Unstable Drainage of Frictional Fluids and Magnetic Control of the Mechanical Behavior of Confined Granular Media

Louison Thorens

NUMÉRO NATIONAL DE THÈSE : 2021LYSEN069

THÈSE DE DOCTORAT DE L'UNIVERSITÉ DE LYON

OPÉRÉE PAR

L'ÉCOLE NORMALE SUPÉRIEURE DE LYON

EN COTUTELLE AVEC

L'UNIVERSITÉ D'OSLO

ÉCOLE DOCTORALE N°52 PHYSIQUE ET ASTROPHYSIQUE DE LYON (PHAST)

DISCIPLINE : PHYSIQUE

SOUTENUE PUBLIQUEMENT LE 17 NOVEMBRE 2021, PAR :

LOUISON THORENS

UNSTABLE DRAINAGE OF FRICTIONAL FLUIDS AND MAGNETIC CONTROL OF THE MECHANICAL BEHAVIOR OF CONFINED GRANULAR MEDIA

DRAINAGE INSTABLE DE FLUIDES FRICTIONNELS ET CONTRÔLE MAGNÉTIQUE DU COMPORTEMENT MÉCANIQUE DE MILIEUX GRANULAIRES CONFINÉS

DEVANT LE JURY COMPOSÉ DE:

ERIC CLÉMENT	PROFESSEUR	ESPCI–PSL–SORBONNE UNIVERSITÉ
AXELLE AMON	MAÎTRE DE CONFÉRENCES	UNIVERSITÉ DE RENNES
PASCALE AUSSILLOUS	PROFESSEURE	AIX-MARSEILLE UNIVERSITÉ
NICOLAS TABERLET	MAÎTRE DE CONFÉRENCES	UNIVERSITÉ LYON 1 - ENS DE LYON
DAG KRISTIAN DYSTHE	PROFESSEUR	UNIVERSITÉ D'OSLO

SOUS LA DIRECTION DE :

STÉPHANE SANTUCCI	CHARGÉ DE RECHERCHE	CNRS - ENS DE LYON	DIRECTEUR
KNUT JORGEN MÅLØY	PROFESSEUR	UNIVERSITÉ D'OSLO	CO-TUTEUR
MICKAËL BOURGOIN	DIRECTEUR DE RECHERCHE	CNRS - ENS DE LYON	CO-ENCADRANT

ABSTRACT

The transport of immersed grains in confined environments is found in many industrial and natural situations with notably the recovery and transport of oil in pipelines, the decontamination of soils, the transport of sediments or the circulation of physiological fluids.
The study of the slow drainage of a model system composed of a mixture of water and glass beads sedimented in a Hele-Shaw cell or a capillary showed the emergence of instabilities, with the formation of labyrinthine patterns and granular plugs.
In this thesis, we have identified the physical parameters and conditions necessary for the triggering of such instabilities, controlled by the meniscus pushing the grains at the liquid/air interface. We have also highlighted a new unstable drainage regime leading to the periodic formation of dunes along the capillary.
As the friction of the grains with the walls of the tube governs the formation of the plugs, we have also studied an original method to control these frictional interactions by using ferromagnetic particles: submitted to a magnetic field, they acquire a magnetic moment, leading to tunable interactions of pairs of magnetic dipoles. Considering all these anisotropic interactions within a confined granular column, we were able to demonstrate the emergence of a radial force along the walls of the silo, whose amplitude and direction is completely determined by the applied magnetic field. This "magnetic Janssen effect" allows to control the apparent mass of the granular column, paving the way towards the design of granular meta-materials whose mechanical (un)blocking properties can be remotely controlled or even programmed.

RÉSUMÉ

Le transport de grains immergés en milieux confinés se retrouve dans de nombreuses situations industrielles et naturelles avec notamment la récupération et le transport de pétrole en oléoducs, la décontamination de sols, le transport de sédiments ou encore la circulation de fluides physiologiques.
L'étude du drainage lent d'un système modèle composé d'un mélange d'eau et billes de verres ayant sédimentées dans une cellule de Hele-Shaw ou un capillaire a démontré l'émergence d'instabilités, avec la formation de motifs labyrinthiques et de bouchons granulaires.
Dans le cadre de cette thèse, nous avons identifié les paramètres physiques et conditions nécessaires au déclenchement de telles instabilités, contrôlées par le charriage des grains par le ménisque à l'interface liquide/air. Nous avons d'autre part mis en évidence un nouveau régime de drainage instable conduisant à la formation périodique de dunes le long du capillaire.
La friction des grains avec les parois du tube gouvernant la formation des bouchons, nous avons également étudié une méthode originale permettant de contrôler ces interactions frictionnelles en utilisant des particules ferromagnétiques : soumises à un champ magnétique, elles acquièrent un moment magnétique, conduisant à des interactions de paires de dipôles magnétiques, ajustables. En considérant l'ensemble de ces interactions anisotropes au sein d'une colonne granulaire confinée, nous avons pu démontrer l'émergence d'une force radiale le long des parois du silo, dont l'amplitude et la direction est complétement déterminée par le champ magnétique appliqué. Cet « effet Janssen magnétique » permet alors de contrôler la masse apparente de la colonne granulaire, ouvrant la voie à la conception de méta-matériaux granulaires dont les propriétés mécaniques de (dé)blocage peuvent être contrôlées à distance, voire programmées.

ACKNOWLEDGMENTS

First of all, I would like to express my deepest gratitude to my main supervisors. Stéphane Santucci, for being present all along these three years and being always supportive, I hope this journey was only a beginning. Knut Jørgen Måløy for trusting me to be part of Porelab, working with you is a real pleasure and I am thankful to have crossed path with you. I would also like to thank my co-supervisors Mickaël Bourgoin, for initiating this project and helping me for several years now, and Eirik G. Flekkøy for the valuable discussions and the clear interest in this project. You are the ones who made my doctoral research possible by giving me the freedom to follow my thoughts and for having unwavering belief in my abilities.
During my PhD I had the feeling of being a part of a wonderful community, and I would like to thank all the amazing colleagues both in Porelab and in Lyon. I would like to give a special thanks to the people who helped me work in the laboratories, and more specifically to Mihailo Jankov. All of you made this journey so enjoyable and full of sweet memories.
Finally, these three years, working in two countries, have not been without hardships; and I would like to express my wholehearted thanks to my family and my long-term friend Yannick Bertrand for their relentless support during the crisis.

CONTENTS

1

CONFINED GRANULAR MEDIA OVERVIEW

Confined granular media in the presence of a liquid and gas phases may present unstable dynamics during the slow drainage of the liquid. These instabilities are the result of frictional interactions with the geometry walls as well as a capillary forces at the liquid/gas interface.
In this chapter we give a review of confined granular media mechanics focused on the interactions at play in these instabilities. First, we recall the dry grains behaviour in a confined geometry. Second, in the perspective of a control of the medium behaviour, we investigate the role of interactions between grains. Finally, the multiphasic response of an immersed granular medium is described when adding liquid and then air to the system.

1.1 MECHANICS OF DRY GRANULAR MEDIA

(a) Coffee grains (b) Gravel (c) Drug pills (d) Saturn

Figure 1.1: Examples of different granular material.

Coffee, gravel, pills or Saturn's rings, presented in figure (1.1), all have in common to be a collection of individual grains and form a part of what is called granular matter. Thanks to their omnipresence in a variety of systems, in both industrial or natural context, granular media have been the subject of a recent upsurge within an active research community [1–3]. In Nature, or more explicitly in geophysics, granular matter can take various forms, from the formation of dunes in deserts, coastal regions where water comes into play or even snow avalanches where phase transitions can occur. Granular matter apprehension is therefore of high importance to prevent accidents or predict the shape of future landscapes. From an industrial point of view, the challenge of granular matter is mainly technological with the improvement of granular processes and technical designs. Indeed, they represent the second most manipulated materials after water [2], and as a striking example, the building industry uses each year around 40 billion of tones of sand and gravel [4]. In spite of granular media variety, their behaviour follow a set of common fundamental laws some of which, of importance for the rest of this study, are introduced and described in this chapter.

(a) Dune (b) Landslide (c) Sandstorm

Figure 1.2: Depending on the system, granular matter can behave as a solid, a liquid or a gas.

Before going any further, we recall that, usually, a distinction is made between grains and colloids for which the thermal agitation plays a major role. A quick energy comparison on a particle of radius a between the gravitational potential energy and the thermal agitation gives a limit of $a \approx 1\,\mu m$ at room temperature:

$$\rho g \frac{4}{3}\pi a^4 = \frac{1}{2}k_B T \rightarrow a = \sqrt[4]{\frac{3k_B T}{8\rho g}} \approx 1\,\mu m\,, \tag{1.1}$$

where $k_B \approx 1 \times 10^{-23}\,J \cdot K^{-1}$ is the Boltzmann constant, $T \approx 300\,K$ is the room temperature, $\rho \approx 2 \times 10^3\,kg \cdot m^{-3}$ the particle density and $g \approx 10\,m \cdot s^{-2}$ the acceleration of gravity. In the rest of this study we will focus on grains of radius far greater than $1\,\mu m$.

Despite their common presence and numerous studies, due to their complexity, the mechanical behaviour of granular systems still remain challenging for engineers and physicists. They are defined by an assembly of particles for which individual mechanical interactions can be described. At the system scale however, the granular assembly represents a colossal amount of particles making a macroscopic description more intricate. For example, a single cup of coffee made in a French press, well studied in [5], ($R = 5\,cm$, $h = 2\,cm$) contains about 10^5 grounded coffee particles of size $500\,\mu m$! Moreover, as figure (1.2) represents, a granular system can behave as a solid, a liquid or a gas depending on the system conditions. A sand pile at rest on a surface will behave as a solid, characterized by an avalanche angle, while the granular assembly of a discharging silo flows as a liquid. At the extreme, grains in suspension in air will behave as a dilute gas, for which sandstorm are a nice illustration. Moreover, several or all these granular phases can coexist inside the same system. Think of an hourglass where the sand is flowing out of a resting pile in the upper chamber. All these considerations are the heart of the granular matter complexity.

Janssen Effect

One of the most renown behaviour of grains certainly is the Janssen effect that we will describe here. Back in 1895, the German engineer H. A. Janssen proposed a description of the stress redistribution inside grain silos. Janssen noticed that the apparent mass at the bottom of a silo does not follow the hy-

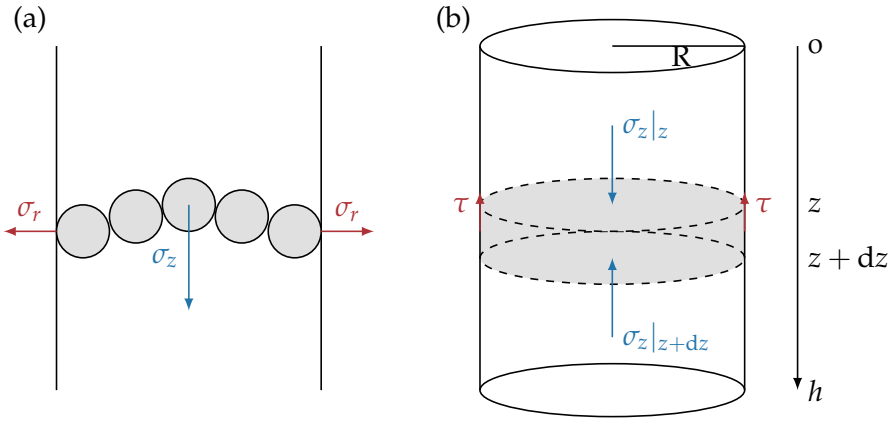

Figure 1.3: (a) Typical arch formation inside a confined granular packing, leading a redistribution of the vertical stress along the radial direction. (b) Force equilibrium on a horizontal slice of a confined granular medium in a silo.

drostatic pressure law of liquids for which the pressure is directly proportional to the height of the column. In fact, a grain silo appears lighter than it really is, suggesting that a part of the grains weight is supported by the walls of the vessel. This model still remains a good description of silos' mechanics and has been used ever since to predict the stress distribution to take into account in their construction.
Janssen's description is based on three hypotheses:

(i) the granular medium and the vertical stress σ_z in the radial direction r are supposed uniform,

(ii) the friction forces between grains and the walls are supposed to be fully mobilized along the vertical direction $\tau = \mu\sigma_r$, where μ is the friction coefficient and σ_r the radial stress acting on the wall,

(iii) the vertical stress redirects partly to the radial direction following a proportional law characterized by the Janssen constant κ, $\sigma_r = \kappa\sigma_z$, as described in figure (1.3.a).

Hypotheses (ii) and (iii) lead to the frictional stress at the tube wall $\tau = \mu\kappa\sigma_z$, while (i) allows us to write the force equilibrium on a packing layer of height dz, shown in figure (1.3.b):

$$\pi R^2 dz\phi\rho g + \pi R^2 \left(\sigma_z|_z - \sigma_z|_{z+dz}\right) - 2\pi R dz\mu\kappa\, \sigma_z|_z = 0\,, \tag{1.2}$$

where the apparent density of the granular medium is $\phi\rho$, with ϕ the packing fraction typically around 0.6 for random close packing, and ρ the material density of the grains, typically around $\rho \approx 2 \times 10^3\,\mathrm{kg}\cdot\mathrm{m}^{-3}$ for sand. Dividing this equation by the infinitesimal height dz leads to the differential equation:

$$\frac{d\sigma_z}{dz} = -\frac{2\kappa\mu}{R}\sigma_z + \phi\rho g\,, \tag{1.3}$$

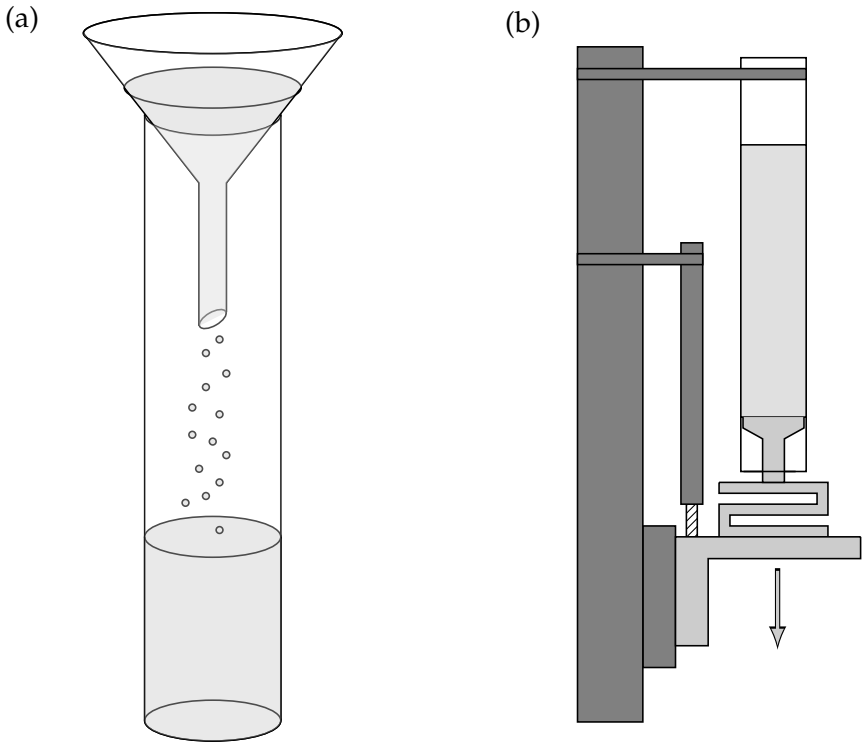

Figure 1.4: Janssen effect experimental apparatus. (a) Typical filling protocol where the beads are poured inside a tube via a funnel. (b) Experimental set-up inspired by [6] where the light grey area is free to move downward at a constant velocity.

with a straight-forward solution:

$$\sigma_z(z) = \phi\rho g\lambda\left(1 - \mathrm{e}^{-\frac{h}{\lambda}}\right) \quad , \quad \lambda = \frac{R}{2\kappa\mu} \, , \tag{1.4}$$

where we defined the screening height λ depending on the tube radius R, the Janssen constant κ usually ranging from 0 to 1 and depending on the grain properties, and the friction coefficient μ between the grains and the silo wall. The pressure at the bottom of the tube is usually expressed as the apparent mass of the granular column $m = \sigma(h)\pi R^2/g$:

$$\boxed{m = m_\infty\left(1 - \mathrm{e}^{-\frac{m_0}{m_\infty}}\right) \quad , \quad m_\infty = \frac{\pi R^3\phi\rho}{2\kappa\mu} \, .} \tag{1.5}$$

This exponential saturation law means that for a packing mass greater than a few critical mass m_∞ (or a packing height greater than a few characteristic length λ), the apparent mass at the bottom of the silo is constant and equals the critical mass. In other terms, the upper part of the packing is screened by the first layers of grains and the apparent mass for high enough silos does not depend on the packing height. Typically, the characteristic length is about the tube diameter $\lambda \approx 2R$.

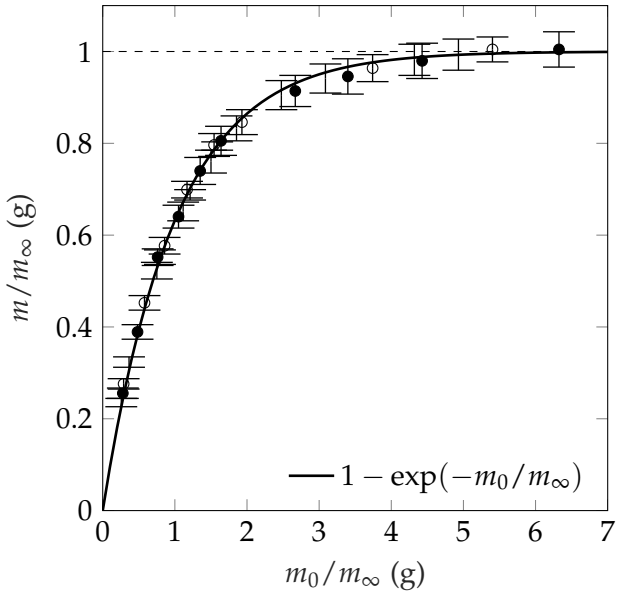

Figure 1.5: Typical Janssen effect measurement, data from [7]. The apparent mass of a granular column is measured for different packing parameters and normalized by the critical mass m_∞.

Experimentally, the Janssen effect is characterized by the measurement of the apparent mass of grains poured inside a tube via a funnel as shown in figure (1.4.a) . As shown in figure (1.4.b), the granular packing is resting on a piston, slightly smaller than the tube to ensure no contact with the walls, in order to measure directly the apparent mass of the packing using a force gauge. Though seemingly simple, the Janssen system presents some experimental difficulties. Indeed, when dealing with granular matter, one shall remember that the friction forces are usually undetermined since the Coulomb criterion gives an inequality between the normal and the resulting tangential friction force [8]:

$$f_t \leq \mu f_n, \tag{1.6}$$

where f_t and f_n are respectively the tangential and normal forces. The friction forces are usually in an undetermined state. The force network is undetermined and imposed by the preparation of the granular packing. However, the Janssen hypothesis (ii) requires that the friction forces at the wall are fully mobilized in the vertical direction. In [6], L. Vanel and E. Clément proposed to reach this condition by moving downward the lower part of the mass measurement set-up, represented by the light grey area in figure (1.4.b). Figure (1.5) shows the apparent mass measurement for different packing mass m_0 following this experimental protocol. The experimental results are in very good accordance with the Janssen prediction. Even though the Janssen description considers the medium as continuous, it still remains nowadays a good prediction of the force redistribution inside a confined granular packing.
Nevertheless, since 1895, some refinements to the Janssen model have been brought to attention, one can think of the OSL (oriented stress linearity) model taking into account the grain-scale forces [9, 10]. Moreover, some limitations

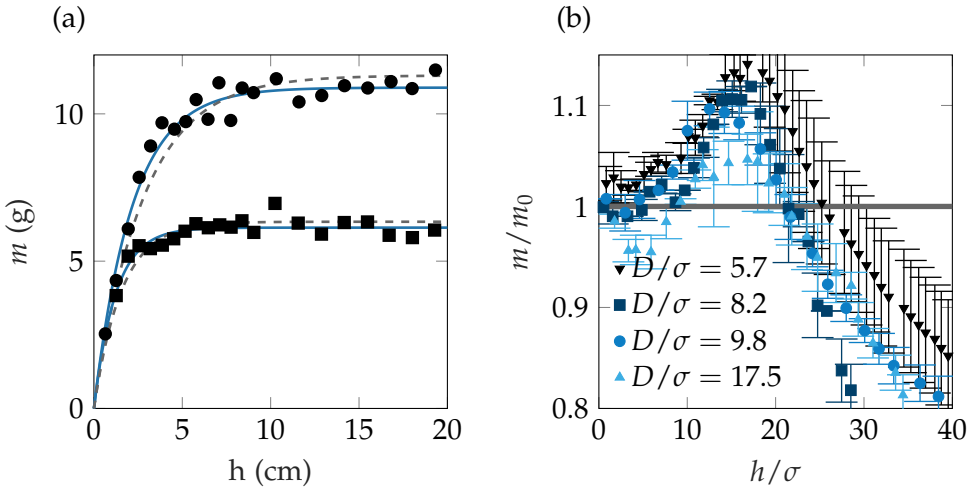

Figure 1.6: Janssen effect in a narrow tube. (a) Data from [11]. Two apparent mass measurements for a tube diameter of about 5 bead radii, the apparent mass follows a two-parameters saturation law. The dashed line corresponds to the classical Janssen prediction while the blue line corresponds to the modified prediction. (b) Data from [12]. Apparent mass rescaled by the true mass of grains for different narrow tube of diameter D, with a bead diameter σ. One can notice that the apparent mass can be greater than the actual mass of the packing.

to the Janssen model can be found for narrow granular column [11] where the Janssen effect does not follow a one-parameter (m_∞) exponential saturation but depends on two parameters, $m = m_\infty(1 - \exp(-m/\tilde{m}))$, where $\tilde{m}$ is a screening mass. A typical example of this result is displayed in figure (1.6.a), and can be understood as the formation of cell arrangement inside the packing. Confined grains in a narrow tube can also display striking phenomena as presented by [12] and shown in figure (1.6.b). In this case, the frustration of mechanical stress at the grain level and the violation of Janssen hypothesis (iii) leads to the apparition of additional compressive force resulting in a packing apparent mass greater than the actual mass of the grains, $m/m_0 > 1$, called "reverse Janssen effect". On top of the intrinsic parameters of the system (geometry, density, etc.), the Janssen effect depends strongly on the preparation of the granular packing as described in [13].

To complete the description of confined granular media mechanics, we present in the following sections some striking dynamics properties.

Discharge of a granular silo

We have described so far the static regime of grains silos. We propose here to describe their dynamic discharge. An emptying silo is similar to an hourglass. The most striking fact about them is that the output flow rate of beads does not depend on the height of grains stored in the upper chamber. This surprising behaviour is the reason why hourglass are filled with sand instead of water, the passed time is proportional to the amount of sand that flowed through the orifice. The origin of this independence over the height is still uncertain. For

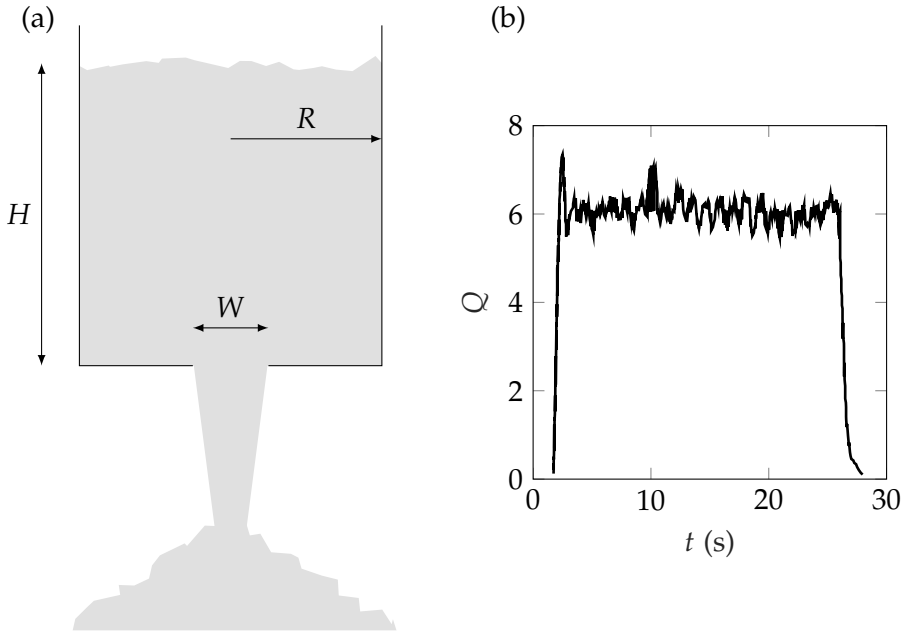

Figure 1.7: Discharge of a silo. (a) Schematic view of discharging silo characterized by its radius R and opening width W. (b) Data from [14]. Flow rate of a discharging silo, constant over time.

long time, the Janssen effect was proposed to be at the origin of the constant flow rate of the grains escaping the hourglass. Nevertheless, recent work from [15, 16] showed that the flow rate does not depend on the local pressure around the outlet, thus refuting the Janssen hypothesis.

Despite a clear understanding of the origin of such behaviour, one can still predict the flow rate at the output of a silo, shown in figure (1.7). If we suppose that the flow rate is constant and does not depend on the silo radius R, a relevant spatial scale of the problem is the outlet diameter W. The grain velocity at the outlet is then approximated by $v \sim \sqrt{gW}$. Moreover, the area of the outlet, in three dimensions, is proportional to W^2. A mass conservation law leads to the granular flow rate:

$$Q \sim \rho \sqrt{g} W^{5/2} \tag{1.7}$$

In practice, due to the finite size of the grains, the outlet width W is effectively reduced by a width W_m of about a few grain diameters. This prediction of the flow rate at a silo output is known as the Beverloo equation [18]:

$$\boxed{Q = C\rho\sqrt{g}\,(W - W_{\mathrm{m}})^{5/2},} \tag{1.8}$$

where C is a constant around 0.5, and the power $5/2$ becomes $3/2$ in the case of a two-dimensional silo. Two sets of experimental results for two different geometries are shown in figure (1.8). The Beverloo prediction is in really good agreement with the flow rate measurements.

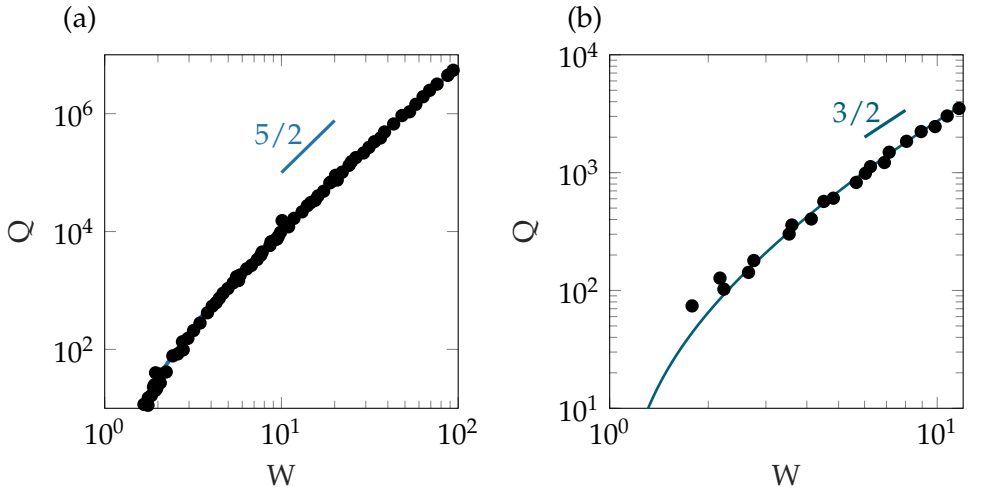

Figure 1.8: Flow rate of a discharging silo. Data from [17]. (a) (resp. (b)) Flow rate at the output of a 3D (resp 2D) silo. The experiments are following nicely the power law prediction in 5/2 (resp. 3/2).

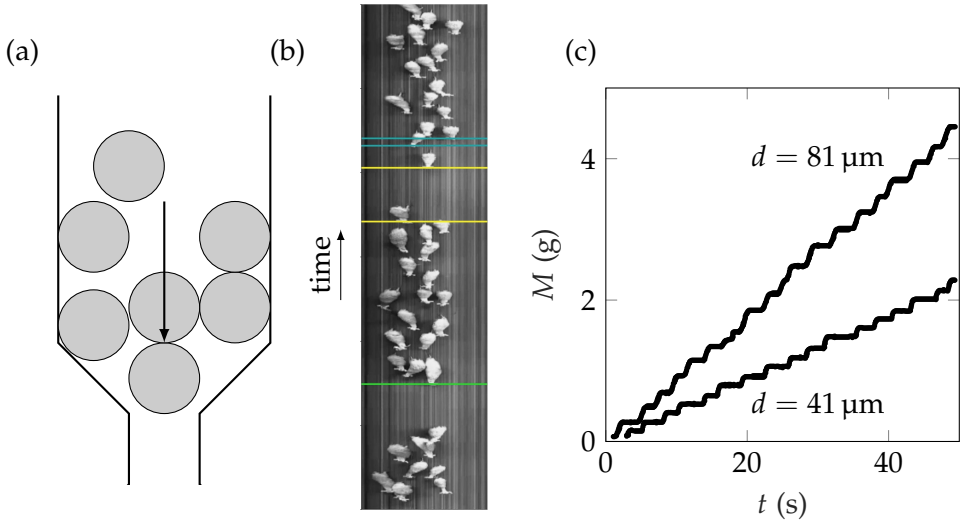

Figure 1.9: Clogging situation. (a) Inspired by [19]. Particles flowing through a too small opening will clog. (b) Image from [20]. Spatio-temporal diagram of sheep passing through a gate with a ticking behaviour. (c) Data from [21]. Ticking hourglass where the flow rate follows a stick-slip behaviour, represented as the mass in the lower chamber of the hourglass for two different glass beads diameter d.

Nevertheless, for small openings $W < 10a$, the grains will have a tendency to form arch ahead of the neck and the system will clog, as shown by [19] and figure (1.9.a). The clogging situation is also of great interest for crowd behaviour research, where individual person can be considered similar to grains. This model allows to find the best geometry in order to maximize the flow of people through a constrained opening [22]. Similar experiments have also been conducted with sheep [20] as shown in figure (1.9.b). Depending on the system conditions, the geometry can unclog spontaneously after a moment, resulting in a periodic flow similar to a stick-slip mechanical behaviour. This is very similar to the flow of cars during rush hour, the cars will form traffic jam which are constantly being formed and unformed in an accordion way.
Similar behaviour can be obtained in a so-called "ticking hourglass" where the lower chamber of an hourglass is closed. The pressure increases as the number of particles there increases. At some point the pressure in the lower chamber will overcome the pressure needed to stabilize the flow rate at the opening. Then, air percolates through the medium and the flow of grains can start again [21]. Results from two experiments are shown in figure (1.9.c).

Compaction of a granular medium

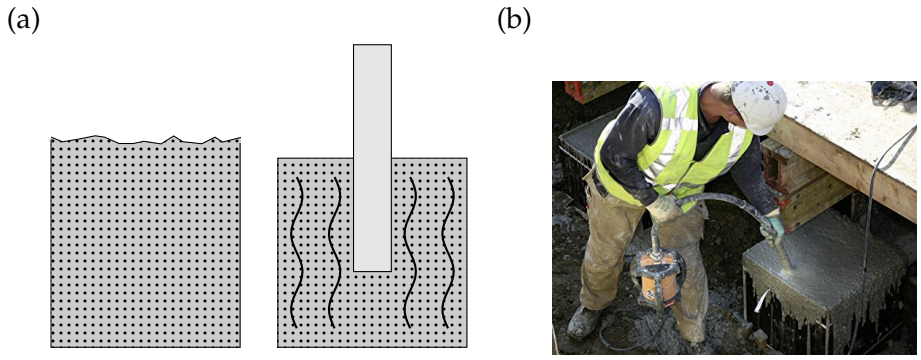

Figure 1.10: Compaction of concrete. (a) Schematic view of a concrete vibrator where the granular medium is vibrated to remove trapped air clusters. (b) Building worker using a concrete vibrator.

Concrete certainly is one of the most common granular material. Made of sand and gravel, concrete is largely used in the building industry, and its strength is of primary importance. Due to its granular nature, concrete does not fill completely the allowed space, leaving space to air, characterized by the packing fraction ϕ. Previous studies showed that the strength of concrete is directly linked to the amount of air trapped inside the packing [23, 24]. It is therefore essential to make concrete as compact as possible to prevent any future failure. To do so, building workers use a "concrete vibrator" as shown in figure (1.10), which vibrates the granular medium for a few seconds to liquefy it and remove trapped air clusters. At smaller scale, compaction of granular media is of great interest for the conception of fuse [25].

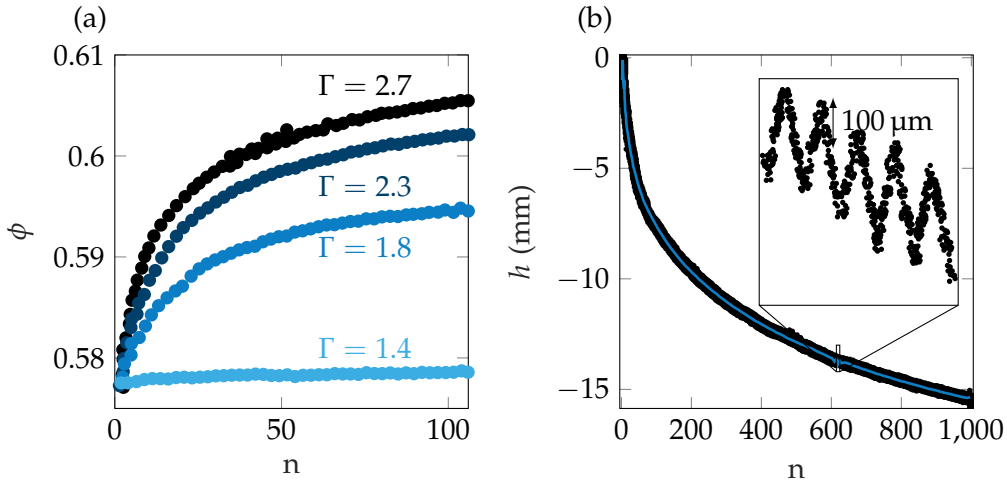

Figure 1.11: Compaction of granular material. (a) Data from [26] Mechanical compaction for different vibration intensity $\Gamma = a/g$ where a is the tap acceleration. (b) Data from [27]. Compaction using temperature cycles of a 140 cm tall column with a temperature oscillation of $\Delta T = 10.8$ °C of periodicity $2\pi/\omega = 600$ s.

In the lab, the compaction of granular media can be achieved by various means. The commonly used system is a tube undergoing periodic mechanical shakes [26, 28, 29], as used in concrete vibration. Figure (1.11.a) shows the typical compaction curve with mechanical taps of different acceleration. The compaction is characterized by an exponential law which characteristic time (in number of taps n), depends on the strength of the tap. Nevertheless, mechanical perturbation of the granular system is not the only way of getting compaction. In [27], Divoux et al. described the compaction of glass beads by applying temperature cycles to the tube. Starting from a loose packing of beads, the granular column height undergoes the same kind of exponential relaxation, as shown in figure (1.11.b), with a series of granular collapses at each temperature oscillation.

1.2 GRAINS INTERACTIONS

So far, we described the global behaviour of a dry granular medium. In this section we investigate several interactions between grains leading to new granular medium responses.

Model of granular interaction

Before going any further, we want to briefly remind the classical mechanic interactions at the grain scale. We differentiate three actions shown in figure (1.12):

(a) tangential friction, given by the Coulomb criterion (1.6), and strongly history dependent,

(b) rolling friction, where the resistance of rolling movement given by a reaction torque $\mathcal{M}^r = \mu^r f_n a$, where μ^r is the rolling friction coefficient [30],

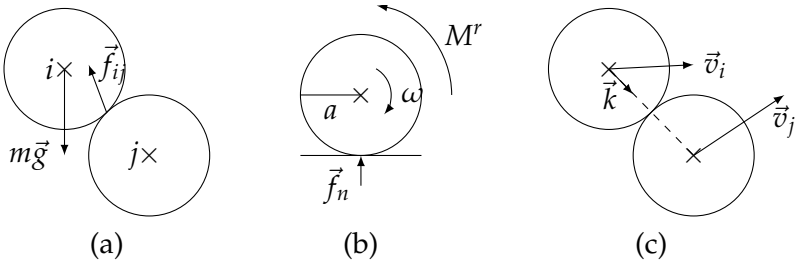

Figure 1.12: Mechanical interactions at the grain scale. (a) Friction. (b) Rolling friction. (c) Inelastic collision.

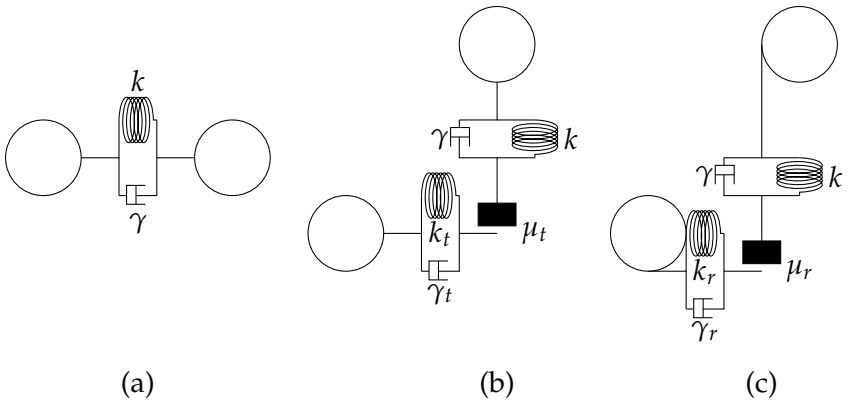

Figure 1.13: Simulation modelling of grains interactions. (a) Normal characterized by the stiffness k and dissipation γ. (b) Tangent characterized by the stiffness k_t, γ_t and friction μ_t. (c) Rolling characterized by the stiffness k_r, γ_r and friction μ_r.

(c) inelastic collision, characterized by a restitution coefficient e linking the velocities of both particles before $\vec{v}_{ij}$ and after the shock $\vec{v'}_{ij}$: $(\vec{v'}_j - \vec{v'}_i) \cdot \vec{k} = -e(\vec{v}_j - \vec{v}_i) \cdot \vec{k}$.

In simulation however, the most common way to model grains proposed by [31] is to represent them by hard spheres but able to interpenetrate each other. At each time step, and for each collision between two particles i and j, the overlap δ_{ij} between the two spheres is stored and used to compute the new positions, velocities and rotation of the spheres modelled by a set of springs. Each of the interactions are characterized by viscous dissipations and friction coefficients as shown in figure (1.13), used in several common Discrete Element Method codes such as [32].

Some usual added interactions

In real life, mechanical interactions at the grain level are usually not the only ones at play. We present here common interactions that can be introduced at the grain level, having an impact on the global behaviour of the granular system. For those who went to the beach and built a sand castle, you certainly already know that adding a small amount of water to the sand is making it more cohesive and therefore suitable for building structures [33, 34]. The key element

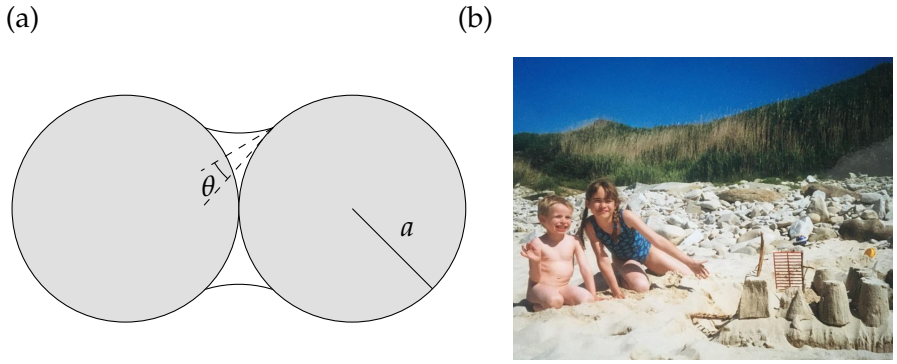

Figure 1.14: Physics of a sandcastle. (a) A small amount of water inside the granular packing results in the formation of capillary bridges between the grains. (b) Two young siblings (my sister and I), building a sandcastle (Île-Grande 1999).

here is the formation of capillary bridges between the grains, as shown in figure (1.14), leading to a capillary force acting between the two spheres [35]:

$$F_{\text{cap}} \sim 2\pi\gamma_{\text{la}} a \cos\theta \,, \tag{1.9}$$

where γ_{la} is the liquid/air surface tension. The maximum strength is achieved for really low volume fraction of about 1-3% [36]. For higher volume fraction of water inside the granular material the structure will collapse and the medium behaves as a liquid, as seen during landslides.
Cohesion of a granular medium can also be achieved by applying an electric field to the system [37]. In this case, a strong high-voltage difference is applied to the front and back plates of a rectangular silo filled with non-conductive glass beads, and various cohesive regime are reached. Without any electric field, figure (1.15.a), the classical Beverloo law is retrieved. For medium applied electric gradient, figure (1.15.b), a stabilization of the grains at the border of the cell is observed and the flow regime is restricted to the centre of the medium while the borders flow by successive avalanches. Finally, for high electric field, figure (1.15.c), a "rathole" regime is achieved where the flow of grains is restricted to the centre of the cell while the borders of the granular medium do not move and are stabilized by cohesion of the medium.

Magnetic granular media

In our work, we investigate tunable magnetic interactions inside a granular medium. Here, we recall the magnetic interactions between two uniformly charged ferromagnetic spheres as well as previous studies of such media.
Let us consider two grains i and j made out of ferromagnetic material, typically steel, who will acquire magnetic moment $\vec{d}_i$, $\vec{d}_j$ when submitted to a magnetic

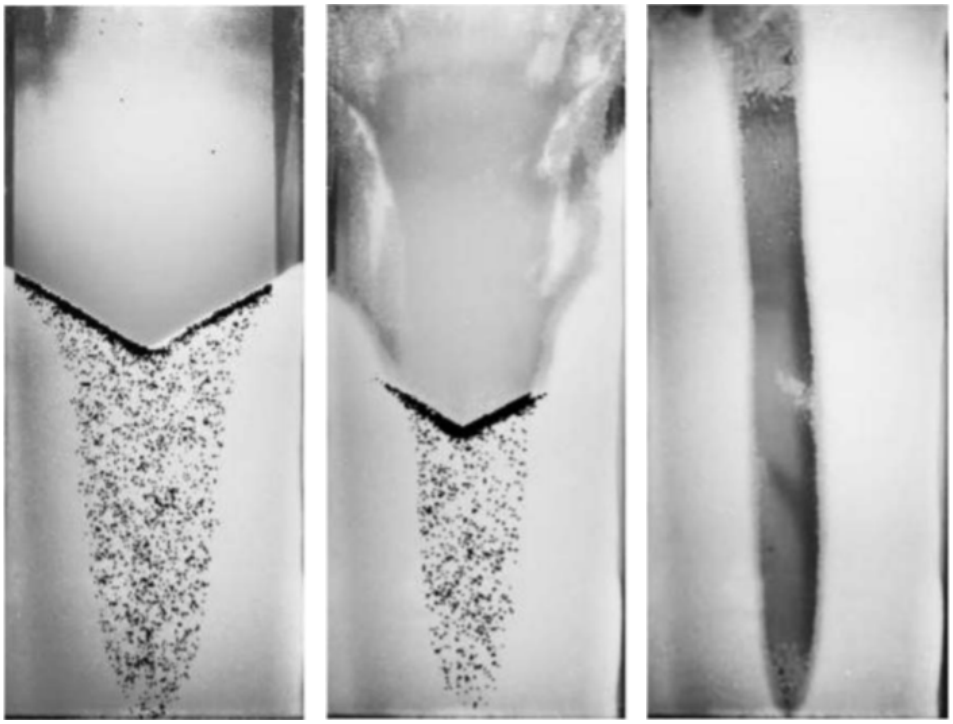

(a) (b) (c)

Figure 1.15: Discharge of an electrically cohesive silo, from [37]. (a) Flow without electric field (0 V). (b) Avalanche regime (500 V). (c) Rathole regime (1500 V).

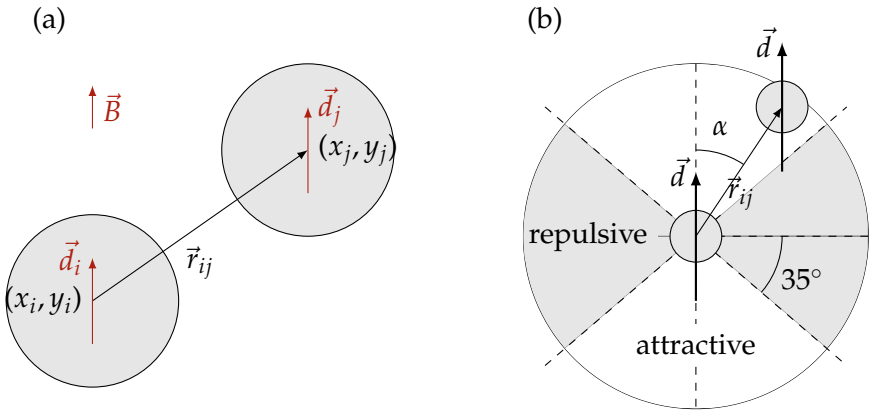

Figure 1.16: Magnetic interaction between two ferromagnetic grains. (a) When submitted to a vertical magnetic field $\vec{B}$, both grains acquire a magnetic moment $\vec{d}_i$, $\vec{d}_j$. (b) In the case of a uniform magnetic field, the magnetic interaction between the two beads can be either attractive or repulsive.

field $\vec{B}$, as shown in figure (1.16.a). The magnetic interaction between the two spheres is given in the general case by [38]:

$$\vec{f}_{ij} = \frac{3\mu_0}{4\pi r_{ij}^5}\left[\left(\vec{m}_i \cdot \vec{r}_{ij}\right)\vec{m}_j + \left(\vec{m}_j \cdot \vec{r}_{ij}\right)\vec{m}_i + \left(\vec{m}_i \cdot \vec{m}_j\right)\vec{r}_{ij} - 5\frac{\left(\vec{m}_i \cdot \vec{r}_{ij}\right)\left(\vec{m}_j \cdot \vec{r}_{ij}\right)}{r_{ij}^2}\vec{r}_{ij}\right].$$

In the case where the magnetic field is uniform in the medium, both magnetic moments will be equal, $\vec{d}_i = \vec{d}_j = \vec{d} = V\chi B/\mu_0$, with V the bead volume, χ the magnetic susceptibility, μ_0 vacuum permeability. In this case, the magnetic interactions between the two spheres can be simplified to:

$$\vec{f}_{\mathrm{ij}} = \frac{3\mu_0}{4\pi r_{ij}^5}\left(d^2\left(1 - 5\cos^2\alpha\right)\vec{r}_{\mathrm{ij}} + 2dr_{ij}\vec{d}\cos\alpha\right), \tag{1.10}$$

where r_{ij} is the separation vector between the two grains and α the angle between this vector and the applied magnetic field direction. In this case, it is easy to notice that the interaction can be either repulsive or attractive depending on the position of both particles, as summarized in figure (1.16.b), with a transition for $\alpha = 55°$.

The magnetic interaction is directly proportional to the square of the magnetic field amplitude and depends on its direction, making magnetic interactions easily tunable compared to the relative humidity of the system for example. To quantify the magnetic pair interactions, we introduce, as proposed by [39, 40], the magnetic Bond number comparing magnetic pair interactions to a bead weight:

$$\Psi = \frac{\chi_m^2 B^2}{\mu_0 a \rho g}, \tag{1.11}$$

where χ_m is the magnetic susceptibility ceiling at 3 for a particle packing [41].

Previous studies [40, 42–46] have already suggested that the use of magnetic interactions in a granular medium can lead to surprising behaviour at the system scale. For example, [42] studied the stability angle of a magnetic grains assembly inside a rotating drum. Figure (1.17.a) shows their experimental results. When increasing the magnetic field intensity, the medium becomes more stable and cohesive, resulting in a higher stability angle. It is also noticeable that the stability is higher for a horizontal magnetic field (perpendicular to gravity) than for a vertical one. In [40], the flow of magnetic particles through a funnel was investigated, again by varying the direction and amplitude of the external magnetic field. The discharge dynamics is not continuous but the grains are escaping the funnel in a series of periodic cohesive clusters. Nevertheless it is possible to define an average flow rate as the ratio between T_0 and T, respectively the emptying time without and with a magnetic field. Figure (1.17.b) shows the experimental results for a vertical and horizontal magnetic field. As a result of the magnetically induced cohesion, the flow rate decreases when increasing the magnetic field amplitude, with a stronger effect for a vertical magnetic field, even up to a clogging situation for a critical

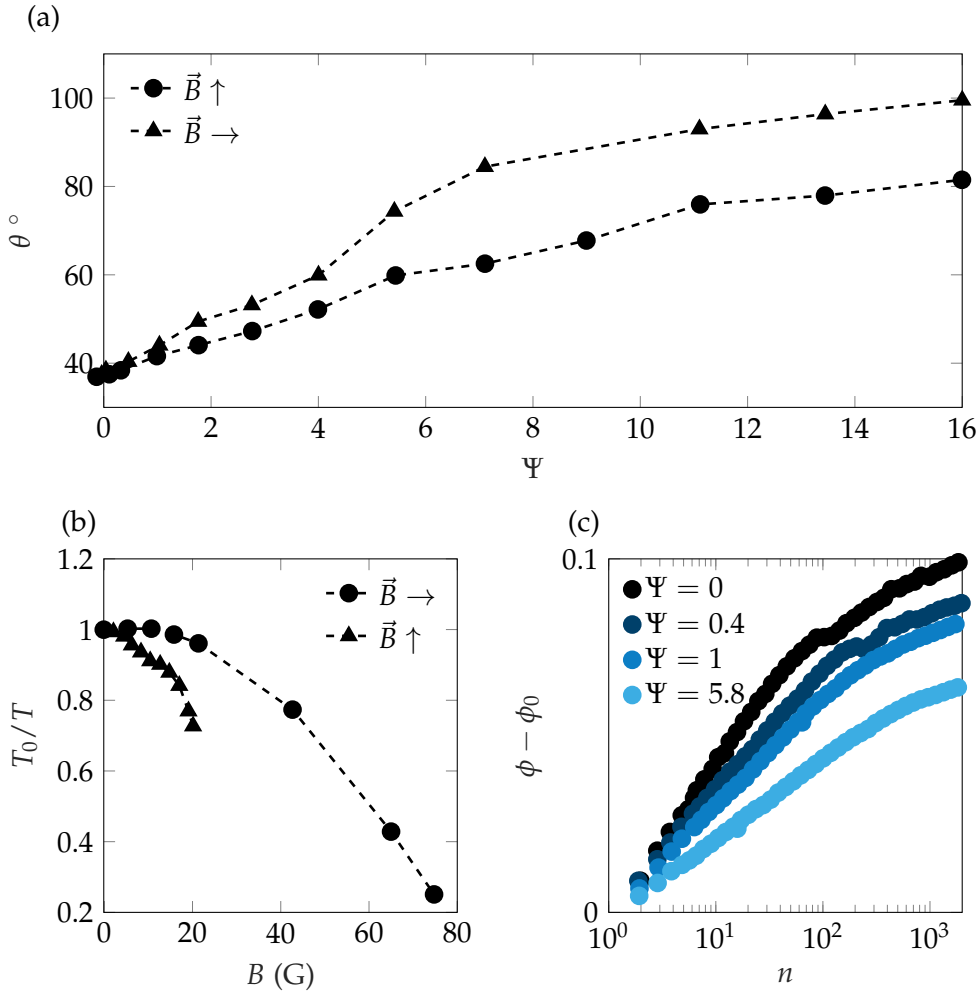

Figure 1.17: Magnetic field interactions impact on a granular medium. (a) Stability angle of grains inside a rotating drum for different magnetic field amplitude and direction, data from [42]. (b) Flow rate of magnetic grains escaping a funnel for different magnetic field amplitude and direction, data from [40]. (c) Compaction curves of a granular column for different magnetic field amplitude, data from [43].

magnetic field $B_c \approx 20\ G$. Finally, the compaction of a granular column is also impacted by the introduction of magnetic interactions, as suggested by [43]. In this study, a granular column was compacted using a series of mechanical taps while a vertical magnetic field was applied to it. By a series of successive tap, the medium is compacted, characterized by an increase of the packing fraction ϕ compared to the initial packing fraction ϕ_0. Figure (1.17.c) gives a series of compaction curves for different magnetic field intensities Ψ, where one can notice that the higher the magnetic field amplitude, the lower the compaction, resulting from the packing cohesion. Similar results were obtained by using a mixture of ferromagnetic and non-ferromagnetic (glass) grains, with an effect noticeable only for high metallic fraction ϕ_m.

1.3 MULTIPHASIC GRANULAR DYNAMICS

The case of dry granular material, a system only composed of solid grains, is already the theater of interesting phenomena as discussed so far. Interactions at the grain scale can modify the global response of the medium. In this section we introduce several phases to the granular system and describe the impact of the novel resulting interactions.

Two-phase sediment transport

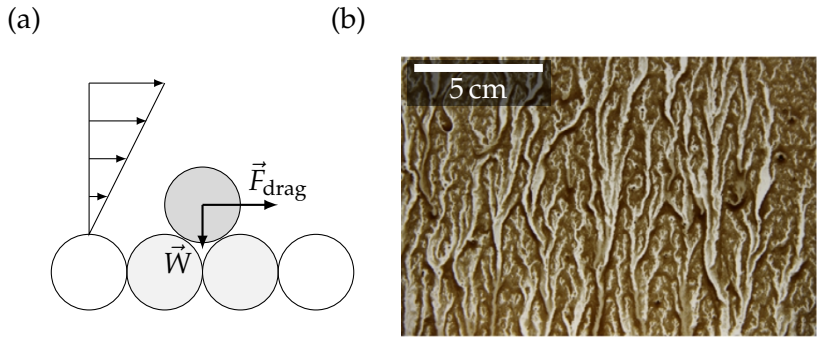

Figure 1.18: (a) Transport threshold of a grain by flowing liquid. (b) Picture from [47]. Fractal erosion pattern of a grain/liquid mixture.

When thinking about rivers, oceans, etc. the liquid and grains scheme is pretty common in Nature. Wind as well can be the driving force behind beautiful pattern formations of dunes, riddles or barchans. The key mechanism between these two-phase systems is the transport of sediments by viscous effects.
Erosion, for example, takes place when a liquid is transporting grains over a large scale and deposit them further away. The time scales in Nature are usually about several million of years and the erosion process is able to transform landscapes. In the lab, toy models of rivers can be used to study the transport of sediments and the formation of dunes at the top of the sedimented layer [48]. The transport of grains by a moving fluid occurs when the fluid flow is strong enough, and more specifically when the stress imposed by the fluid on one grain overcomes the frictional stress induced by other grains, as shown in

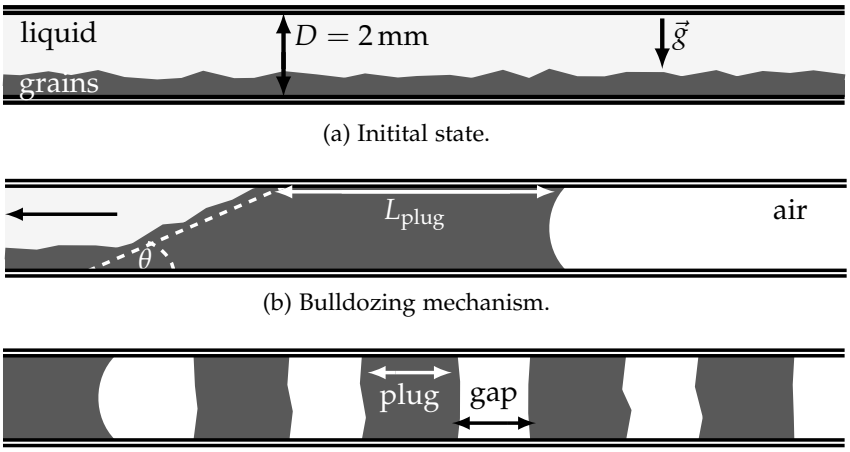

(a) Initital state.

(b) Bulldozing mechanism.

(c) Plugs formation.

Figure 1.19: Frictional fluids in a confined geometry. (a) Initially a layer of beads is resting at the bottom and the liquid is slowly drained out of the system from one side with the other side open to air. (b) The meniscus at the liquid/air border bulldozes particles on its way. (c) After some time, the bulldozing front separates in a series of plugs along the confined geometry.

figure (1.18.a). This criterion is defined as the Shields number, comparing the viscous shear stress τ_f between fluid and grains and the apparent weight of one grain:

$$\Theta = \frac{\tau^f}{\left(\rho_g - \rho_f\right) g d}\,, \tag{1.12}$$

where ρ_g and ρ_f are respectively the grains and fluid densities, d is the grain diameter. The prediction of the transport threshold gives $\Theta \approx 2\mu/9$, with μ the friction coefficient, in good accordance with experiments [49]. From erosion phenomenon, beautiful fractal patterns can emerge as presented in [47, 50] and shown in figure (1.18.b). A mixture of grains and liquid is poured on a vertical wall and let to flow by gravity. The liquid will always find its way and flows along the easiest path eroding particles on its way.

Three phase frictional fluids in confined geometry

Settling granular mixtures with inter-particle friction are known as frictional fluids. By introducing air to the system, a meniscus at the liquid/air boundary appears. The introduction of capillary interactions in the system leads to various dynamic evolution. A good overview of the dynamics in such systems is given in [53], ranging from viscous fingering to frictional fingering depending on the flowing properties and the amount of particles inside the system. In this study we will only consider the frictional case when viscous forces can be neglected. The typical system we consider is a frictional fluid trapped inside a confined geometry either in a Hele-Shaw cell or a capillary tube as shown in figure (1.19.a). The liquid is slowly withdrawn from the system at a really low flow rate from one side, letting the other side opened to the atmosphere, as shown in figure (1.19.b). Using both Darcy's law, describing the flow through a porous

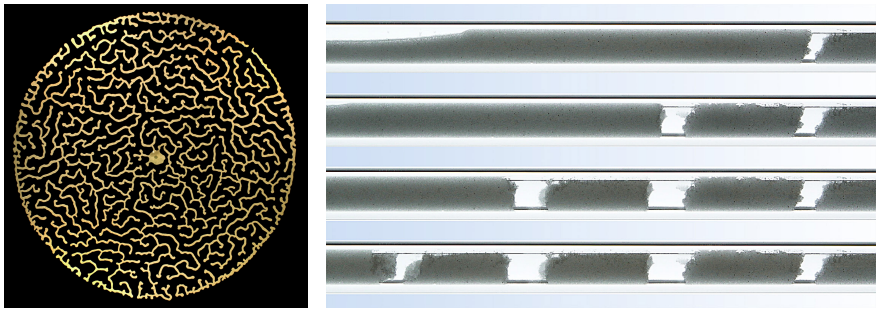

(a) (b)

Figure 1.20: Confined frictional fluids experiments. (a) Drainage inside a Hele-Shaw cell resulting in a labyrinthine pattern [51]. (b) Drainage inside a capillary tube resulting in a series of plugs along it [52].

medium, and Kozeny-Carman equation, modelling the pressure drop of a fluid passing through a porous medium, the following criterion [53] on the flow rate q_c below which one can neglect viscous effect can be determined:

$$q_c = \pi D \Delta z \frac{\mu \rho g k(\xi)}{\xi \eta} \,, \tag{1.13}$$

where $k(\xi)$ is the permeability of the medium as function of its porosity ξ, and η is the viscosity of the fluid. For typical values of these parameters ($xi = 0.5$, $eta = 0.1$ cP), the flow rate threshold occurs at $q_c \approx 0.5\,\mathrm{ml} \cdot \mathrm{min}^{-1}$.
Characteristic experimental results for these systems in the Hele-Shaw cell [51, 54, 55] consist in beautiful labyrinthine patterns, shown in figure (1.20.a), which are still under consideration for their interesting diffusion mechanism [56]. The capillary experiment results in the formation of plug and gap patterns [52, 57, 58], shown in figure (1.20.b), which will be the interest of this study, and for which a schematic view is given in figure (1.19.c).

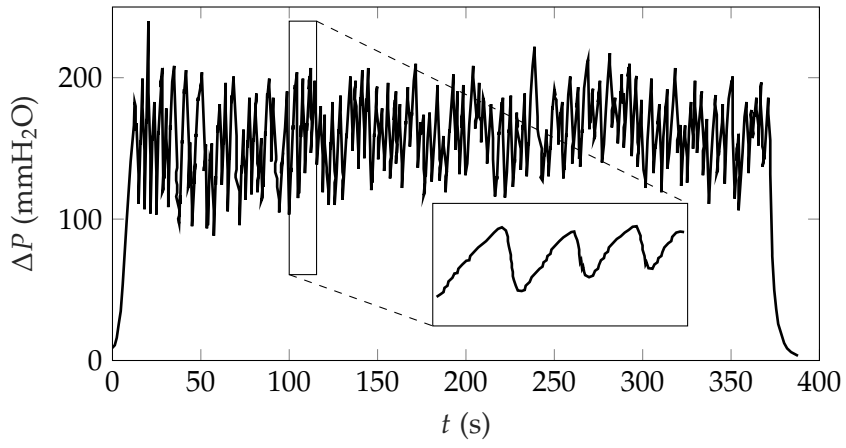

Figure 1.21: Pressure variation during a bulldozing experiment. The pressure is following a stick-slip behaviour, increasing with the plug length and decreasing rapidly when it reaches the minimum pore pressure P^*_{pore}.

In this system, two main ingredients are at play:

- the meniscus, bulldozing the particles front and giving a minimum capillary pressure threshold for air to penetrate a pore of the granular medium p_c,
- the friction forces exerted by the particles and undergoing a Janssen effect, meaning that the longer the plug length L_{plug}, the harder it gets to push the particles.

The whole system is therefore driven by a competition between the pressure needed to push the grain plug forward and p_c. When the latter is lower than the first, air percolates through the system, leaving behind a plug made of grain and trapped liquid. This competition results in a periodic stick-slip behaviour, as shown by the typical pressure evolution in figure (1.21).

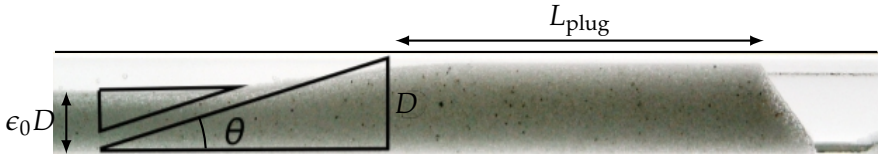

Figure 1.22: Schematic of the plug during the bulldozing experiment.

To describe into details the plug pattern formation, [57] gave a prediction for the plug length depending on the system parameters. As shown in figure (1.22), we note ϵ_0 the initial filling fraction of particles and θ the grain avalanche angle. A calculus given in appendix A leads to the following pressure needed to push the plug ahead:

$$P\left(L_{\text{plug}}\right) \approx \sigma_0(\phi, \mu, \kappa) \exp\left(4\mu\kappa L_{\text{plug}}/D\right), \tag{1.14}$$

with a typical stress σ_0 depending on the system parameters. This pressure grows exponentially with the plug length due to the Janssen effect occurring inside the granular medium, in good accordance with experimental results [57].

STRUCTURE OF THE THESIS

Among the vast panel of granular media phenomena, we described in the first chapter a selective review of granular matter physics in confined geometries relevant for our work.

The slow drainage of immersed grains in confined geometries leads to instabilities that have been well described for model systems in the previous years. Nevertheless, a few questions remain to be addressed. For instance, the displacement of grains by a water/air meniscus in a horizontal capillary tube results in the formation of plugs along the confining geometry. Nevertheless, so far, the triggering of such instability has never been explored. This will the subject of the work presented in this thesis. Indeed, we will show how (by systematically changing the surface tension and the wettability of the liquid drained out of a capillary tube) we could identify the relevant physical parameters and conditions for the emergence of the bulldozing instability. Furthermore, we could also reveal the existence of a new unstable regime of the drainage, leading to the periodic formation of dunes, analogous to the road washboarding instability.

Once the emergence of the bulldozing instability understood, we planned to control its dynamics. Several studies, mentioned in our review, highlighted that the introduction of ferromagnetic pair interactions between grains can lead to a tuned response of the granular system. Therefore, we have also investigated the possibility to tame the bulldozing instability by introducing these magnetic interactions.

The bulldozing instability is governed by the friction between the grains and the system walls, described by the Janssen effect. Thus, we have studied the effect of ferromagnetic pair interactions between grains on the Janssen effect. We could demonstrate that the interactions between magnetized grains result in a radial force along the walls, of amplitude and direction determined by the applied magnetic field. This new "magnetic Janssen effect" allows for the control of the packing apparent mass.

Those results concerning the mechanical behaviour of a static granular assembly confined in a silo led us to investigate some of their dynamical properties. Thus, we started to develop two different experimental studies, with the discharge of a magnetic silo, and the magnetic fatigue of a granular column by applying periodic charging cycles.

2

MAGNETIC JANSSEN EFFECT

In this chapter, we are studying the impact of a magnetic field on the apparent mass of a granular column and characterize the Janssen effect describing its evolution.

2.1 EXPERIMENTAL SET-UP

Our experimental apparatus consists of industrial spherical steel beads of 1.50 mm diameter filling a copper tube of 19.6 mm diameter and laying on a 19.0 mm diameter piston. The piston is slightly smaller than the tube to measure only the mass of the grains. The apparent mass of the column is measured by a force sensor (Testwell KD40S-100N). As proposed by [6], we are mobilizing the friction forces at the wall in the vertical direction to satisfy the Janssen hypothesis (i). The experimental protocol is as follows, and an apparent mass measurement example is given in figure (2.1.a):

1. the grains are poured inside the tube using a funnel,
2. the desired packing mass m_0 is reached, the friction forces at the wall are in an undetermined state,
3. the piston starts to move downward at a constant velocity v, the friction forces at the wall are mobilized along the vertical direction and the apparent mass decreases drastically. The apparent mass is taken as the average along the plateau and the measurement error as the standard deviation,
4. the downward movement stops, due to inertia the grains are pushing down on the piston resulting in a slight increase of the apparent mass [6].

Figure (2.1.b) gives the apparent mass of the granular column for different packing mass m_0 measured using our apparatus. The data points are in excellent agreement with the Janssen prediction m_J with a critical mass $m_\infty = 48\,\mathrm{g}$. The mass measurement during the plateau is not sensitive to the piston velocity v, as suggested by [59], while the apparent mass in region (4) when the piston stops, increases significantly when increasing the velocity.

The external magnetic field was generated using a set of two 10 cm radius coils in an Helmholtz configuration, presented in figure (2.2.a). In such configuration, the magnetic field generated by the two coils, the sum of both individual coils magnetic fields, is roughly constant along the revolution axis as shown in figure (2.2.b). The maximum magnetic field reachable by our apparatus is $B_{\max} \approx 150\ G$. To ensure no magnetic history (remanence) of the grains between two experiments, we followed a demagnetization protocol [60] consisting in applying a 100% amplitude-modulated 20 Hz sinusoidal signal.

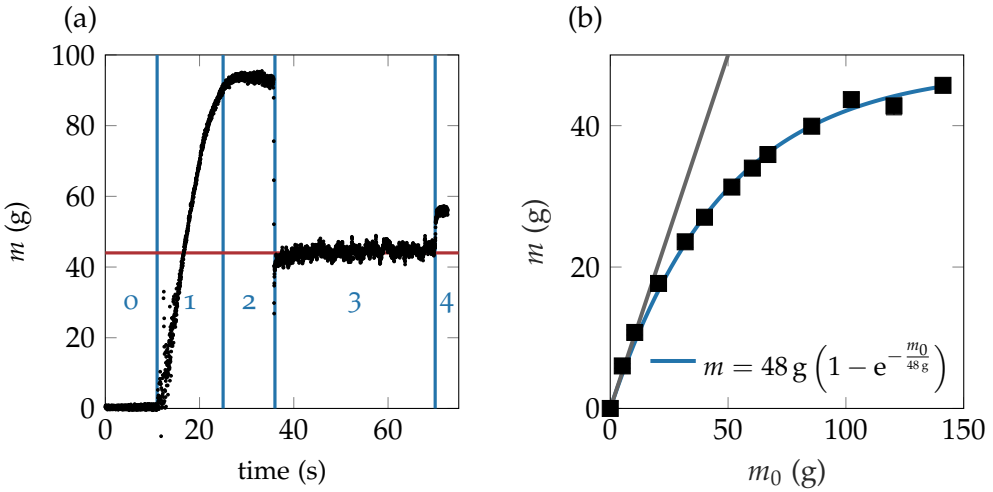

Figure 2.1: (a) Typical apparent mass measurement protocol inspired by [6]. (b) Typical experimental curve of the Janssen effect.

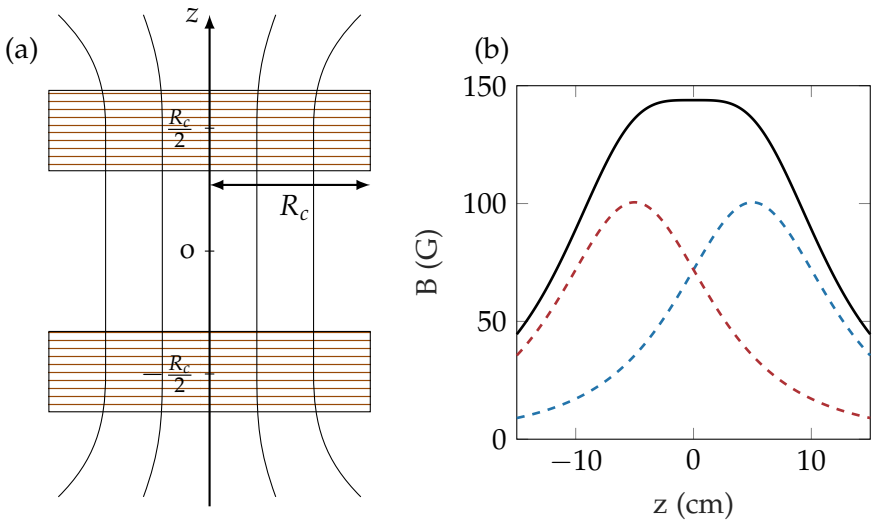

Figure 2.2: Helmholtz coils. (a) Helmholtz configuration where two identical coils of radius R_c are separated by a distance equal to their radius. (b) Magnetic field generated by the coils as the sum of both contribution and resulting in an uniform magnetic field between the two coils.

The complete magnetic Janssen apparatus, inspired by the one used in [6] and presented in section 1.1, is surrounded by the two coils as shown in figure (2.3). Due to the limitations of the Helmholtz coils configuration, the maximum packing height for which the magnetic field is homogeneous is $h_{\max} = R_c = 10\,\mathrm{cm}$, corresponding to a maximum packing mass $m_{\max} \approx 150\,\mathrm{g}$. The piston is moving downward at a constant velocity $v = 0.2\,\mathrm{mm}\cdot\mathrm{s}^{-1}$ over a distance $\delta h = 7\,\mathrm{mm}$ during which the mass plateau corresponds to the apparent mass measurement m. In our experiments we vary both the magnetic

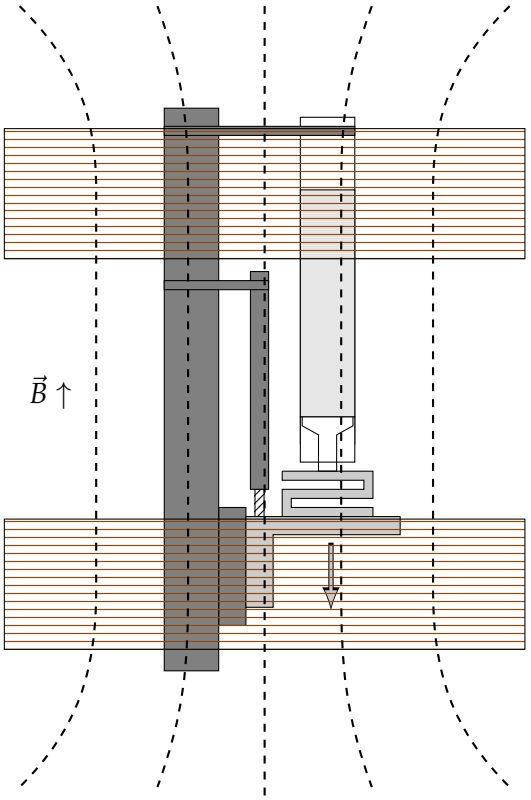

Figure 2.3: Experimental apparatus used in our study.

field amplitude up to a magnetic Bond number $\Psi_{max} \approx 35$, as well as its direction, either vertical or horizontal. For reasons that will be detailed later, we focus mainly on the vertical magnetic field direction in the following results.

2.2 RESULTS

Experimental measurements

A series of experimental apparent mass measurements for different magnetic field amplitudes is given in figure (2.4.a). Without any magnetic field we retrieve the classical Janssen prediction in black. By increasing the magnetic field amplitude we notice that the apparent mass of the packing decreases, suggesting an increase of the Janssen effect. For higher magnetic field amplitude we even notice a surprising "more is less" effect: when adding grains to the column, its apparent mass decreases! For the highest magnetic field, and by pushing the limits of our apparatus (packing higher than h_{max} set by the coils) the apparent mass even decreases to zero: the grains are stuck inside the silo and the column becomes undetectable with a zero apparent mass!
To quantify more precisely the effect of the magnetic field on the apparent mass of the packing, we examine the difference of our apparent mass measurements with the prediction of Janssen corresponding to the apparent mass of the column

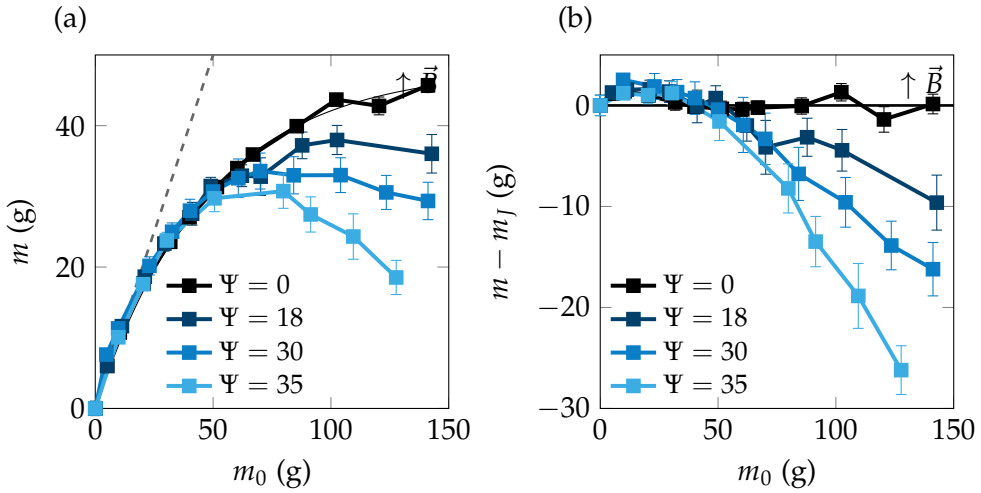

Figure 2.4: (a) Apparent mass of the packing submitted to different magnetic field strength Ψ. (b) Difference between the experimental results with the classical Janssen prediction m_J.

when no magnetic field is applied m_J. The results are shown in figure (2.4.b). We notice two different zones of interest. First for packing mass m_0 lower than 50 g, corresponding to a packing height $h = 2R$, the apparent mass seems to be slightly higher than the actual mass of the packing. This result appears similar to the reverse Janssen effect described in [12] though, without any specific preparation of the packing. Nevertheless, one should be aware that this overshoot is very small with an apparent mass about a few grams above the hydrostatic. Second, for packing mass greater than 50 g the difference decreases in a linear manner with a slope depending on the magnetic field strength.

Geometrical considerations

To rationalize our experimental results, we have to consider the magnetic pair-interactions inside the granular medium. Each particle i interacts with its neighbours j following the magnetic pair interaction $\vec{f}_{ij}$ given by equation (1.10). The total force exerted on particle i is given by the sum of all pair-interactions acting on it $f_i^\beta = \sum_j f_{ij}^\beta$, where $\beta = r, \theta, z$ gives respectively the radial, azimuthal and vertical component. We consider the granular packing as a whole; thus, the global magnetic force exerted on the granular packing is given by the sum of all the individual magnetic pair interactions $F^\beta = \sum_i f_i^\beta$. If we consider the cylindrical geometry of the system, and suppose the packing to be homogeneous, there is no azimuthal net force $F^\theta = 0$. Moreover, considering the symmetry of the system with respect to the mid-plane of the tube ($z = h/2$), two particles i and i' symmetric with respect to this plane will compensate each other, leading to no vertical net force at the packing scale $F^z = 0$. Therefore, thanks to the confined cylindrical geometry of our system, the only net force expected to emerge from those magnetic interactions should be in the radial direction $F^r \neq 0$.
If we consider a particle off the tube axis, as represented in figure (2.5), due

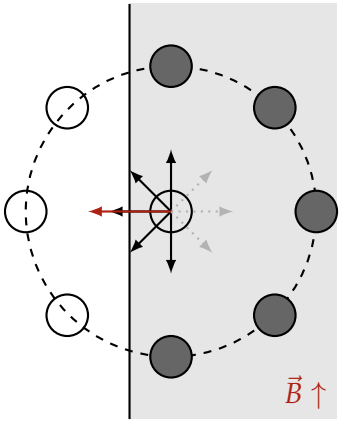

Figure 2.5: Neighbouring particles acting on an off-axis particle, resulting in a non-zero radial force.

to the finite size of the tube, this particle is missing some of its neighbouring particles, resulting in a radial net force applied to this particle.

Numerical solution

We have tried to obtain an analytical expression for the global radial force F^r without success. Instead, we developed a numerical computation of all individual pair-interactions using equation (1.10), and the positions of each particle within a random packing generated by a DEM simulation [32]. The packing generation, inspired by the protocol proposed in [61], is shown in figure (2.6). At each time step, a set of M grains are generated at a fixed height to the top of the packing, let to sediment by gravity, until the packing has reached the desired mass m_0. The packing fraction can be tuned by varying M. We found that $M = 20$ leads to a packing fraction $\phi \approx 0.6$ in accordance with our experiments.

Map force

To analyse the emergence of radial forces along the walls of the silo, we show in figure (2.7) spatial (r, z) maps of the radial component of the magnetic pair-interactions averaged over the angular component. The maps for different packing height h correspond to several values of interest of the global radial force F^r. For low masses $m < 30\,\mathrm{g}$, the magnetic interactions inside the packing are mainly attractive in the bulk and the force is slightly negative. For higher mass however, repulsive interactions emerge along the wall of the silo. The

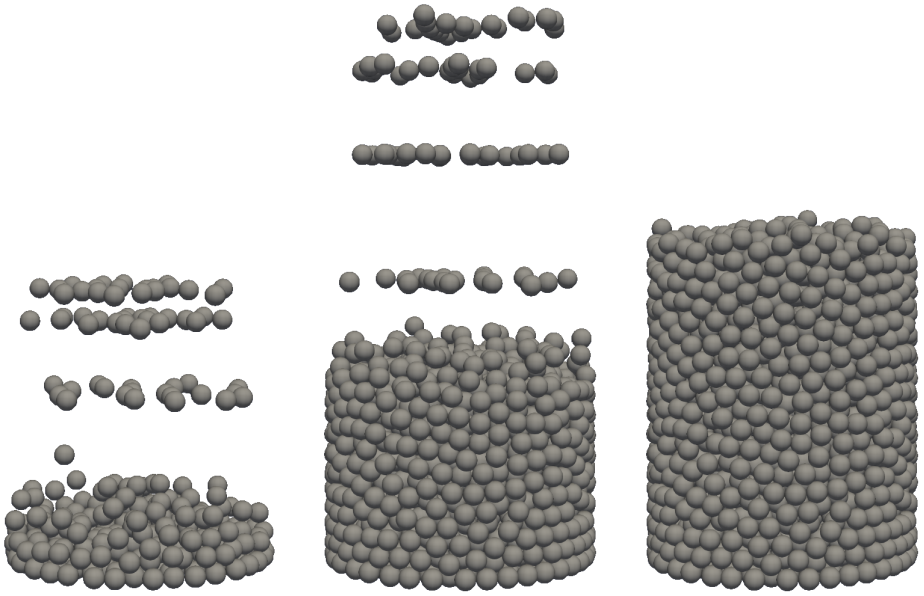

(a) (b) (c)

Figure 2.6: Random generation of a 3D beads packing in a geometry similar to the experiment, inspired by [61]. At each time step $M = 20$ particles are generated at a fixed height to the top of the packing and let to sediment.

radial repulsive force pushing against the tube wall is constant along the packing height (apart from top and bottom boundary effects). The global radial force is then increasing linearly with the amount of particles along the walls for high enough packing height $h > 2R$. The number of particles along the tube walls is proportional to the packing height h (or mass m_0). The attractive and repulsive interactions inside the packing compensate each other and $F^r = 0$ for a packing mass $m_0 \approx 30\,\mathrm{g}$, corresponding to a packing height $h = 2R$ with R the tube radius. Indeed, when the packing height corresponds to the tube diameter, no direction is favoured and the global radial force averages to zero.

Magnetic Janssen model

Following Janssen hypothesis, by considering the granular packing as a homogeneous continuous medium, and using the fact that the friction forces at the wall are fully mobilized in the vertical direction, the global magnetic radial force $F^r(h)$ can be associated with a vertical frictional contribution to the apparent mass measured at the bottom of the silo $F(h) = -\mu F^r(h)$. The negative sign comes from the fact that adding friction to the system lowers the apparent mass. This added pressure can be either compressive or tensile depending on the sign of $F^r(h)$, and the apparent mass of the packing at the bottom is tuned by the magnetic pair interactions:

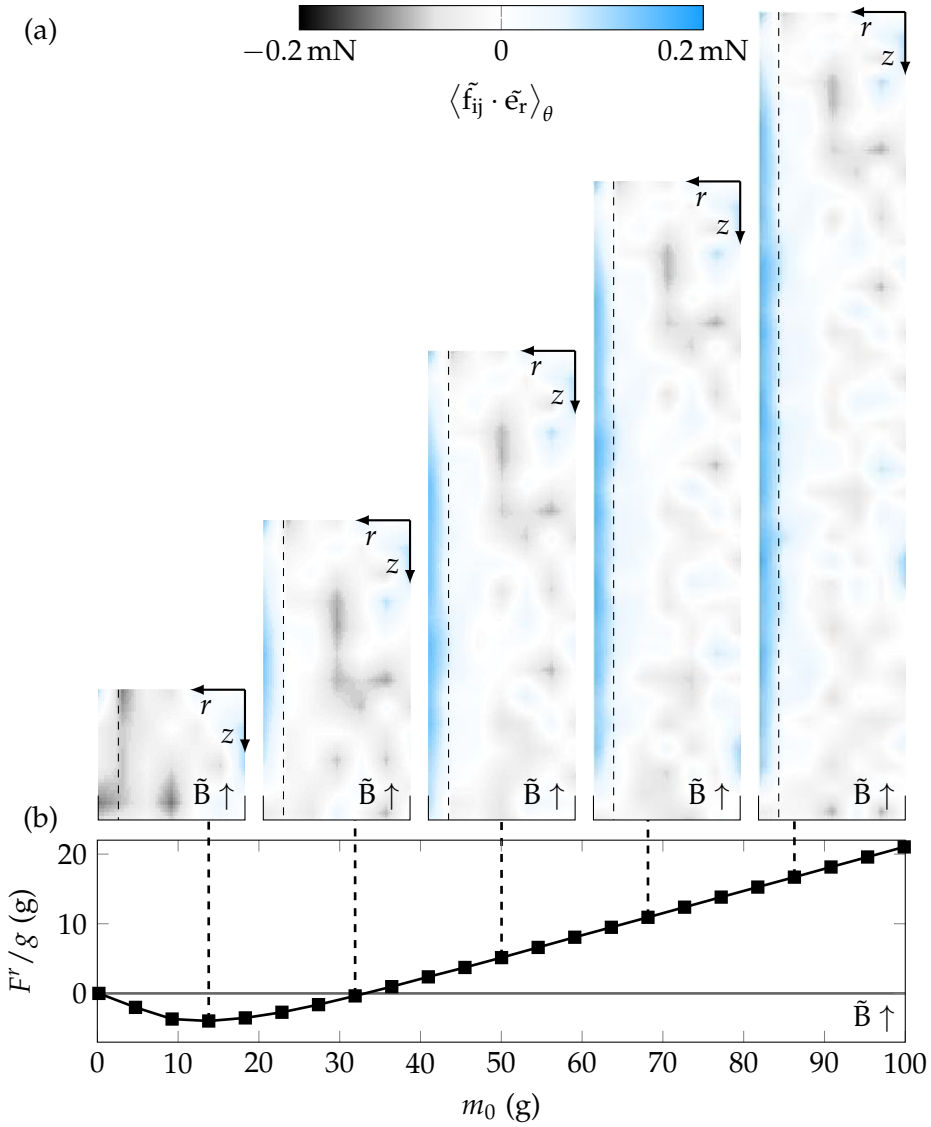

Figure 2.7: Maps of the radial force at different packing height (or mass), averaged in the θ direction for a vertical magnetic field. A blue region corresponds to a positive radial force (i.e. pressing on the wall of the container). The vertical dashed line within the packing represents a one bead diameter boundary from the silo wall. The radial force is observed mainly located along the boundary of the silo, for high enough columns $h > 2R$. For smaller ones, the radial force is mainly negative and distributed in the core of the granular packing

$$m = m_J - \frac{\mu}{g} F^r(h) \ . \tag{2.1}$$

The model curves resulting from the numerical solution are given in figure (2.8.a). We chose a friction coefficient corresponding to steel/copper contact $\mu = 0.40$. An excellent quantitative agreement is shown in figure (2.8.b), where we compare our experimental mass measurements to the prediction of our

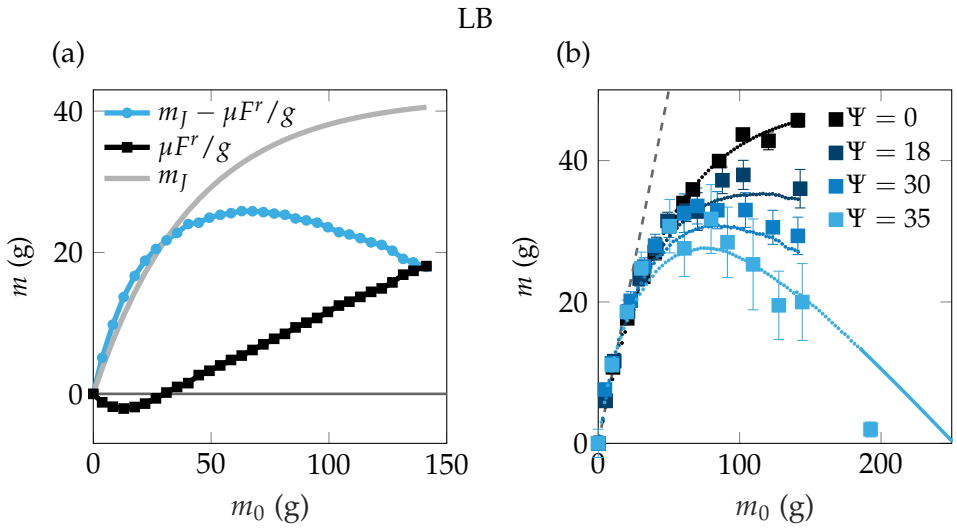

Figure 2.8: (a) Model curves, in light grey the classical Janssen prediction given by equation (1.5), in black the numerical solution for the global radial force F^r, in blue the resulting magnetic Janssen prediction given by equation (2.1). (b) Comparison of the experimental results to the magnetic Janssen prediction for a selection of magnetic Bond number Ψ. Squares correspond to the experimental results, small dots correspond to the numerical resolution.

model of a magnetic Janssen effect. Moreover, we can notice that our model also predicts a zone for low packing mass for which the apparent mass of the packing could be greater than its actual mass. Therefore, thanks to an applied magnetic field to the ferromagnetic granular column, we could control and tune this reverse Janssen effect, in contrast to the "classical" one reported in [12] which required a delicate filling protocol of the column.

Invisibility threshold

Moreover, our model also predicts the existence of a critical mass m_0^c for which the apparent mass of the packing is zero. As described above, the global radial force increases linearly with m_0 for high enough packing mass $m_0 > 30\,\mathrm{g}$. We then expect that the magnetic Janssen prediction is equal to zero for a large enough mass $m_0 = m_0^c$. At this point the granular packing is "invisible" at the bottom of the column and its weight is completely supported by friction with the silo wall.
For tall columns, the classical Janssen mass has reached its saturation value and we can write $m_J \approx m_\infty$, while $F^r \propto \Psi(m_0 - m_0^{2R})$, with $m_0^{2R} = 30\,\mathrm{g}$. Using these two expressions in the magnetic Janssen prediction (2.1), we end up with $m_0^c \propto m_\infty \frac{g}{\mu}\Psi^{-1}$. This prediction is compared to the numerical solution of the critical mass m_0^c in figure (2.9.a) and is found in excellent agreement. However, this packing mass is beyond the experimentally reachable values set by the limits of our experimental set-up. Indeed, we recall that the maximum reachable magnetic field in our case is $B_{\max} = 170\ G$ corresponding to $\Psi_{\max} = 35$, while granular columns of height greater than $h_{\max} = 10\,\mathrm{cm}$ (corresponding to a packing mass of approximately 150 g) experiences inhomogeneous magnetic

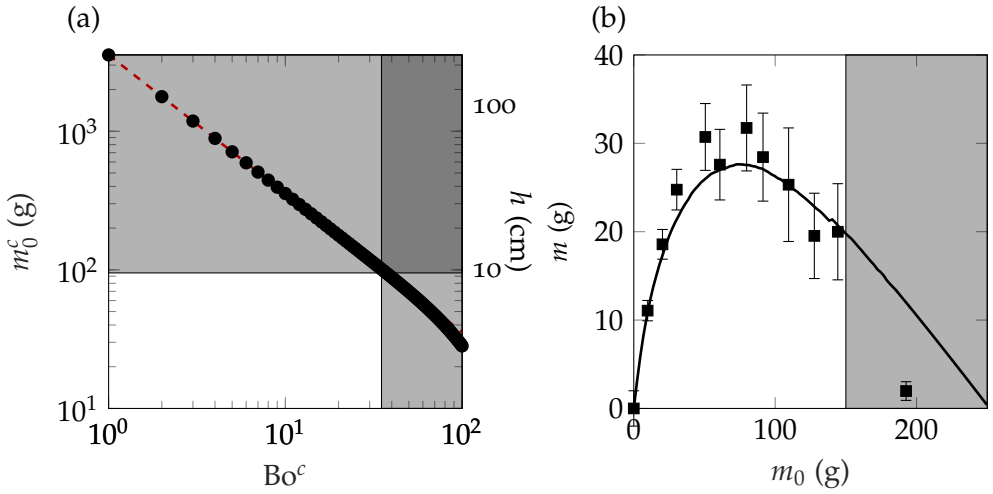

Figure 2.9: (a) Numerical computation of the critical mass m_0^c, for which the apparent mass of the packing is zero, as a function of the magnetic field strength Ψ. The grey zones represent the mass and magnetic field intensity that cannot be reached by our experimental apparatus, while the red dashed line corresponds to our theoretical prediction. (b) Apparent mass measurement for the highest magnetic field intensity, applied vertically, and comparison to our model (black line).

field. The experimental limitations are displayed by the grey area in figure (2.9). Nevertheless, we performed one apparent mass measurement for a tall column $h = 15\,\text{cm}$, corresponding to a packing mass $m_0 = 200\,\text{g}$. We could observe that, in these conditions, the apparent mass is close to zero and the granular column is "undetectable", in agreement with our prediction. This measurement is smaller than the theoretical one $m_0^c = 250\,\text{g}$, certainly due to the inhomogeneity of the magnetic field in this case.

Tunability of the magnetic Janssen effect

To highlight the tunability of the magnetic Janssen effect, we turned off the magnetic field during an apparent mass measurement as shown in figure (2.10), for a packing mass $m_0 = 60\,\text{g}$. The magnetic field is on to its maximal value $\Psi = 35$, where the apparent mass equals to the magnetic Janssen prediction. The magnetic field is turned off after 15 s and increases sharply to reach its value $m = m_J$.

Friction coefficient

Throughout our study, we have kept the friction coefficient value μ fixed and equal to 0.40, in agreement with reported values from the literature for steel/copper contact. However, this friction coefficient may have a slightly different value depending on specificities of the grains' material, which would modify accordingly those slopes: $m - m_J = -\mu F^r/g$. Keeping the friction coefficient μ as a free parameter, figure (2.11) shows that if we fine tune the

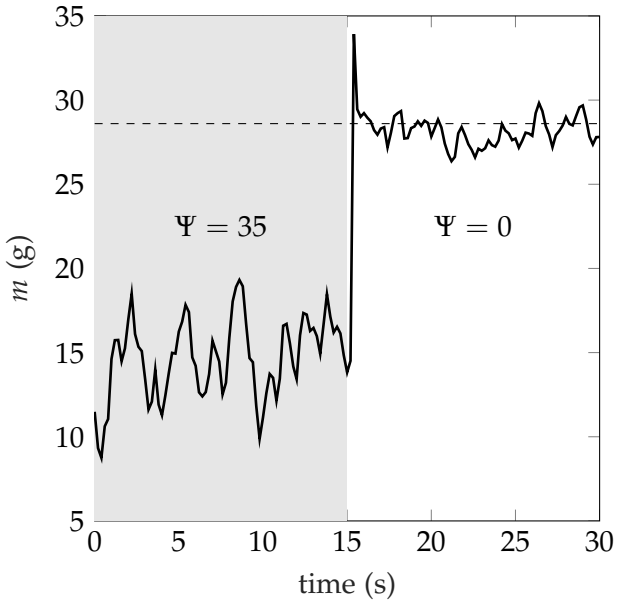

Figure 2.10: The magnetic field is switched-off during an apparent mass measurement (piston moving downward). The apparent mass jumps from the magnetic Janssen prediction to the classical Janssen prediction m_J.

value of the friction coefficient, an almost perfect agreement between the model and the specific experimental data set for a vertical magnetic field and $\Psi = 30$ can be found for $\mu = 0.35$. However, we checked that the value $\mu = 0.40$ fits better our overall measurements, performed in various conditions (different column heights, different amplitude and direction of the magnetic field).

Influence of the tube geometry and magnetic field direction

We investigate here the impact of the system parameters (tube size and magnetic field direction) on the magnetic Janssen prediction with the help of our numerical tool.
Firstly, we varied the tube radius in our numerical solution, while keeping the packing height h constant. For each radius we generated five packings using the DEM simulations and averaged the results over these realizations. In this case, the magnetic field is in the vertical direction with a magnetic Bond number $\Psi = 35$. The resulting global radial force F^r for different tube radii are shown in figure (2.12.a). The packing mass m_0^{2R}, for which the global radial force is equal to zero, increases with the tube radius R. We previously stated that m_0^{2R} corresponds to a packing height $h = 2R$, to verify this statement we simply translated our measurement in terms of packing height $h^{2R} = m_0^{2R}/(\pi R^2 \phi \rho)$ as shown in figure (2.12.c) where we can note that m_0^{2R} is found slightly higher than our prediction for the largest radii.
Figure (2.12.b) shows the expected rescaled mass m_0/m_∞ and m/m_∞ where the classical Janssen expression is set according to the tube radius dependency on the saturation mass given by $m_\infty = (\rho \pi R^3)/(2K\mu)$. In this case the classical Janssen effect is independent of the tube radius and given by

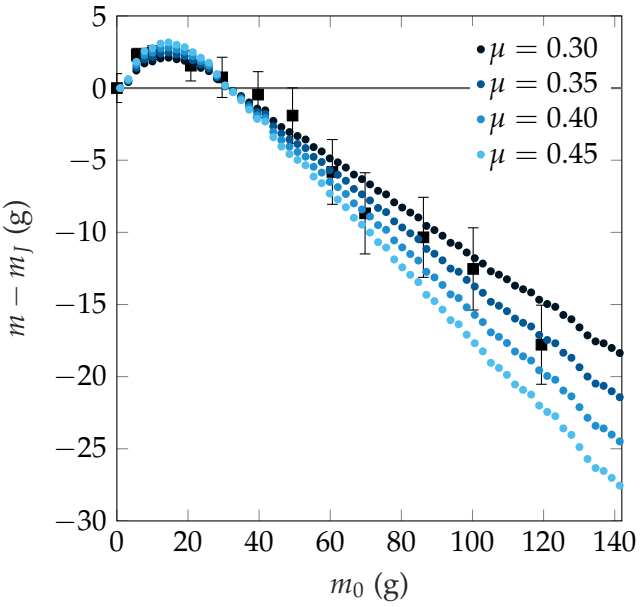

Figure 2.11: Influence of the friction coefficient. The difference between experimental data points at $\Psi = 30$ and classical Janssen prediction m_J is compared to the numerical solution where we varied the value of the friction coefficient. The best fit is found for $\mu = 0.35$ in this case.

$m/m_\infty = 1 - \exp(-m_0/m_\infty)$. We can easily compare the results for different tube radius, which is predominant for smaller tube radius. To quantify this result we are interested in the linear decrease of $\mu g F^r$ with m_0, as defined and shown in figure (2.12.a). If we consider, as previously shown, that for high enough packing mass m_0 the magnetic pair interactions are mainly situated along the tube wall and roughly constant there, we can suppose that the global radial force F^r is linear with the number of particles along the walls $N_{\text{wall}} = 2Rh/a^2$. If we define f_0^r the standard magnetic pair interaction on the wall, we can write $F^r = N_{\text{wall}} f_0^r + \text{cst} = 2Rhf_0^r/a^2 + \text{cst}$. The constant comes from boundary effects for $m_0 < 30\,\text{g}$. By translating this expression in terms of the packing mass m_0, we end up with:

$$F^r = \frac{2m_0 f_0^r}{\pi R \phi \rho a^2} + \text{cst}. \tag{2.2}$$

This expression is found in excellent agreement with our numerical computations, as shown in figure (2.12.d). We can conclude that the magnetic Janssen effect prevails the classical one for small tube radii. Nevertheless, for an even smaller tube radius we would have to also take into account the fact that the classical Janssen value m_J is modified as discussed in [11].

Secondly, we varied the magnetic field characteristics to identify their influence on the resulting magnetic Janssen. According to the expression of eq. (1.10), the magnetic pair interaction is proportional to d^2, with d the dipolar moment

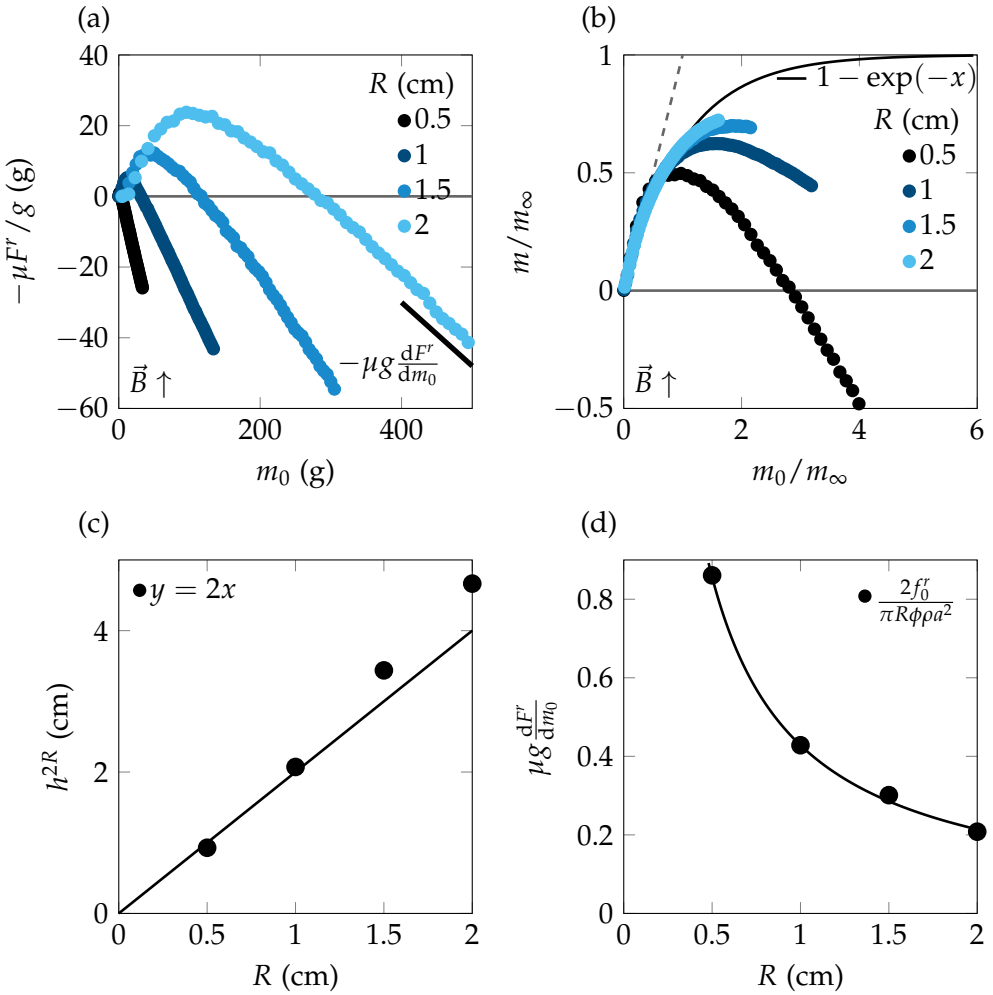

Figure 2.12: Numerical solution for the magnetic Janssen effect for different tube radius. (a) Global radial force contribution to the apparent mass. (b) Apparent mass of the granular column normalized by the saturation mass m_∞ compared to the normalized packing mass m_0/m_∞. The narrower the tube, the stronger the magnetic Janssen effect. (c) Prediction of the packing h^{2R} for which the global radial force is zero. (d) Slope of the linear evolution of the global radial force with the packing mass m_0.

amplitude. We define $\overline{F^r} = F^r(d = 1\,\mathrm{A\cdot m})$ the global radial force for a unit dipolar moment, used to rewrite the magnetic Janssen effect:

$$m = m_J - \frac{\mu}{g}\overline{F^r}d^2\,. \tag{2.3}$$

We then use the definitions of the magnetic Bond number $\Psi = (\chi_m^2 B^2)/(\mu_0 a \rho g)$ and the magnetic moment $d = V\chi_m B/\mu_0$ to rewrite the magnetic Janssen effect prediction:

$$m = m_J - \mu\overline{F}^r \Psi a \rho \mu_0 \left(\frac{4}{3}\pi a^3\right)^2, \tag{2.4}$$

Following this expression, the magnetic field amplitude, given by Ψ, is acting as a scaling factor on the global radial force, and therefore a unique understanding of the effect for a unit dipolar moment $d = 1\,\mathrm{A}\cdot\mathrm{m}$ leads to the final expression of the magnetic contribution to the apparent mass of the packing. However, the field direction is more of importance in the magnetic Janssen effect. We computed the numerical solution of the global radial force F^r for different angle β of the magnetic field with the horizontal, which, thanks to the symmetry of the problem and the parity of Ψ, can be done only for β between 0° and 90°. The numerical results are shown in figure (2.13.a). The global radial force F^r evolves continuously with the field angle with its minimum for high packing mass $m > m_0^{2R}$ found for a vertical field and the maximum for a horizontal field. Moreover, we notice that the zero-point of the global force at $m_0 = m_0^{2R}$ is found to be always the same without any dependence on the angle. Because the global radial force goes from negative to a positive values while changing the field direction, it exists an angle where this global radial force is roughly equal to zero. This magnetic field angle is found to be at $\beta \approx 35^\circ$, corresponding to the attractive-repulsive border shown in figure (2.3.b). This means that if the magnetic field is aligned with the ferromagnetic interaction dipolar border, the magnetic Janssen is null, and we only find the classical Janssen effect regardless the amplitude of the magnetic field. Finally, figure 2.13b shows the apparent mass of the column as a function of the packing mass m_0 for different magnetic field angles following expression (2.4). We moreover compare, in figure (2.14), such numerical results to experimental measurements obtained for a magnetic field applied either horizontally or vertically. Other magnetic field angles with the vertical are hardly possible experimentally. We can conclude that to maximize the magnetic Janssen effect, ones has to align the magnetic field with the direction of the tube along with $\vec{g}$. Since the maximum of the magnetic Janssen effect is found for a vertical magnetic field, we decided to focus on this configuration for the following studies.

2.3 FERROMAGNETIC / NON-FERROMAGNETIC MIXTURE

A potential application of the magnetic Janssen effect may be found in the use of a mixture made of both ferromagnetic and non-ferromagnetic grains. Throughout this section, we kept the magnetic field vertical and at the highest amplitude, $\Psi = 35$. The tube radius $R = 1\,\mathrm{cm}$ is constant, but we varied the amount of ferromagnetic particles characterized by the fraction $\phi_m = N^m/N$, where N^m and N are respectively the number of ferromagnetic particles and total number of particles inside the packing, as well as their spatial distribution.

Experimental preparation of the packing

Before any experiments, we prepared in advance a mixture of ferromagnetic and non-ferromagnetic grains at the desired ϕ_m concentration. One should be careful when preparing a random distribution of grains. Indeed, in commonly used grains, ferromagnetic and non-ferromagnetic particles are usually of a very different density. For instance, in [43], the mixture was composed of magnetic

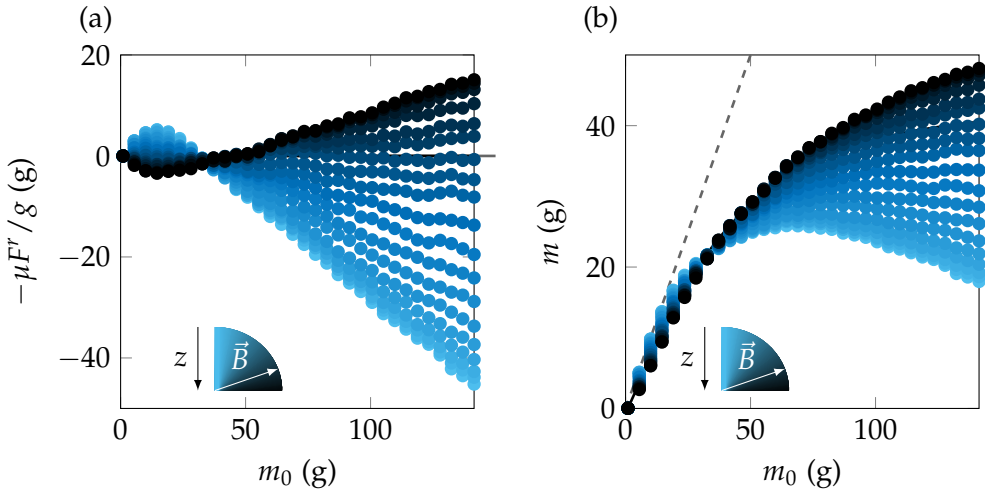

Figure 2.13: Magnetic Janssen for different magnetic field direction for $\Psi = 35$. (a) Global radial force contribution to the apparent mass, the contribution is zero for a magnetic angle to the vertical $\alpha = 55\,^\circ$. (b) Apparent mass of the granular column, for a horizontal magnetic field the magnetic Janssen effect is above the classical Janssen prediction.

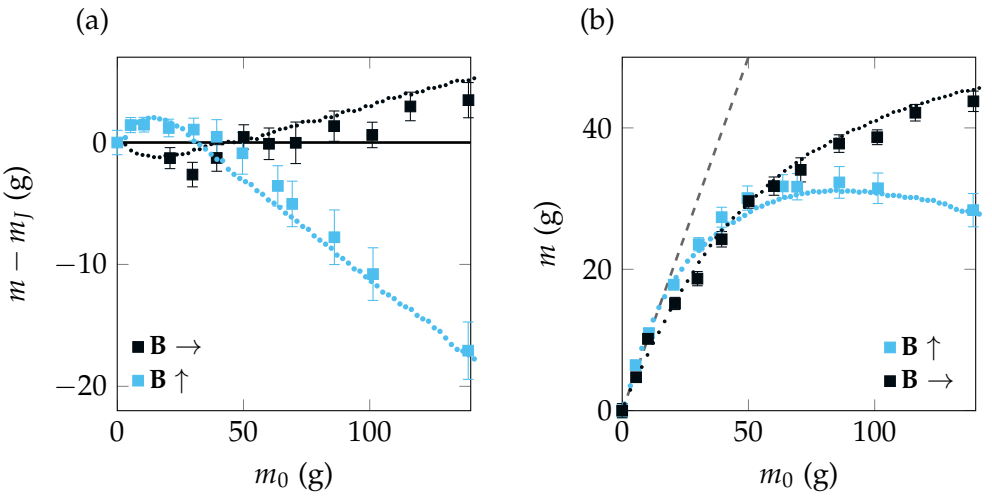

Figure 2.14: Experimental results for a vertical and horizontal magnetic field for $Psi = 30$. (a) Difference between the apparent mass and the classical Janssen prediction m_J. (b) Apparent mass measurement.

grains (typically steel or iron of density $\rho_{\text{mag}} \approx 8\,\text{g}\cdot\text{cm}^{-3}$) and glass beads of density $\rho_{\text{glass}} \approx 2\,\text{g}\cdot\text{cm}^{-3}$. Such a huge density difference can lead to unwanted density driven segregations [62–64] as shown in figure (2.15) and jeopardize the realization of a truly random mixed packing. To avoid such problems, we have decided to use a mixture of beads similar in size, shape and density with the only difference being their magnetic properties. We used, as ferromagnetic component, 1.50 mm diameter 100C6 steel grains, and as non-ferromagnetic, 1.50 mm diameter 316-L steel grains. The density difference between these materials is about 2%. The mixture was prepared in advance by checking the

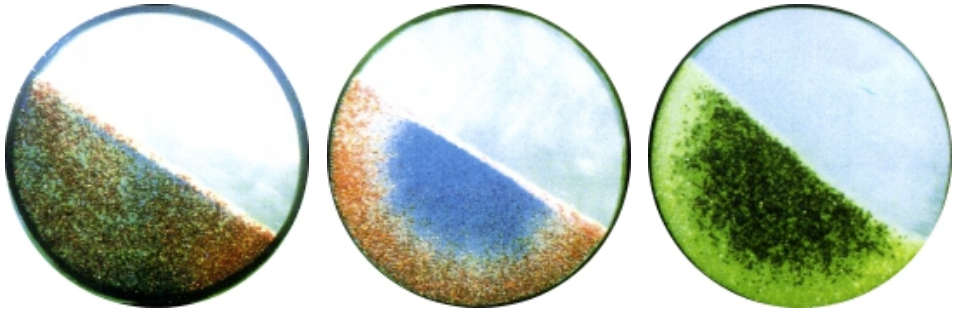

(a) (b) (c)

Figure 2.15: Granular segregation, pictures from [62]. (a) Initial distribution of grains in a rotating drum. (b) Size-driven particle segregation after a few rotations of the drum. (c) Density-driven segregation of the particles after a few rotations of the drum.

mass concentration of both types of grains and shaken vigorously afterwards to achieve a random distribution.

Results

We show in figure (2.16) the apparent mass measurements of columns composed of a mixture of ferromagnetic and non-ferromagnetic particles, prepared at different concentrations ϕ_m, while other system parameters are kept constant. For the numerical solution of the magnetic Janssen effect, we selected for each ϕ_m a random list of N^m grains inside the packing and computed the pair interactions only on this limited random collection of positions inside the packing. To avoid any bias on the final result that could be induced by the random process, we averaged the computation of the total radial force F^r on a series of 10 random collections for each ϕ_m. Our numerical prediction of a magnetic Janssen effect adapted to the mixture case with a randomized positioning of the ferromagnetic particles appear in rather good agreement with our experimental results. Nevertheless, up to a fraction of ferromagnetic particles $\phi_m \approx 0.5$, the magnetic Janssen effect is really mild. Indeed, with our experimental conditions, and the maximum mass (m_0) of the packing we can reach, we cannot really distinguish the prediction of the classical Janssen approach and the one of our magnetic Janssen model. If numerically, one can observe a systematic deviation and a decrease in the apparent mass of the column when the fraction ϕ_m of ferromagnetic particles increases, up to $\phi_m \approx 0.5$, such a mass difference is lower than the experimental dispersion and the typical measurement error. Interestingly, at $\phi_m = 0.55$, we observe a transition, where the measured mass of the (highest) column is clearly smaller than the values predicted by the Janssen model, in agreement with our numerical prediction. Notice that our experiments at a given ϕ_m were performed only once, and several realizations in the same conditions would be needed to clarify such transition. To identify the origin of this transition we are going to examine the internal structure of the packing, and specifically, the spatial distribution of the ferromagnetic particles inside the packing.

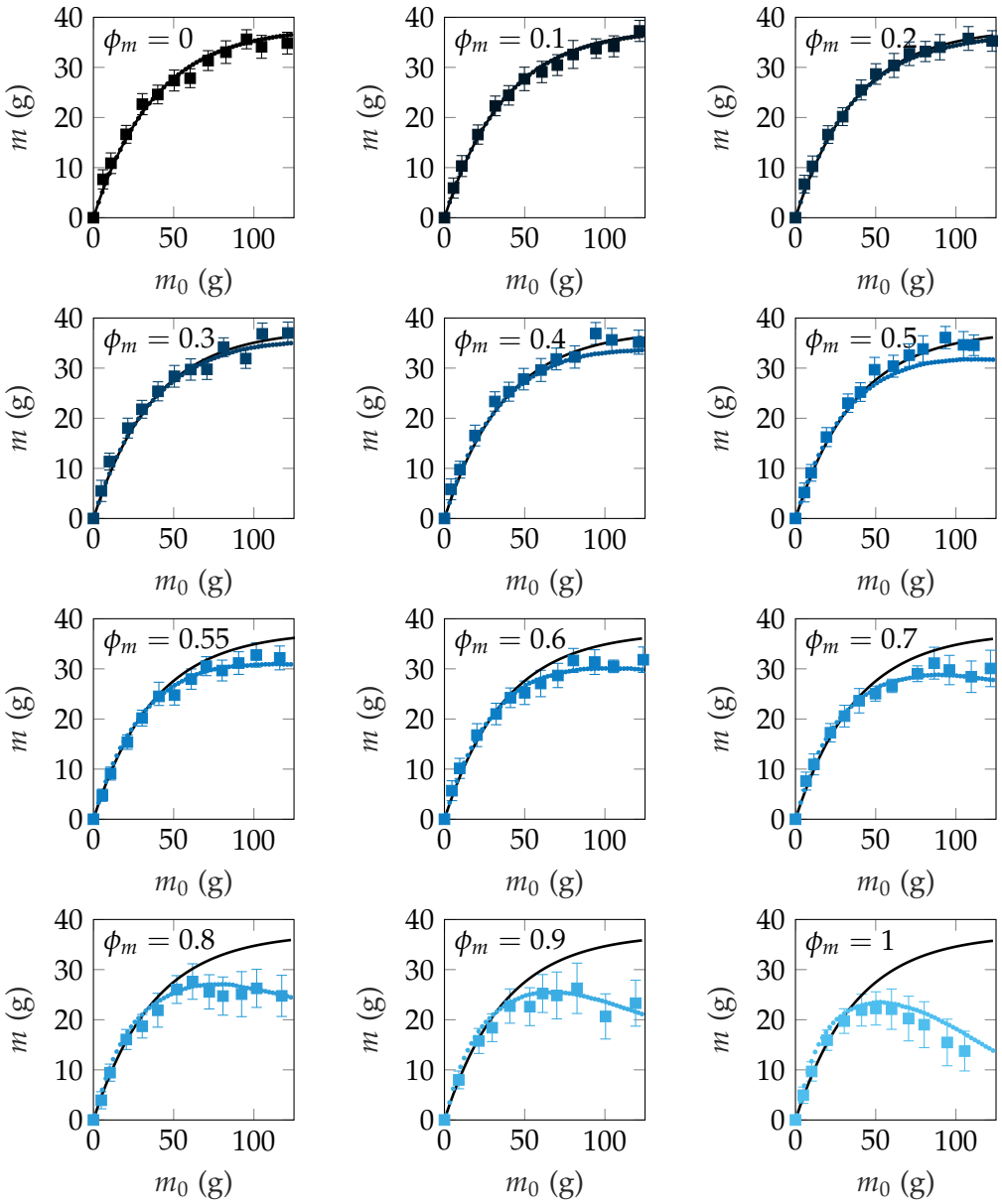

Figure 2.16: Apparent mass measurements as a function of the true mass of the packing m_0, for various ferromagnetic fraction ϕ_m. The higher the concentration, the greater the magnetic Janssen effect, nevertheless one can notice a transition for $\phi_m \approx 0.5$ below which the apparent mass curve follows the classical Janssen prediction.

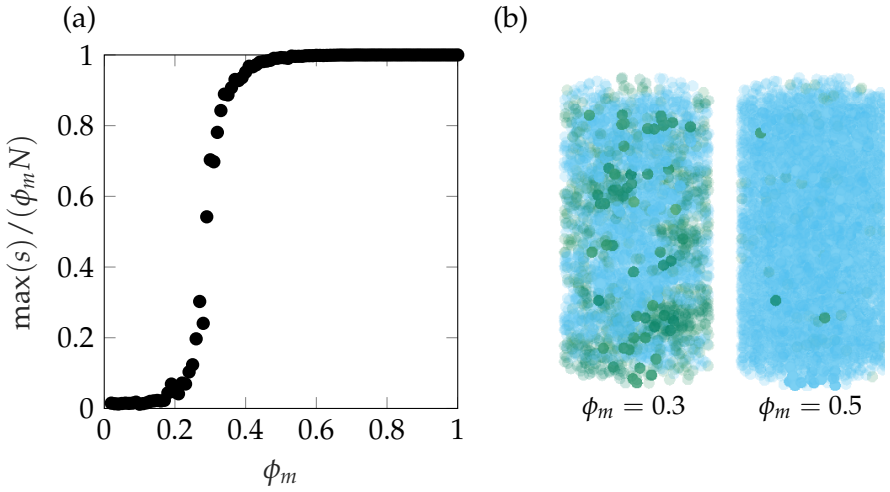

Figure 2.17: (a) Size the biggest cluster normalized by the total number of ferromagnetic particles in the packing, we observe a transition around $\phi_m = 0.4$. (b) Clusters representation inside the packing. The biggest cluster is represented in blue while smaller clusters are represented in green, non-ferromagnetic particles are not shown. We note that for $\phi_m = 0.3$ this cluster is in contact with the boundaries of the silo, but several smaller clusters remain not connected.

Magnetic clusters

For each magnetic particle, we identify its magnetic neighbours in contact (distance between the two particles lower or equal to $2a$). As in percolation description [65], we identify each cluster with its size s, and we compute the associated number of clusters of this size n_s. Figure (2.17.b) shows the size s of this biggest ferromagnetic cluster present in the packing, normalized by the total number of ferromagnetic particles N^m. One can observe that there exists a clear transition around $\phi_m = 0.4 - 0.5$ where the packing consists of one connected cluster containing all the ferromagnetic particles. Using this description, the packing can be considered almost homogeneous if is made of a unique cluster of connected ferromagnetic grains, meaning that the biggest cluster of size $\max(s)$ is equal to the total number of ferromagnetic particles in the packing $\phi_m N$, with the presence of non-ferromagnetic defects.
Figure (2.17.b) gives a representation of the ferromagnetic particles distribution inside the packing with, in blue the biggest ferromagnetic cluster, and in green the particles not connected to this cluster. One can see that for ferromagnetic concentration $\phi_m = 0.3$, the biggest cluster is about the size of the packing and touches the silo walls but does not contain all ferromagnetic particles. For a ferromagnetic concentration of $\phi_m = 0.5$, the packing consists of one big connected ferromagnetic cluster with the presence of non-ferromagnetic defects. We conclude that the connectivity of the ferromagnetic particles is the relevant parameter for the magnetic Janssen effect to appear, with their connection to the tube wall.

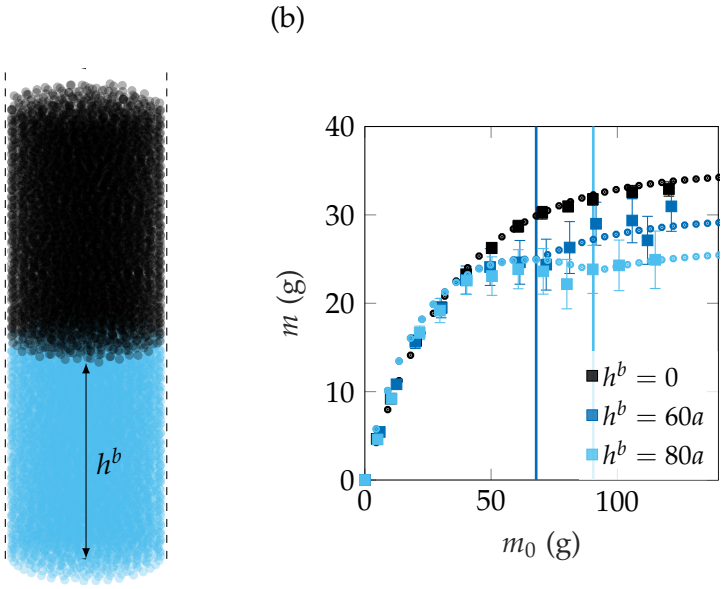

Figure 2.18: Magnetic Janssen for a buffer distribution. (a) Buffer distribution characterized by the buffer height h^b. (b) Apparent mass of the packing for different buffer height where the transition from magnetic Janssen to classical Janssen effects occurs at a packing mass m_0 equals to the buffer mass.

Other intern structures of the ferromagnetic particles

We propose now to investigate specific spatial structures of the assembly of ferromagnetic particles within the packing. Indeed, the positioning of ferromagnetic and non-ferromagnetic grains can be chosen wisely in order to affect the apparent mass of the packing in a more controlled way than just a random mixture.
We propose to study experimentally a "buffer" situation where all ferromagnetic particles are placed at the bottom of the packing, as shown in figure (2.18.a), characterized by the buffer height h^b given in terms of grains radius a. The experimental mass measurements are compared to the numerical solution in figure (2.18.b) and are in good accordance. For a packing mass lower or equal to the buffer mass, the apparent mass of the packing follows the magnetic Janssen prediction. For a packing mass higher than this limit we observe a transition to the classical Janssen prediction shifted by an offset corresponding to the global radial force contribution of the magnetic buffer. For high packing mass, the apparent mass of the column saturates as predicted by the classical Janssen prediction, but the saturation mass is tuned by the buffer height:

$$m_\infty = m_\infty^0 - \frac{\mu}{g} F^r\left(h^b\right) \ , \tag{2.5}$$

where m_∞^0 is the classical Janssen saturation mass depending only on the geometry and density of the packing.

Finally, the numerical resolution allows us to study other spatial distribution of the ferromagnetic and non-ferromagnetic particles within the packing not yet experimentally investigated. Among others, we propose to study a radial

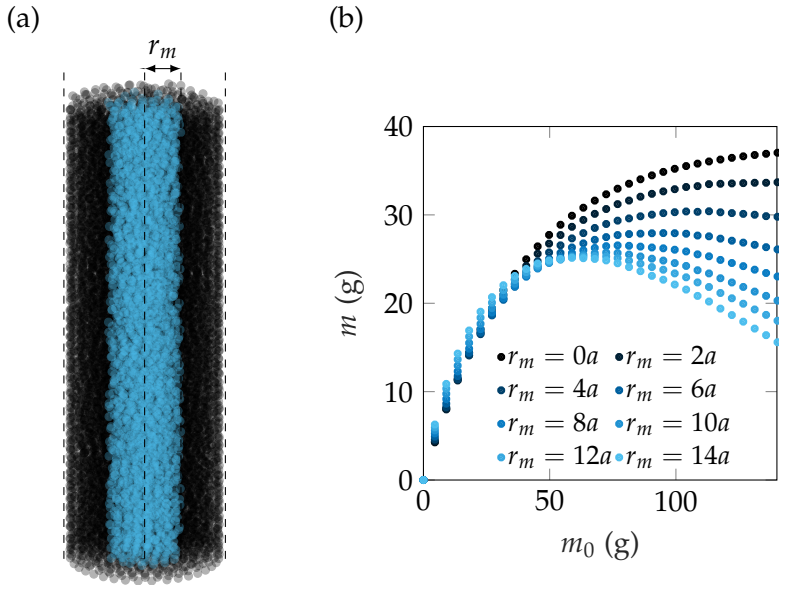

Figure 2.19: Magnetic Janssen for a radial distribution. (a) Radial distribution characterized by the ferromagnetic radius r_m. (b) Apparent mass of the packing for different ferromagnetic radius obtained by the numerical resolution.

arrangement of ferromagnetic particles, as shown in figure (2.19.a). All ferromagnetic particles are placed within a radius smaller than the tube radius characterized by the ferromagnetic radius r_m. The numerical results are shown in figure (2.19.b) and as expected, the smaller the ferromagnetic radius, the smaller the magnetic Janssen effect. Experimental study is expected in future work where the preparation can be achieved using a double funnel filling of the experiment. Experiments on the radial distribution of ferromagnetic particles would let us conclude if their connectivity is the key parameter for the presence of the magnetic Janssen effect over their contact with the tube wall.

3

PERSPECTIVES ON MAGNETIC GRANULAR MEDIUM DYNAMICS

In this chapter we present preliminary results obtained during two distinct experimental studies where we started to investigate the dynamical behaviour of magnetic granular media. The observations are still under investigation but already display interesting phenomena. First, we will discuss the dynamic response of a ferromagnetic granular column when a periodic magnetic field is applied. Second, we study the discharge of a silo filled with magnetic grains and submitted to a magnetic field.

3.1 MAGNETIC FATIGUE OF THE GRANULAR COLUMN

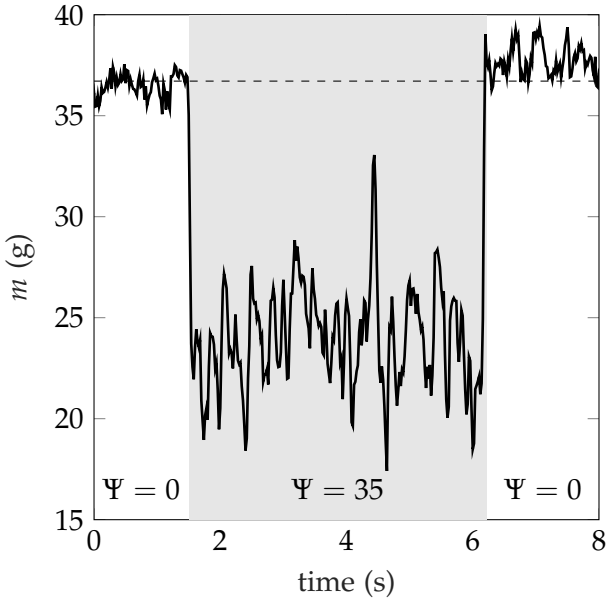

Figure 3.1: The vertical magnetic field of amplitude $\Psi = 35$ is switched on and off during an apparent mass measurement of a column of $m_0 = 60\,\mathrm{g}$ (piston moving downward). The apparent mass jumps from the classical Janssen prediction $m_J = 37\,\mathrm{g}$ to a lower value $m = 22\,\mathrm{g}$ predicted by our "magnetic Janssen" model. When the magnetic field is turned-off again, the measured apparent mass appears slightly higher than m_J.

To highlight the tunability of the magnetic Janssen effect, the magnetic field was turned on and off during an apparent mass measurement. Here, we go further by applying the same method periodically on the granular column. Figure (3.1) displays an apparent mass measurement where the vertical magnetic field of maximum amplitude $\Psi = 35$ was turned on during the piston movement and quickly (a few seconds later) turned off again. At first, the apparent mass of the column of mass $m_0 = 60\,\mathrm{g}$ corresponds to Janssen pre-

diction $m_J = 37\,\mathrm{g}$, followed by an abrupt decrease when the magnetic field is turned on. The new apparent mass $m = 22\,\mathrm{g}$ corresponds to our magnetic Janssen prediction. One can note that the fluctuations on the measurement at this point increases. An analysis of its spectrum did not reveal any predominant frequency. The magnetic field is turned off a few seconds later and the apparent mass increases sharply. Interestingly, one can notice that the measured apparent mass is now slightly higher than the classical Janssen prediction m_J. A hysteresis seems to emerge when applying a magnetic field to the column. Such observation led us to the following study, where we investigate the dynamic response of the granular column when the magnetic field amplitude varies periodically.

Aging of the granular column

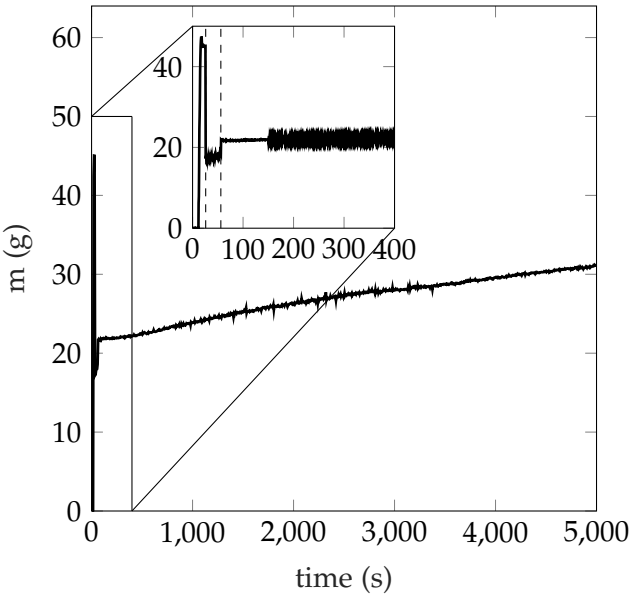

Figure 3.2: Typical aging of the granular column. The apparent mass measurement is carried on after the Janssen apparent mass estimation when friction forces are mobilized in the vertical direction (inset). The apparent mass of the granular column keeps increasing once the piston stops its downward movement.

Before going any further, we must describe the dynamics of the apparent mass of the column without any magnetic field. The measurement of the apparent mass of the column was carried out during a long period of time of 5000 s, and the results are shown in figure (3.2). As the onset displays, as a first step we made an apparent mass measurement following the protocol to measure properly the Janssen effect, by mobilizing vertically the friction along the walls. The silo is filled with a fixed amount of grains $m_0 = 50\,\mathrm{g}$ and the piston moves downward decreasing sharply the apparent mass of the column. Once the piston stops its movement, the apparent mass of the column increases slightly, due to the inertia of the grains. The apparent mass measurement continues for a longer period and, as one can see, the apparent mass of the

column increases slightly over time. We recall that during this period of time the piston does not move, breaking Janssen hypothesis (i). This increase is considered to be a natural aging of the column and could emerge from small perturbation of temperature or vibrations. On a period of 5000 s, the apparent mass rises from $m = 21\,\mathrm{g}$ to $m = 31\,\mathrm{g}$ at a roughly constant rate. For a short period of time up to $t = 400\,\mathrm{s}$, due to the slow aging dynamics, the apparent mass is almost constant. In this study, we focus on the fast magnetic fatigue dynamics, of maximum a few minutes, so that our measurements should not be impacted by the slow natural aging of the column.

Typical magnetic fatigue of the column

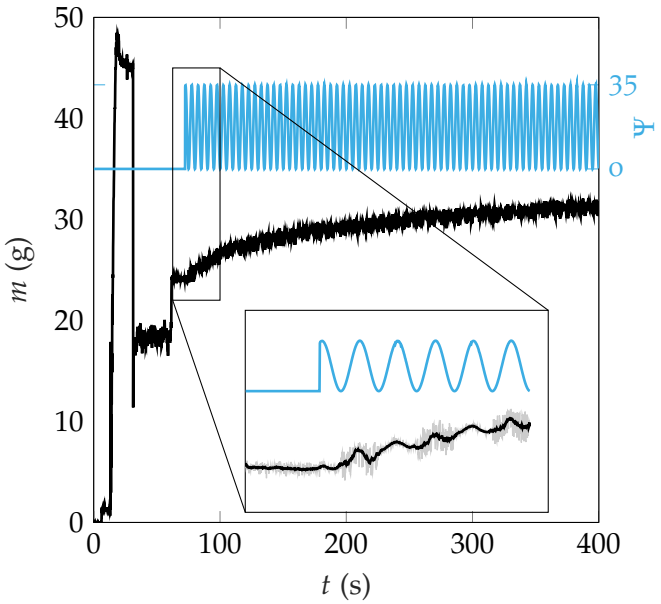

Figure 3.3: Typical magnetic fatigue of a granular column of mass $m_0 = 60\,\mathrm{g}$. The apparent mass, in black, is measured during a Janssen effect experiment followed by a oscillating magnetic field of amplitude $A = 170$ G and frequency $f = 0.1\,\mathrm{Hz}$, shown in blue.

In figure (3.3) we show the apparent mass evolution when applying a sinusoidal magnetic field. As before, the apparent mass measurement is carried on after the protocol to measure properly the Janssen effect (friction forces mobilized in the vertical direction). A few seconds after the piston stopped its movement, at $t = t_0$, an oscillating magnetic field (applied vertically to the column) is turned on, characterized by a sinus wave of frequency f and amplitude A, $B = A\sin(ft)$. Interestingly, we observe that the apparent mass at the bottom of the tube increases of around 5 g in about 200 s. During the whole measurement, no change in the height of the packing has been measured, leading us to the conclusion that the resulting behaviour of the packing is not a compaction phenomenon in contrast to some results reported in the literature (with temperature cycles or direct mechanical perturbation of the column [27, 29]). The friction forces between grains and the tube wall are not mobilized

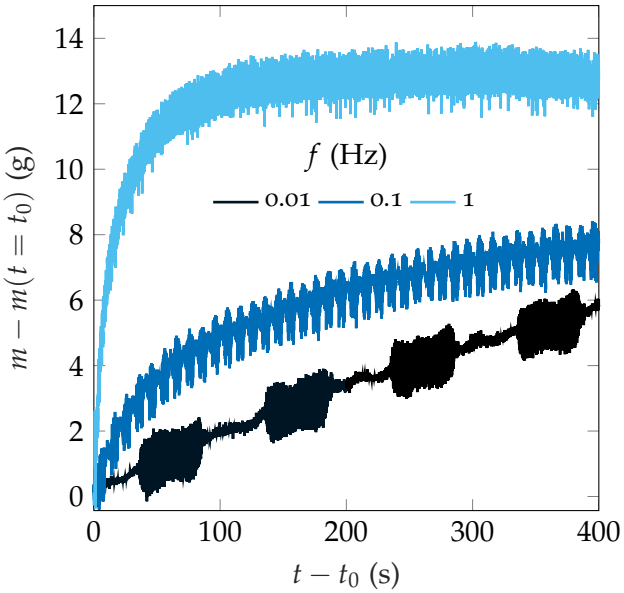

Figure 3.4: Apparent mass of the granular packing evolution for different frequency oscillations.

in the vertical direction, as imposed by Janssen hypothesis (i), the packing mass is less supported by the walls leading to an increase of the packing mass. Moreover, as in the inset in figure (3.3) shows, the apparent mass increases and decreases in phase with the magnetic field oscillations. The apparent mass during a cycle is maximum when the magnetic Bond number Ψ is maximum, and minimum when Ψ is. Again, the apparent mass measurement displays strong fluctuations when the magnetic field is high. The origin of this noise (suspected to be electronic) still needs to be addressed.

Magnetic response of the granular column for different magnetic field frequencies

We investigate here the magnetic fatigue of the granular column for different frequencies of the magnetic field cycle. Figure (3.4) shows the apparent mass measurement, focused on the fatigue process, $t \geq t_0$, for different magnetic field frequency $f = 0.01, 0.1, 1\,\mathrm{Hz}$ with a maximal magnetic field amplitude $\Psi = (\chi_m^2 A^2)/(\mu_0 a \rho g) = 35$. The maximum frequency imposed to the system is set by the coil cut-off frequency given by $f_c = V/(2\pi L I)$, where $V = 25\,\mathrm{V}$ is the input voltage, $I = 8\,\mathrm{A}$ the current and $L \approx 5 \times 10^{-2}\,\mathrm{H}$ the inductance of one coil, leading to a limit $f \approx 10\,\mathrm{Hz}$. The apparent mass of the granular column increases along the experiment and depends on the magnetic field frequency f. In particular, we observe small oscillations of the apparent mass signal, in phase with the oscillations of the magnetic field as presented before. The increase the apparent mass with time is close to an exponential growth for magnetic field frequencies $f = 0.1, 1\,\mathrm{Hz}$, saturating to a frequency-dependent mass $m^*(f)$. To verify this point, longer experiments for low frequencies are required. We must notice that the experimental data for $f = 0.01\,\mathrm{Hz}$ were carried on for longer time than the one displayed here where we focus only

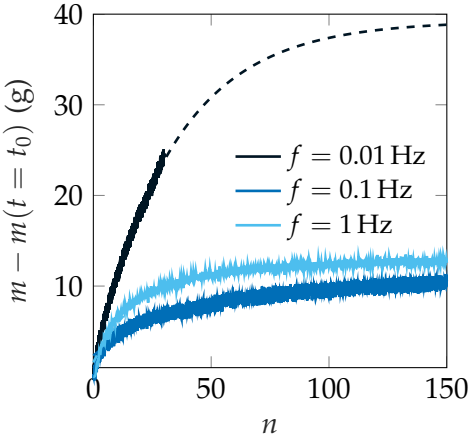

$m = a - be^{-n/n^*}$

f (Hz)	a	b	n^*
0.01	39.2	38.2	33
0.1	10.3	8.0	37
1	12.4	10.8	20

Figure 3.5: Magnetic fatigue of a granular packing for different frequency oscillations plotted against the number of magnetic oscillation cycles n. The experimental results are fitted by exponential laws (dashed lines). The fitting parameters for the different frequencies are given in the opposite table.

on the fast magnetic fatigue dynamics. One may wonder if the increase of the apparent mass is directly related to the number of magnetic field cycles n. In figure (3.5) we display the same experimental results in terms of magnetic cycles n. The apparent mass evolutions do not collapse on a single curve, and the apparent mass evolution with the number of cycles depends on the magnetic field frequency f. The experimental data points are fitted by the expression:

$$m = a - be^{-n/n^*(f)} , \tag{3.1}$$

with $n^*(f)$ a characteristic number of cycles. The results of the fit are given in figure (3.5). Regardless the frequency f, the two constants a and b are roughly the same but depend strongly on the frequency f. For the lowest frequency $f = 0.01$ Hz, the measurement was not carried-out for sufficient time, and is certainly more sensitive to the natural aging of the granular column. From these observations we propose the following empiric expression for the magnetic fatigue:

$$m = m^*(f)(1 - e^{-n/n^*(f)}) . \tag{3.2}$$

Magnetic response of the granular column for different magnetic field oscillations amplitudes

We varied the oscillating magnetic field amplitude A, characterized by the magnetic Bond number $\Psi = (\chi_m^2 A^2)/(\mu_0 a \rho g)$. In figure (3.6) we show the magnetic fatigue process for different amplitudes while the frequency of the magnetic field was kept constant $f = 1$ Hz. Without any magnetic field applied to the packing, $\Psi = 0$, we retrieve a slight increase in the apparent mass due to a natural aging of the packing. The experimental data curves are fitted by the empiric expression (3.2) and the results are given in figure (3.6). An increase in Ψ results in an increase of the apparent mass of the packing while the characteristic time n^* decreases. The empiric expression we found is the

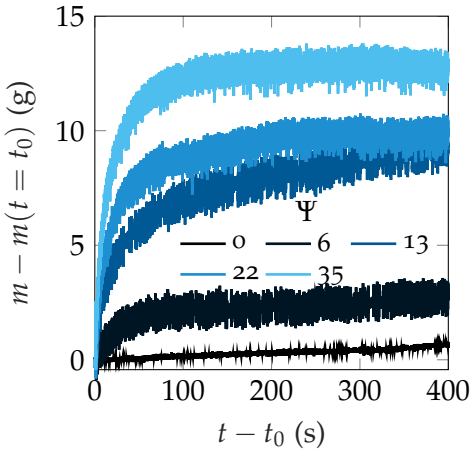

$m = m^*(1 - e^{-n/n^*})$

Ψ	m^*	n^*
6	2.4	38
13	8.5	46
22	9.5	24
35	12.6	20

Figure 3.6: Apparent mass of the granular packing evolution for different amplitude of the magnetic field.

result of preliminary magnetic fatigue experiments and can be summarized by the expression:

$$m = m^*(f, \Psi)(1 - e^{-n/n^*(f,\Psi)}) \, . \tag{3.3}$$

Future work is intended to validate our first observations, as well as simulations of a dynamic magnetic granular column.

3.2 DISCHARGE OF A MAGNETIC 2D-SILO

In this section, we revisit the classical experiment investigating the discharge of a 2D silo, filled with ferromagnetic grains and submitted to a constant magnetic field. This study started with the co-supervision of Maud Viallet's internship at the Physics Laboratory at ENS de Lyon (May-July 2020).

Experimental set-up

Our experimental set-up, presented in figure (3.7.a), is composed of a 0.6 mm gap Hele-Shaw cell filled with $2a = 0.5$ mm diameter steel beads. The gap is made out of two chambers separated by a $10a$ width opening with a 45 ° funnel. The beads are arranged in a one-layer packing and the system is placed inside a coil, wider than the cell, generating a magnetic field $\vec{B}$ normal to the cell plane. In this case, the maximum angle between the magnetic field and a separation vector $\vec{r}_{ij}$ between two particles i and j, shown in figure (3.7.b), is equal to $\alpha = \arccos(e/(2a) - 1) \approx 78$ °, meaning that the magnetic pair interactions are always repulsive. Finally, the two-dimension arrangement of the packing allows us to record the discharge of the silo with an high-speed camera (Phantom V10) at 440 frames per second. A typical obtained image is shown in figure (3.7.c). The cell starts with all the grains in the lower chamber and rotates to reach the next vertical state when the magnetic field is turned on. The discharge recording stops when the upper chamber is emptied and the magnetic field turned off.

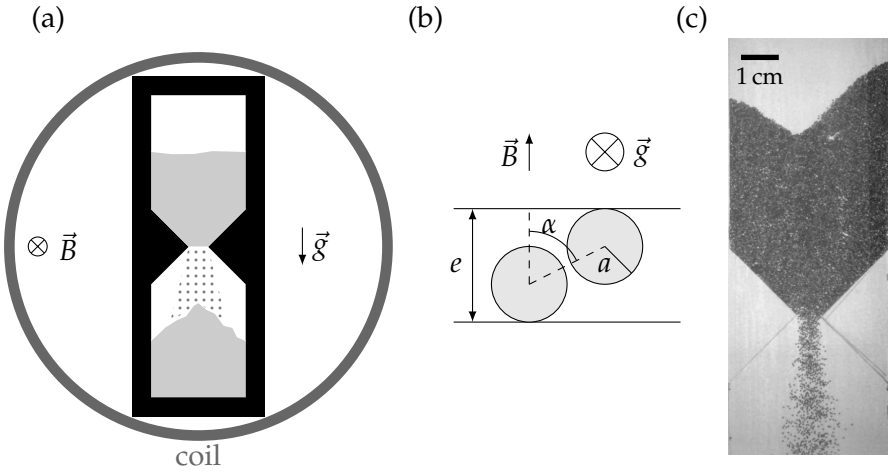

Figure 3.7: Discharge of a magnetic 2D-silo. (a) Experimental apparatus where a 2D hourglass is placed inside a coil generating an out of plane magnetic field. (b) Typical image of the discharge, without any magnetic field, $\Psi = 0$.

Experimental results

We first simply measure the outgoing grains flow rate. To do so, we estimated the temporal evolution of the number of particles in the lower chamber of the hourglass, via the packing area, during the discharge. The results are shown in figure (3.8.a) for different magnetic field strength. The number of particles increases linearly with time, signature of a constant discharge in the bottom chamber, from which we can estimate the flow rate shown in figure (3.8.b). The discharging flow rate is decreasing with the increase of the magnetic field amplitude following a linear tendency with $\Psi^{1/2}$. This result appears different from the measurement reported in [40], where the flow rate was linear with Ψ. Nevertheless, we must highlight the fact that this previous study was performed in a three-dimensional funnel suggesting a strong dependence on the geometry of the silo, usually taken into account in the phenomenological Beverloo law for non magnetic particles.

Upper chamber dynamics

The dynamics of the upper chamber is more complex. Indeed, as previously shown in section 1.1, grains are flowing in an avalanche cone, highlighted by our image analysis. During the discharge, we analysed the mean difference between two successive frames and binarized the mean difference over all frames, as shown in figure (3.9.b), where a typical cone opening angle θ emerges. The opening angle dependence on the magnetic field strength is shown in figure (3.9.c), getting narrower when increasing the magnetic field strength. This result reminds us of the work of [37] during the discharge of grains with electric interactions where stronger interactions resulted in a "rathole" behaviour with cohesive walls shown in the first chapter figure (1.15).

Furthermore, huge density fluctuations, visible for stronger magnetic field, take place in the upper chamber. An air bubble emerges at the opening neck

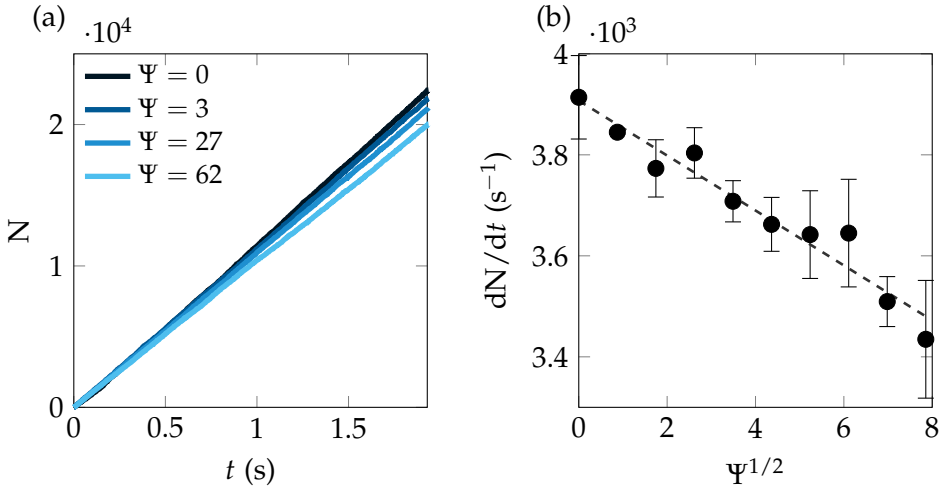

Figure 3.8: Flow rate of the discharging magnetic silo. (a) Temporal evolution of the number of particles in the lower chamber of the hourglass for different magnetic field strength Ψ. (b) Flow rate measured as the slope of the linearly increasing area of the bottom chamber.

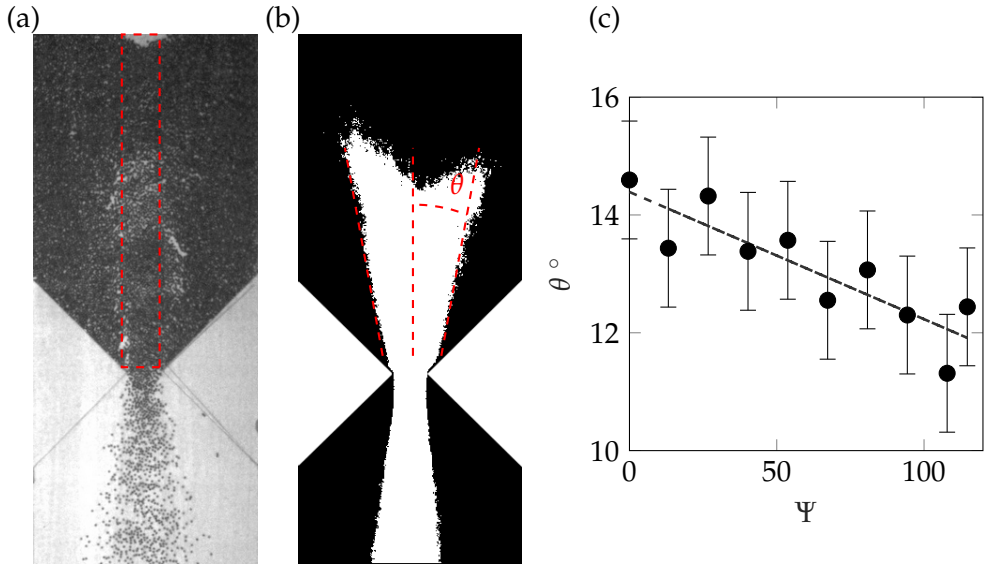

Figure 3.9: Discharge angle in the upper chamber. (a) Typical image of the magnetic silo discharge. (b) Binarized mean over all frames of successive frame difference, characterized by a cone flow of angle θ. (c) Evolution of the cone angle with the magnetic field strength.

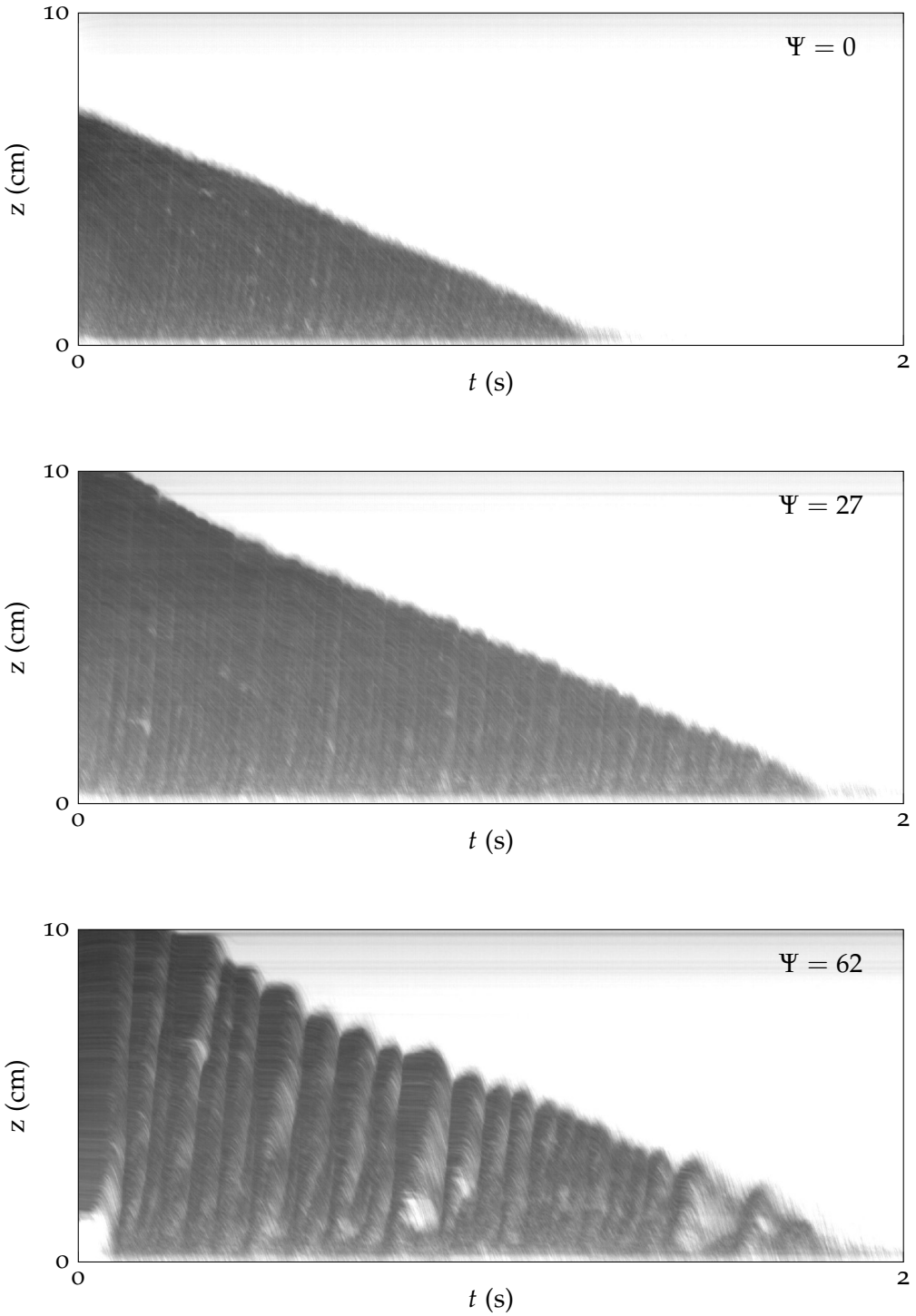

Figure 3.10: Spatio-temporal maps of the density of grains in the upper chamber for different magnetic field strength Ψ. The maps were obtained by averaging the pixel in the greyscale window above the opening at each time step. The white lines inside the granular packing correspond to the apparition of air bubbles propagating from the neck to the free surface of the packing.

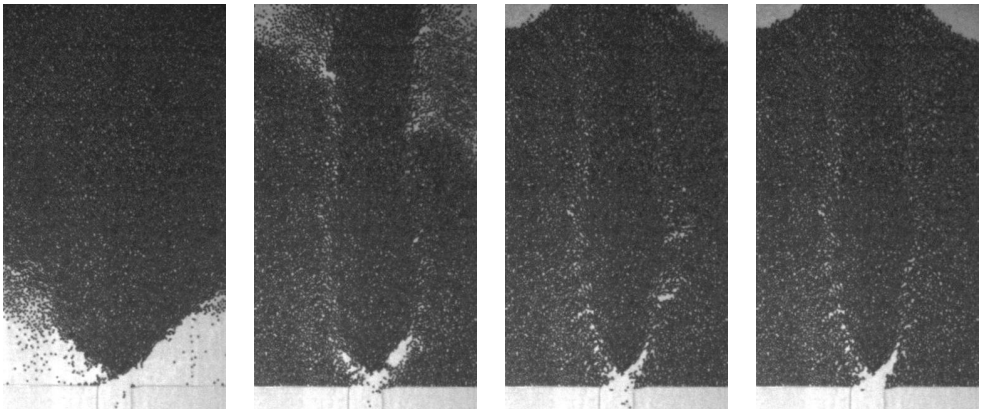

(a) $t = 0.4\,\mathrm{s}$ (b) $t = 0.6\,\mathrm{s}$ (c) $t = 0.8\,\mathrm{s}$ (d) $t = 1\,\mathrm{s}$

Figure 3.11: Discharge of the silo with a flat opening for the highest magnetic field amplitude $\Psi = 62$. The grains at the centre of the chamber do not move and the granular flow stops after one second.

moving upward to the free surface of the packing, which then collapses. At this point a new bubble emerges at the opening and the process repeats itself. This phenomenon reminds us of the work of [21, 66] describing a "tickling hourglass" where the flow stops until air percolates through the medium. Nevertheless, in our case we already mentioned that the flow rate of grains in the bottom chamber remains constant regardless the magnetic field amplitude applied. This striking behaviour is closer to [67, 68] where density fluctuations propagate through the granular medium. To quantify such density fluctuations we computed spatio-temporal maps of the density in the hourglass top chamber for different magnetic field strength. At each time step, we perform an average over the greyscale values of the pixels of a window within the upper chamber above the opening width as shown in figure (3.7.a). The results are shown in figure (3.10). Without any magnetic field, $\Psi = 0$, the grains in the upper chamber flow continuously. For an intermediate amplitude of applied magnetic field, $\Psi = 27$, we can notice the emergence of irregularities in the packing with the apparition of white lines, while the free surface of the packing continues to flow continuously. Finally, for a high magnetic field strength, $\Psi = 62$, the irregularities grow and the flow dynamics in the upper chamber becomes jerky with a characteristic stair-like dynamics of the free surface accounting for its successive collapses. Moreover, one can notice that the white lines inside the packing are all parallels, suggesting that the density fluctuations move at a constant speed regardless the packing height.

Flat silo experiment

We have also performed few experiments where we have modified the geometry of the silo: instead of a 45° funnel forcing the silo discharge, the bottom of the silo is now flat. Interestingly, we could observe a different dynamics of the discharge. In particular, as shown in figure (3.11), for the highest magnetic field amplitude $\Psi = 62$, the centre of the grains packing does not move while the

grains at the side avalanche. The whole packing clogs and the flow is stop only after one second. These preliminary observations will be addressed in future work.

4

UNSTABLE DRAINAGE OF FRICTIONAL FLUID IN A CAPILLARY TUBE

In this chapter, we describe the bulldozing instability during the slow drainage of a frictional fluid in a confined geometry. First, a frictional fluid composed of grains and liquid is formed inside a capillary tube. When the liquid is slowly drained out, the capillary forces at the liquid/air border bulldoze partly the particles along the tube. Under certain conditions a granular plug clogging the geometry is formed and leaves a plug trail along in its path. Second, the liquid properties are varied to investigate the onset of the bulldozing, with the apparition of a novel capillary washboarding instability. Finally, we give preliminary results on the control of the bulldozing instability introducing ferromagnetic pair-interactions inside the granular packing.

4.1 PLUGS FORMATION

Filling procedure

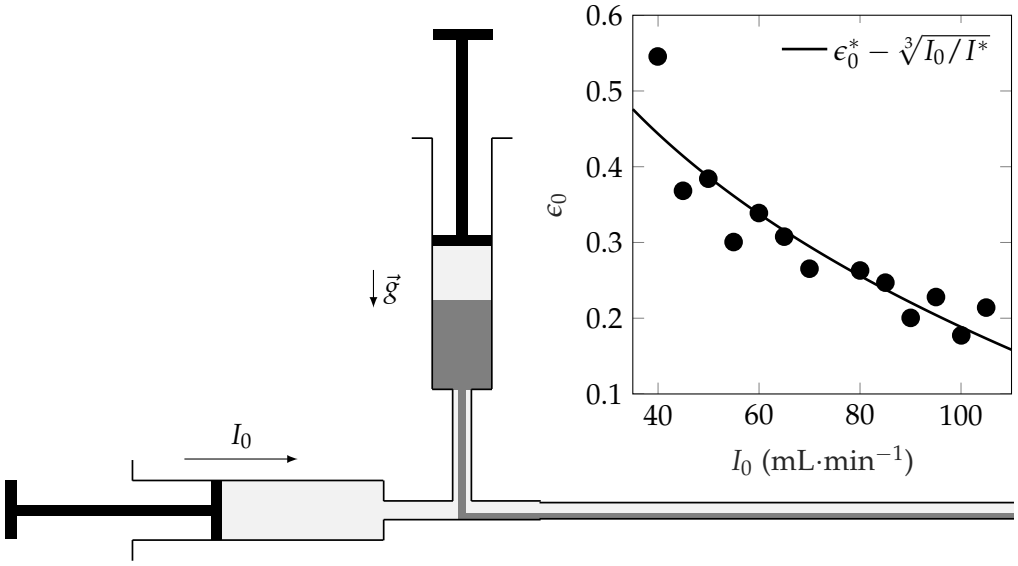

Figure 4.1: Experimental set-up and filling procedure of a capillary tube with a mixture of glass beads and water in order to prepare an uniform layer of beads sedimented in the capillary. Two syringes one filled with the particles and the other with the liquid inject the frictional fluid inside the capillary at a constant injection rate I_0. The inset gives the achieved amount of particles inside the tube ϵ_0 for the different injection rates.

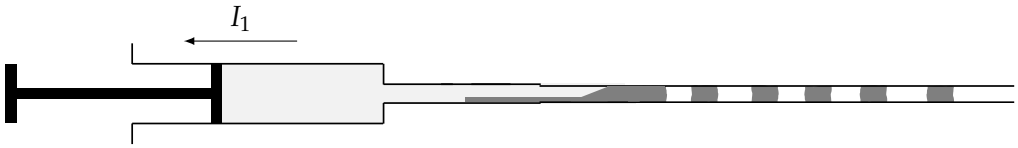

Figure 4.2: Drainage of the frictional fluid out of the capillary tube. The syringe is withdrawing liquid at a constant flow rate while the other side of the tube is opened to air. During the drainage, the particles are bulldozed and may clog the geometry and forms a plug trails along the tube.

Frictional fluids are, as we defined earlier, composed of a granular material and a surrounding liquid. Typically, we use glass beads of density $\rho = 2 \times 10^3\,\mathrm{kg \cdot m^{-3}}$ while the typical liquid used in previous studies is water [52, 57, 58]. In our study we will demonstrate that the liquid properties are essential for the onset of the bulldozing mechanism. In all experiments, the set-up remains the same and is presented in figure (4.1). The capillary tube is of diameter $D = 2\,\mathrm{mm}$, length $L_{\mathrm{tube}} = 1\,\mathrm{m}$, opened to air on one end and connected to the filling syringes on the other side. The tube was made hydrophobic in advance using a silanization solution ($\sim$5% dimethyldichlorosilane in heptane). One of the syringe, vertical, is filled with the grains and the liquid, the grains are sedimenting by gravity at the opening of the capillary, while the other syringe, horizontal, is filled only with the liquid. The liquid is injected in the system at a constant flow rate I_0, pushing the particles inside the capillary and creating a uniform layer of beads at its bottom. Depending on the flow rate, one can tune the amount of particles initially in the tube ϵ_0, as presented in the inset of figure (4.1). The model fitting our experimental results is presented in appendix . We can estimate that the initial height of particles inside the tube $2\epsilon_0 R$ is given by:

$$\epsilon_0 = \epsilon_0^* - \sqrt[3]{\frac{I_0}{I^*}}\,, \tag{4.1}$$

with ϵ_0^* and I^* characteristic amount of grains and filling rate, respectively.

BULLDOZING EXPERIMENTAL SET-UP

Once the tube is partially filled, the flow of particles from the top syringe is stopped, and the flow of liquid is reversed as shown in figure (4.2). The withdrawing flow rate is constant $I_1 = 0.1\,\mathrm{ml \cdot min^{-1}}$, and low enough to ensure no viscous effect as described in section 1.3. During the drainage, the bulldozing front of particles may clog the geometry. Then, due to Janssen friction forces between the grains and the capillary, the pressure needed to push the grains increases exponentially with the length of the front. Once the pressure needed to push the grains overcomes the capillary pressure threshold at the liquid/air border, air percolates through the packing. The capillary pressure threshold depends on the size and shape of the pores as well as on the wettability of the medium. The air percolation results in the formation of a plugs trail along the capillary as shown in figure (4.2).

Index-matching experiment

We already discussed in section 1.3 the formation of plug patterns along the tube resulting from the bulldozing instability. We propose here to highlight the air percolation through the granular packing by using an index-matching liquid. Our choice for both liquid and particles was influenced by [69]. We used ammonium thiocyanate NH_4SCn-water solution and borosilicate glass which densities match the ones of water and glass. Moreover, the refractive index of NH_4SCn-water solution can be tuned by varying the mass concentration of the solution ($NH_4SCn\ \%_w$) and temperature to match the one of borosilicate as shown in figure (4.3). A linear fit of the data obtained by [69] gives a weight concentration $NH_4SCn\%_w \approx 68\%$ to match the refractive index $n = 1.517$ of the borosilicate particles. A fine tune of the liquid temperature would lead to a better adjustment of the liquid refractive index. Nevertheless, the already good match of both indexes allows us to clearly see the air percolation through the grains.

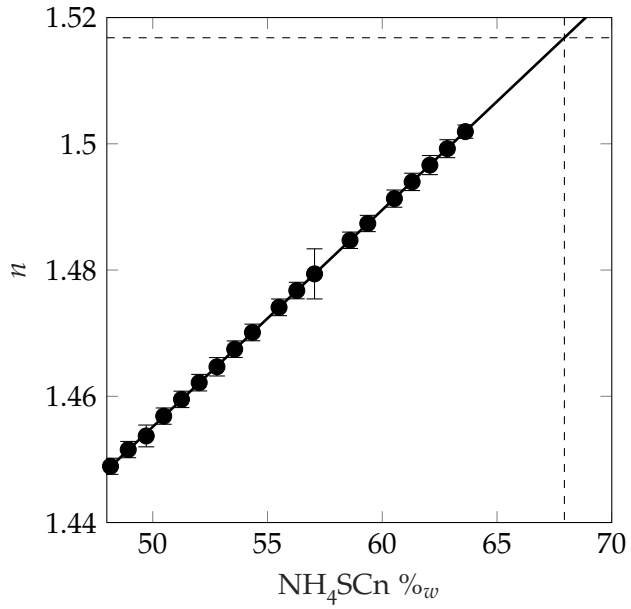

Figure 4.3: Refractive index of NH_4SCn - water mixture for different mass concentrations, data from [69]. The dashed lines correspond to the refractive index of borosilicate glass.

The experimental realizations were made with the previously discussed experimental set-up where the liquid is a NH_4SCn-H_2O mixture and both the glass beads and the capillary are made of borosilicate glass. We recorded the plug formation along the tube and focused on the percolation event when the pressure needed to push the bulldozing front overcomes the capillary pressure threshold at the meniscus boundary. A typical example of the percolation event is shown in figure (4.4). In this case, the particles blend visually in the surrounding liquid while a mixture of air and particles appears in black. We can see that air starts to percolate at the top of the packing before invading the

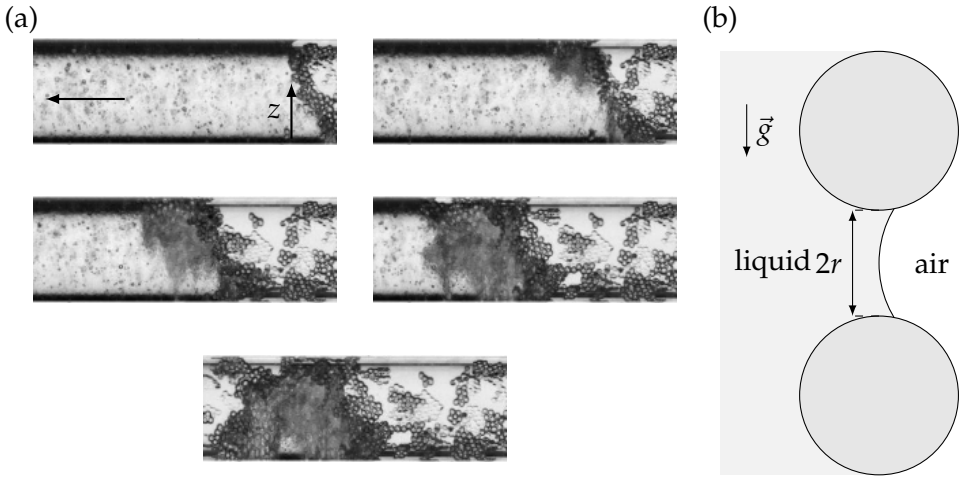

Figure 4.4: Percolation of air inside the granular packing. (a) Experiments with a liquid matching the refractive index of the particles. A mixture of air and particles appears in black. (b) Geometry of air percolation at the particle scale.

rest of the granular medium. This result can be understood by the hydrostatic pressure gradient occurring along the vertical direction. The capillary pressure at position z (upward direction), is given by:

$$\delta p_c(z) = \delta p_c(z = D) - \rho_l g(D - z) \, , \tag{4.2}$$

with ρ_l the liquid density and $z \in [0, D]$ the vertical position inside the tube. If we consider the granular packing to be roughly homogeneous in size a and packing fraction ϕ_c, the capillary pressure threshold is constant at the meniscus. Assuming no boundary effect, the capillary pressure is maximum at the top of the tube and air starts to invade the medium there. Air percolates through the grains until reaching the bottom of the tube. The meniscus continues then its course along the tube by bulldozing new particles and leaving behind a plug of grains, air and trapped liquid. We must note that the wetting properties of the liquid are not controlled and the drainage of the frictional fluid is not as clean as when using water. Such issue is evidenced by the observation of small particles clusters left along the tube.

4.2 ONSET OF THE BULLDOZING

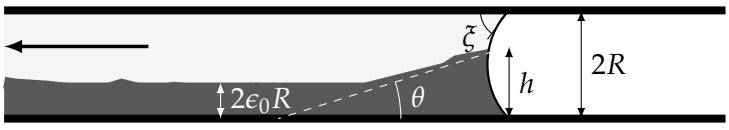

Figure 4.5: Bulldozing onset. The liquid is slowly withdrawn out of the tube at a constant flow rate. The meniscus at the air-liquid boundary can bulldoze the particles resting in the sedimented layer of height $2\epsilon_0 R$, forming a particles front of height h.

We have described the mechanics of the bulldozing instability taking place when particles immersed in a liquid are clogging a capillary tube. Nevertheless, the conditions for which this instability takes place have not been studied in detail, and thus are not clearly understood. This is actually the subject that we propose to explore now, by notably changing systematically some properties of the liquid, and specifically, its surface tension and contact angle with silanized glass walls. We explore in this section the conditions for which the system transit from a sedimented layer of beads at the bottom of the tube to the bulldozing of the particles by the meniscus up to the clogging situation.

Varying the liquid properties

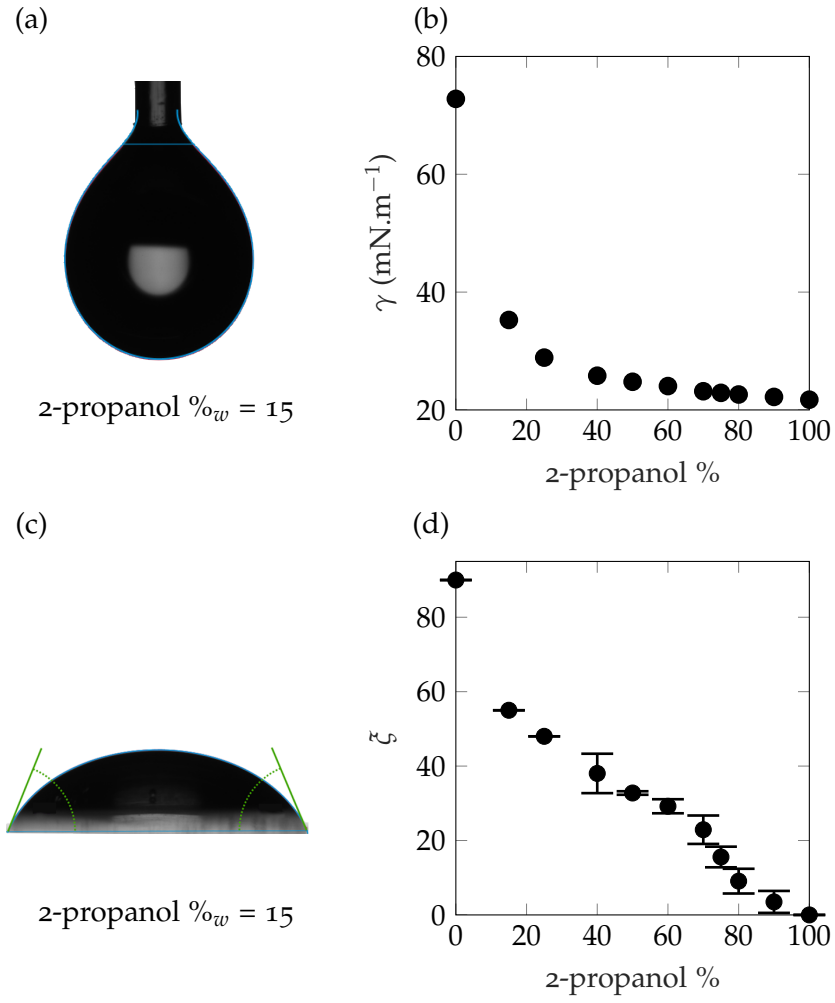

Figure 4.6: Water-isopropanol liquid properties. (a) Drop shape experiment. (b) Surface tension of the liquid measured via the drop-shape analysis for different mass concentration of isopropanol. (c) Wetting angle measurement. (d) Wetting angle ξ for different mass concentration of isopropanol.

In previous studies [52, 57, 58], when using water as the surrounding liquid, the bulldozing instability was always occurring regardless the amount of particles initially in the tube. Water has a quite large surface tension against

air, $\gamma = 71.97\,\mathrm{mN}\cdot\mathrm{m}^{-1}$. We propose here to vary the liquid properties, by mainly lowering its surface tension, to investigate if in these new conditions the meniscus is able to push the particles all the way to the clogging situation where $h = 2R$ to initiate the bulldozing instability.
To lower the surface tension of the liquid without changing too much its density, we use an isopropanol-water mixture where we varied the weight percentage concentration of isopropanol, noted 2-propanol $\%_w$. For each prepared concentration we measured both the surface tension γ and the wetting angle ξ of the liquid with a silanized glass plate, to match the experimental conditions, using a drop shape analyser (Kruss DSA24E). The images as well as the measurements are shown in figure (4.6). The surface tension of the liquid drops rapidly while adding isopropanol to water, and our measurements are in excellent accordance with [70]. The drawback of using such liquid while keeping constant the tube surface conditions is that the wetting properties are also changing drastically. Indeed, the wetting angle of the solution with a silanized glass plate also drops from $\xi = 90\,^\circ$ for pure water, the glass plate is hydrophobic, to $\xi = 0\,^\circ$ for pure alcohol, the liquid is wetting the surface. To quantify the ability of the meniscus to bulldoze an assembly of grains, we consider the geometry of figure (4.5) for $h = 2R$. The bulldozing front is similar to a triangular frictional pad exerting a friction force:

$$f_{\text{friction}} = 2\mu g \frac{\pi R^3}{\tan\theta}\Delta\rho \ . \tag{4.3}$$

The force exerted by the meniscus on the friction pad can be approximated by:

$$f_{\text{meniscus}} = 4\gamma R \sin\xi \ . \tag{4.4}$$

Comparing both forces, we introduce the dimensionless number $\mathcal{C}$:

$$\mathcal{C} = \frac{2\gamma \tan\theta \sin\xi}{\mu g \Delta\rho \pi R^2} \ . \tag{4.5}$$

This dimensionless number ranges from $\mathcal{C} = 2.7$ for pure water and $\mathcal{C} = 0.028$ for pure isopropanol. The bulldozing mechanism, always occurring for pure water, is then challenged by adding isopropanol to the solution.

Experimental results

Experimentally, we varied both the amount of isopropanol in the liquid and the amount of particles initially in the tube of height $2\epsilon_0 R$.
Figure (4.7) shows some typical experimental observations for different isopropanol concentrations while keeping $\epsilon_0 = 0.2$ constant. We can observe three different behaviours. For low concentration in isopropanol, *i.e* high surface tension, the meniscus is able to bulldoze the particles up the way to the clogging situation. For medium concentration, 2-propanol $\%_w = 50$, the meniscus is bulldozing partially the particles but deforms itself until sliding over the particles leaving behind a dune that does not fill the tube. For pure alcohol, the meniscus does not bulldoze any particle and only slides over the bottom layer of particles. Nevertheless, by increasing the amount of particles initially in

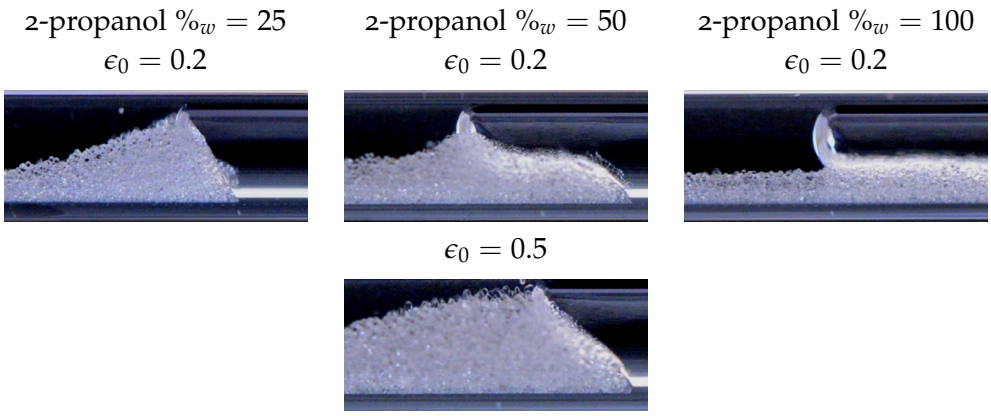

Figure 4.7: Drainage experiment for different isopropanol concentration 2-propanol $\%_w$ and a fixed initial amount of particles $\epsilon_0 = 0.2$. For the case of dune formation at 2-propanol $\%_w = 50$, the clogging regime is reached by increasing the initial amount of particles $\epsilon_0 = 0.2 \rightarrow 0.5$.

the tube for the same isopropanol concentration, one can trigger the clogging situation as shown in figure (4.7).

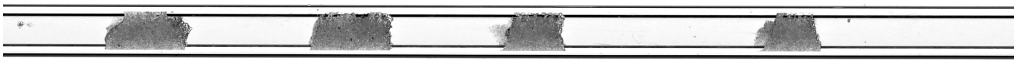

(a) Plugs. 2-propanol $\%_w = 0$ and $\epsilon_0 = 0.2$.

(b) Dunes. 2-propanol $\%_w = 25$ and $\epsilon_0 = 0.1$.

(c) Stable layer. 2-propanol $\%_w = 100$ and $\epsilon_0 = 0.5$.

Figure 4.8: Different types of formation along the tube depending on the liquid properties and initial amount of particles.

The final patterns formed along the tube for the three different regimes are summarized in figure (4.8). The particles clogging the capillary tube leads, as described earlier, in the formation of a plugs trail along the tube. When the meniscus bulldoze partly the particles, dunes are formed periodically along the tube. At the extreme, when no particle is bulldozed at all, the meniscus slides over the sedimented layer along the tube.

All experimental results are summarized in a phase diagram given in figure (4.9). We can distinguish a transition at 2-propanol $\%_w = 75$ where the initial amount of particles needed to trigger the clogging situation increases drastically, which seems related to the drop in wetting angle. For lower concentration a transition from dunes to plugs formation occurs by increasing the initial amount of particles ϵ_0.

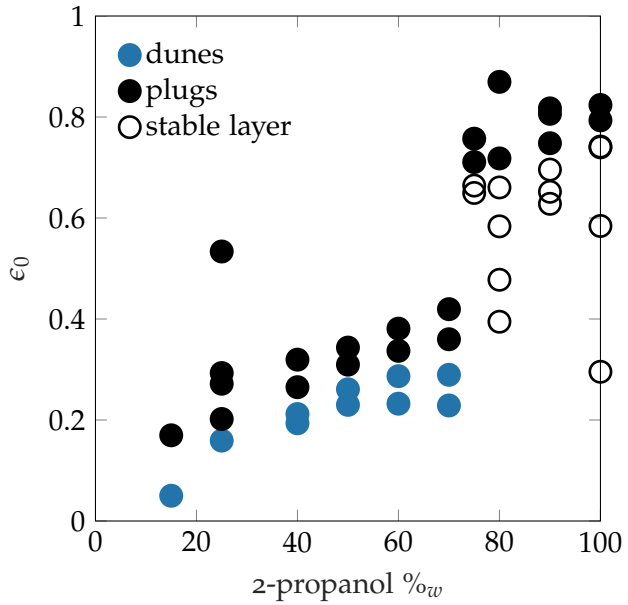

Figure 4.9: Phase diagram of the different patterns and process observed during the drainage experiment. We varied both the isopropanol concentration and initial filling fraction of the tube. In black, situations where the meniscus is able to bulldoze the particles all the way to the clogging situation, initiating the plug formation. In white, the meniscus does not bulldoze any particle and slide over the sedimented layer. In blue, by a capillary washboarding process, the meniscus is forming periodic dunes along the tube.

High amount of isopropanol

For large alcohol concentrations, the meniscus is not able to bulldoze any particles. The transition is not understood at the moment. However, the surface tension for 2-propanol $\%_w \geq 75$ is almost constant while the wetting contact angle decreases drastically. Future work is intended to explain the no-bulldozing situation.

4.3 CAPILLARY WASHBOARDING

For lower alcohol concentrations (2-propanol $\%_w \leq 70$), we see the formation of dunes along the tube. This mechanism reminds us of the washboarding instability where periodic dunes form at the top of a sand road from the repeated passage of vehicles. Figure (4.10.a) gives a typical illustration of this phenomenon. In the lab, similar results are obtained using a plow pushing particles on top of a sand layer at constant velocity [72, 73] as shown in figure (4.10.b). In our case of a meniscus bulldozing particles, the process looks very similar. However, as opposed to an advancing plow, the meniscus is deformable. Moreover, in the bulldozing experiment the meniscus is forming a dune after only one passage as opposed to road washboarding appearing after a series of plow passing.
In this section we investigate numerically the formation of dunes, which we have decided to call by analogy "capillary washboarding". The complete sketch of the

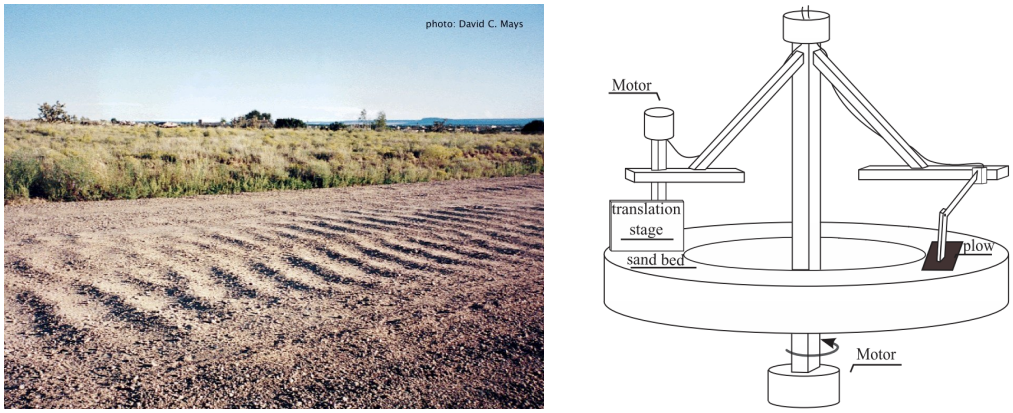

(a) (b)

Figure 4.10: Washboard instability. (a) Picture from [71]. Sand road washboarding from the multiple passage of vehicles. (b) Sketch from [72]. Experimental set-up for characterizing the washboarding instability. A plow is pushing grains on top of a resting bed at constant velocity for different plow attack angles.

situation we are interested in is given in figure (4.11). Two main components have to be simulated, the meniscus governed by capillary action, and the granular pressure pushing on the meniscus.

Meniscus simulation

We describe firstly the meniscus in the absence of grains in the geometry. For the capillary action, we propose to use the simulation proposed by [54], and shown in figure (4.12). This kind of simulation was first proposed in 2D to simulate the labyrinthine pattern obtained after the slow drainage of a frictional fluid in a Hele-Shaw cell. In our case, we are adapting this simulation in the vertical direction. The meniscus is simulated as a series of N points in the 2D-space (x, z), initially vertical at $x = 0$. At each time step, the angle between two successive points 2β is computed from their positions, as well as the separation length $l_{i,i+1}$. The local curvature at each point is given by [54], and writes:

$$\kappa_i = \frac{\pi - 2\beta_i}{l_{i-1,i} + l_{i,i+1}}\,, \tag{4.6}$$

giving the local capillary pressure following the Young-Laplace equation:

$$\Delta P = \gamma\kappa. \tag{4.7}$$

The meniscus then moves where the local pressure is minimum, and the corresponding point is moved along the local normal vector over a distance δl as shown in figure (4.12.b). At this point the new $\beta_i(t+1)$ and $l_i(t+1)$ are computed and the process repeats itself. At each time step, we also add a point every time the distance between two successive points is greater than a threshold $l_{i,i+1} > l_c$, respecting the local curvature along the meniscus. Finally, we impose

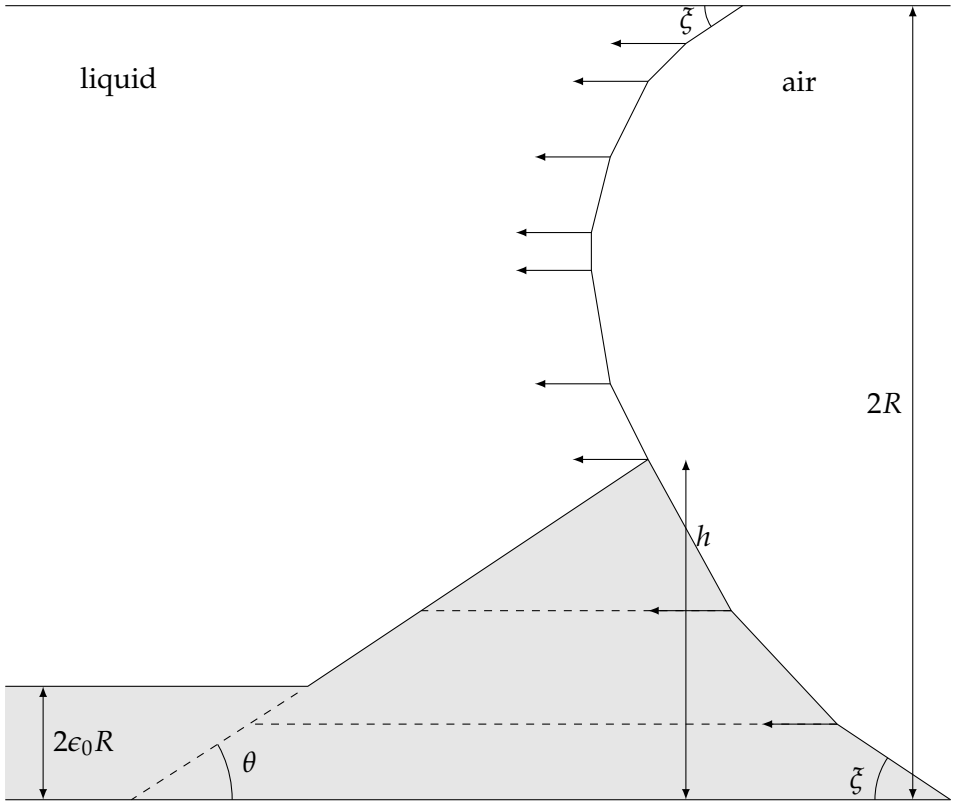

Figure 4.11: Global sketch of our simulations. The meniscus is simulated by an assembly of N points moving normally to the meniscus in contact with liquid, and in the horizontal direction when in contact with particles. At each time step we record the packing height h while the wetting conditions ξ and the avalanche angle θ are kept constant.

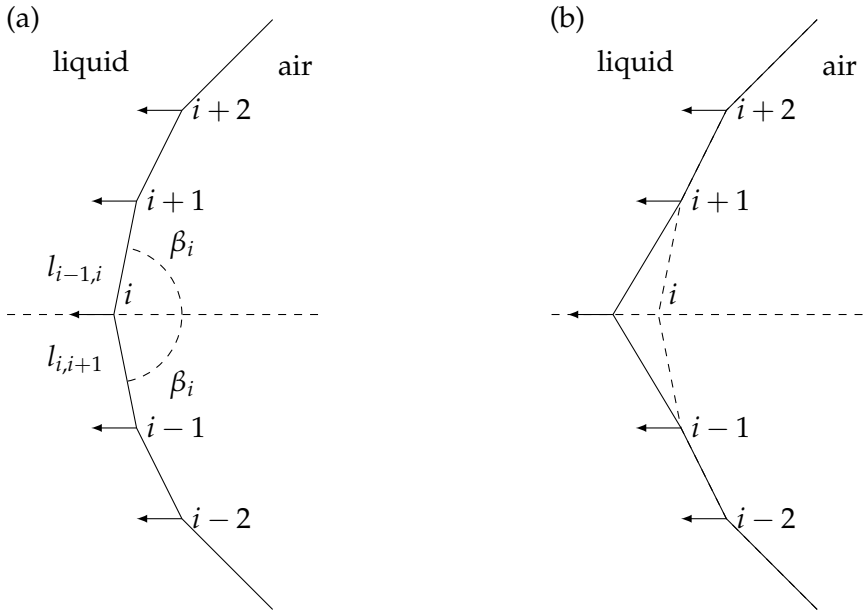

Figure 4.12: Meniscus simulation. (a) The meniscus is simulated as a point assembly where the local curvature is computed using the local angle β_i and points distances $l_{i,i+1}$. (b) At each time step the point of lower local pressure advances normal to the meniscus over a distance δl.

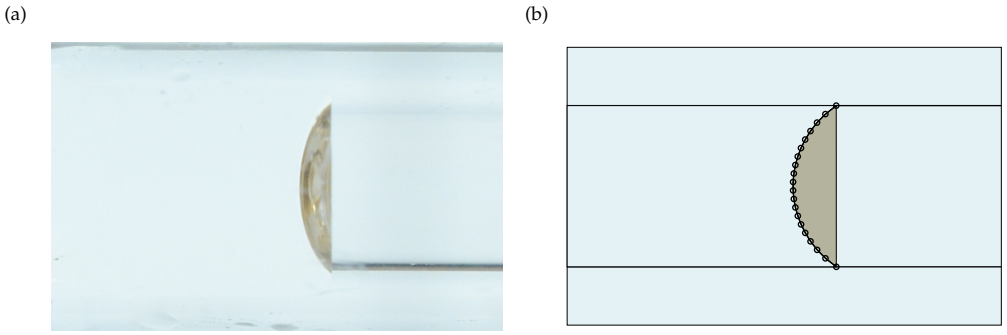

Figure 4.13: Comparison between an experimental meniscus (a) and simulated one (b).

the boundary conditions $\beta_1 = \beta_N = (\pi - \xi)/2$. A meniscus simulation, without particles, is presented in figure (4.13), similar to a typical experimental picture.

Granular stress on the meniscus

To add particles to the simulated system, we have to consider the granular stress exerted by each layer of grains on its corresponding meniscus plane. In figure (4.14), we consider the layer i that we can divide in several zones, each adding a force on the meniscus:

- the bulldozed part, in contact with the sedimented layer applying a force $f_{\text{bull}} = \mu \cos^2 \theta g M^i_{\text{bull}}$,
- the mass of the layer itself applying a friction force $f_{M^i} = \mu g M^i$,

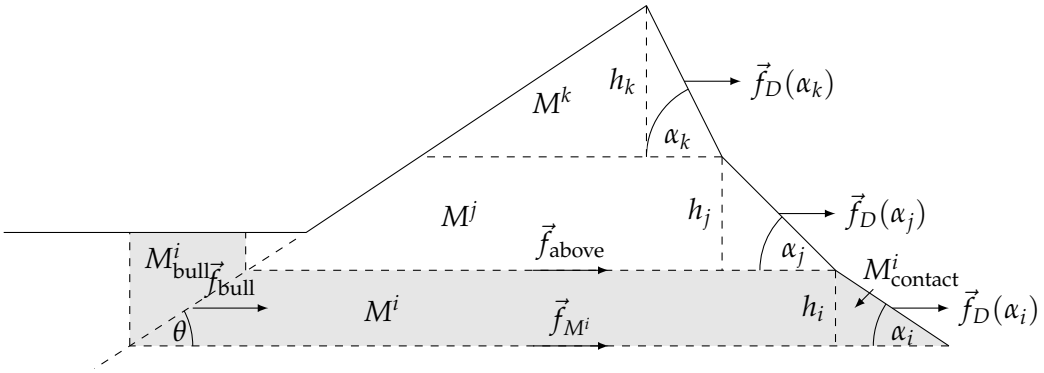

Figure 4.14: Granular packing in the simulations. The pile is divided in several horizontal layers of mass M_i in front of the meniscus planes. Each layer is bulldozing a particle front of mass M^i_{bull} and a tilted mass M^i_{contact} is in contact with the meniscus.

- the mass above the layer applying a friction force $f_{\text{above}} = \mu g \sum_{k>i} M^k$,
- the mass in contact with the meniscus applying a friction force $f_D(\alpha_i) = \mu_D(\alpha_i) g M^i_{\text{contact}}$,

The latter being pushed by a tilted meniscus plane, the friction coefficient will depend on the local angle of attack α_i as suggested by [74] to model the washboard instability [72, 73]. In figure (4.15.a), we represent the washboarding situation where a triangular pile of grains is pushed by an inclined plane over a granular bed. The pile is characterized by the angle of avalanche θ, the angle of attack α and its mass M. The granular pile is exerting a drag force $\vec{F}_D$ and a lift force $\vec{F}_L$ on the pushing plane, given by the associated friction coefficient μ_D and μ_L:

$$F_D = \mu_D(\alpha) M g \ , \ F_L = \mu_L(\alpha) M g \ . \tag{4.8}$$

Both friction coefficients depend on the angle of attack α, and experimental data from [74] are shown in figure (4.15.b). At the moment, the direct dependence of the friction coefficient on the angle of attack is not fully understood. We propose to fit the experimental data by a power law $\mu_{D,L} = a_{D,L} \alpha^{b_{D,L}}$, as shown in figure (4.15.b). In our simulation, we use this power law fit to model the local friction coefficient $\mu_D(\alpha_i)$ along the meniscus. We can note that both friction coefficients can be linked together in an effective friction coefficient $\mu_{\text{eff}} \in [0, 1]$:

$$F_D = \mu_{\text{eff}}(F_L + Mg) \ , \ \mu_{\text{eff}} = \frac{\mu_D(\alpha)}{1 + \mu_L(\alpha)} \ . \tag{4.9}$$

Finally, the force applied on the meniscus at point i is then given by the addition of all the individual friction forces exerted by the moving plow i that we can summarize by:

$$\sigma_i \delta S_i = f_{\text{bull}} + f_{M^i} + f_{\text{above}} + f_D(\alpha_i) \ , \tag{4.10}$$

where δS_i is the local surface of the meniscus plane and σ_i the granular stress applied locally on the meniscus.

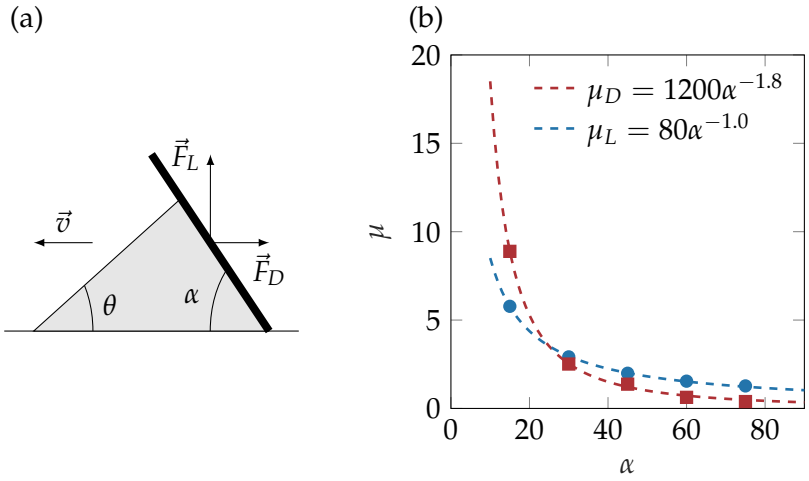

Figure 4.15: Friction pad sliding over a granular bed. (a) Geometry of the pad pushed by plane advancing at a constant velocity $\vec{v}$ with an angle of attack α. (b) Data from [74]. Friction coefficients of the drag $\vec{F}_D$ and lift $\vec{F}_L$ forces.

The global picture of our simulation is given in figure (4.11). To close the simulation, at each time step, the meniscus advances where the local pressure $\delta P_i = \gamma\kappa_i + \sigma^i + \rho_l g(2R - z)$ is minimum. At this point, the meniscus is advancing over a distance δ_l such that the withdrawn volume δV is constant, respecting the experimental condition of a constant withdrawal rate. We finally ensure mass conservation by adjusting the packing height h accordingly at each time step.
During the simulation, the wetting angle ξ and avalanche angle θ are kept constant.

Descent phase

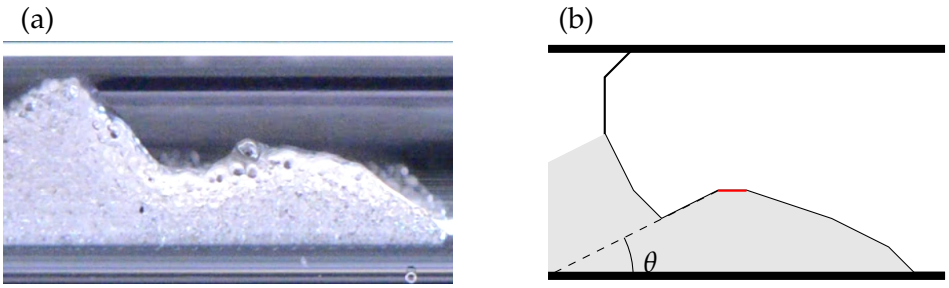

Figure 4.16: Descent phase of the meniscus. (a) Experiment where the meniscus deformed itself until becoming horizontal, the meniscus then plunge in the bead layer. (b) Simulation of the descent phase: when the meniscus becomes has an angle of attack lower than 4° (in red), we force a plunge with an angle θ.

While the meniscus is advancing inside the capillary, it may deform itself until becoming flat with an angle of attack $\alpha_i = 0$. At this point i, we remark in the experiments that the meniscus plunges in the sedimented layer while

forming an angle θ, equals to the avalanche angle, with the horizontal. The origin of this behaviour is still under investigation, but we believe that the granular nature of the medium may explain it. Since the granular packing is considered continuous in our simulations, we forced this descent plunge of the meniscus each time the local attack angle α is lower than a given threshold of $\alpha_{\min} = 4°$.

Simulation results

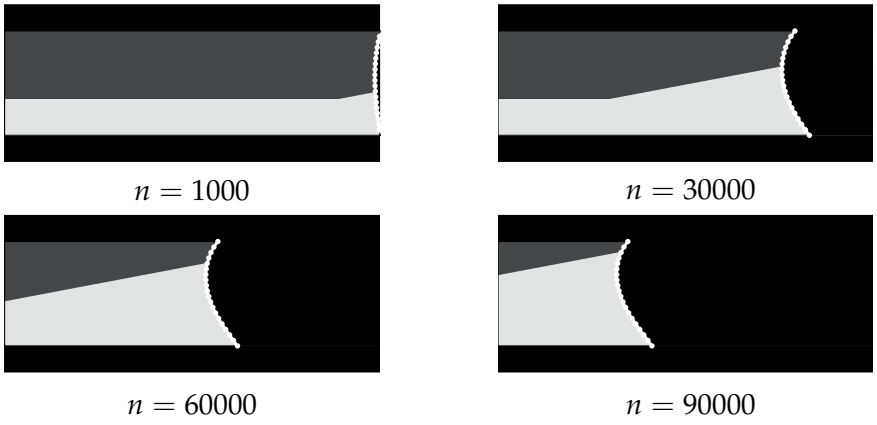

Figure 4.17: Typical example of the capillary washboarding simulation at different time steps n. 15% of isopropanol and initial amount of particles $\epsilon_0 = 0.3$.

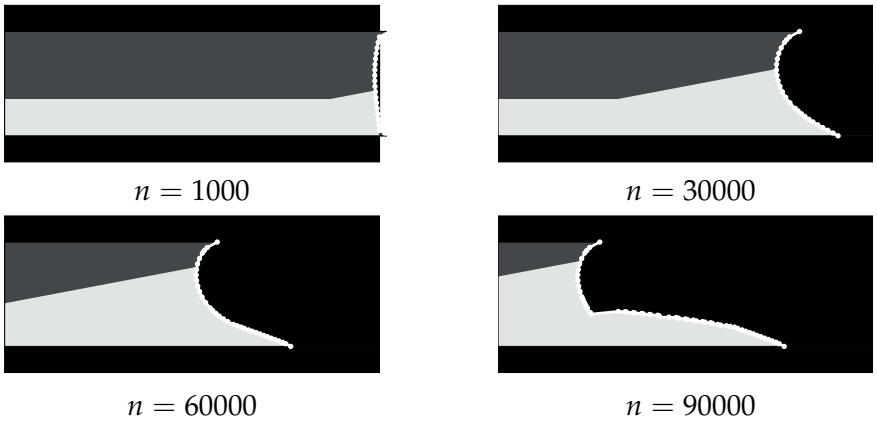

Figure 4.18: Typical example of the capillary washboarding simulation at different time steps n. 60% of isopropanol and initial amount of particles $\epsilon_0 = 0.3$.

In the simulation, we can tune both the wetting angle ξ, the liquid-air surface tension γ and the initial amount of particles ϵ_0. Figure (4.17) gives the simulated meniscus at different time steps n for $\epsilon_0 = 0.3$ and liquid properties matching a 15% isopropanol solution. The meniscus, initially vertical on the right side,

firstly deforms itself according to the capillary pressure. In this case, both the wetting angle ξ and surface tension γ are high, and the meniscus is able to bulldoze the particles up to the top of the capillary. Figure (4.18) gives the simulated meniscus at different time steps n for $\epsilon_0 = 0.3$ and liquid properties matching a 60% isopropanol solution. In this case, the meniscus deforms itself as the particles height increases and so does the granular stress. The meniscus is weaker and tends to stretch horizontally until not being able to bulldoze the particles anymore entering the descent phase described earlier, leaving behind a typical dune.

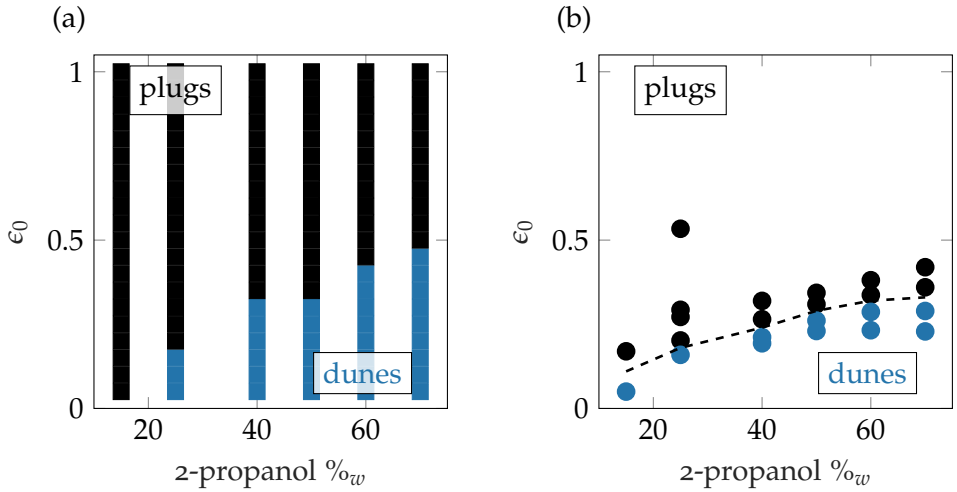

Figure 4.19: (a) Simulation phase diagram of the different bulldozing mechanisms depending on the solution concentration in alcohol and initial height of particles. (b) Experimental phase diagram following the same tendency on the different parameters.

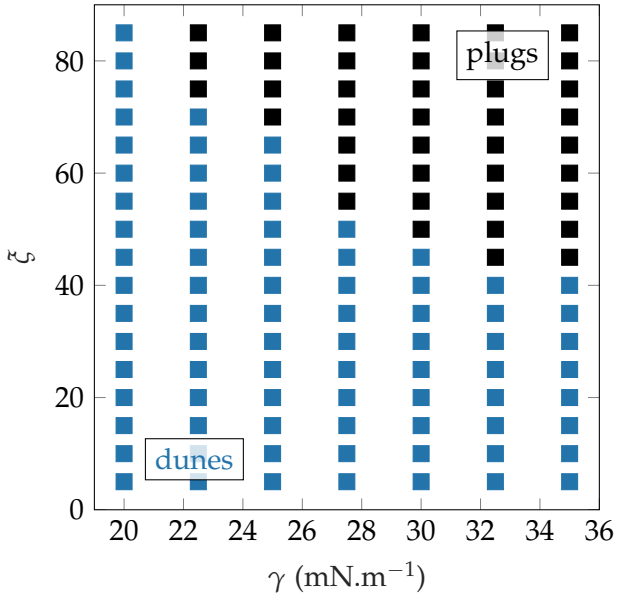

Figure 4.20: Simulation phase diagram varying the liquid properties γ, ξ while keeping the initial amount of particles constant $\epsilon_0 = 0.3$.

As in the experiments, we propose to summarize the simulation results in a phase diagram given in figure (4.19.a). These results have to be compared to the experimental results shown in figure (4.19.b). We note two different regions corresponding to either the formation of plugs (the particles height h reaches the tube diameter) or the capillary washboarding situation where the final result consists of a series of periodic dunes along the capillary. The simulations phase diagram matches nicely the experimental data regardless the simplified 2D geometry considered in the simulations. We also retrieve the same conditions where the plugs formation appears if the amount of water or the initial amount of particles ϵ_0 are high enough.
Unlike the experiments, the meniscus simulations allow us to vary independently the surface tension γ and wetting angle ξ. We summarize the results in a phase diagram in figure (4.20) where the initial amount of particles is fixed at $\epsilon_0 = 0.3$. As predicted, for high enough surface tension or wetting angle, the system transits to the formation of plugs. We note that both liquid parameters (surface tension, wetting angle) are relevant for the bulldozing mechanism.

Figure 4.21: Simulated results along the capillary for 60% isopropanol solution and initial amount of particles $\epsilon_0 = 0.3$.

Finally, we give in figure (4.21) the final pattern obtained for a 60% isopropanol solution and initial amount of particles $\epsilon_0 = 0.3$. The particles layer is deformed into a series of periodic dunes similar to the washboard road experiments. Future experimental work is planned to obtain the characteristic properties of the formed patterns (amplitude, wavelength).

4.4 FERROMAGNETIC TRIGGERING

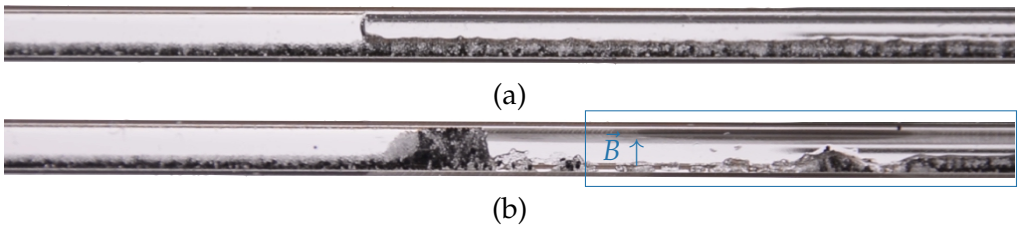

Figure 4.22: Ferromagnetic triggering of the bulldozing mechanism $\epsilon_0 = 0.2$, $\phi_m = 0.5$. (a) No magnetic field applied, no bulldozing mechanism and the bed layer is at rest. (b) A vertical magnetic field is applied on the right side of the tube (blue zone). The bulldozing mechanism is triggered and carries on after the magnetic field is turned-off.

Finally, in an upcoming study, we propose to modify the plug pattern along the capillary by modifying its key mechanism, the Janssen effect, which tunability has been demonstrated earlier by the introduction of ferromagnetic pair interactions between the grains. However, one final step towards the magnetic bulldozing experiment needs to be addressed. Ferromagnetic grains are usually made of steel, a far heavier material than the glass beads used so far, questioning the onset the bulldozing instability. Indeed, for such heavy beads, the meniscus is not able to bulldoze the particles and will slide over the particles bed resting at the bottom of the capillary. We have demonstrated that increasing the liquid surface tension would trigger the instability, however we propose here another solution based on the magnetic properties of the material.
We propose here to initially fill the tube with both steel and glass beads via two distinct syringes, using the same filling protocol as shown in figure (4.1). The steel beads are injected first inside the tube at a constant flow rate I_{steel}, followed by glass beads at another flow rate $I_{\text{glass}} \ll I_{\text{ferro}}$, allowing a fine tune of both the initial filling fraction ϵ_0 and the ferromagnetic concentration ϕ_m. Withdrawing the liquid out of the tube as done before does not result in the onset of the bulldozing as expected and shown in figure (4.22.a). However, if we apply a vertical magnetic field at the right-hand side of the capillary, the process is triggered and the meniscus bulldozes part of the sedimented particles. The most important result here, is that even after turning off the magnetic field, as shown in figure (4.22.b), the bulldozing process carries on and the plug formation occurs along the tube. To apprehend this fact, we must remember that as soon as the particles layer reaches the top of the tube, $h = 2R$, the system enters a competition between the granular stress needed to push the plug forward and the minimum pore pressure for air to percolate the medium. The latter being not dependent on the particles density, the meniscus continues to bulldoze particles until a plug is formed and so on.

CONCLUSION AND PERSPECTIVES

Throughout this study, we have revisited experimentally some classic effects characterizing the mechanical properties of confined granular media with the introduction of ferromagnetic pair interactions between the grains, resulting in new surprising behaviours.
The Janssen effect in ferromagnetic granular columns can be tuned with the direction and amplitude of an external magnetic field. In some preliminary, but particularly interesting experiments, we were able to tune the discharging rate of a silo and highlighted the presence of huge density fluctuations inside the packing. We also investigated in preliminary work the magnetic fatigue of the granular column.
We have also studied a frictional fluid system called the bulldozing experiment where particles, sedimented in a capillary, are carried away by an advancing meniscus. First, we could identify the key mechanisms for the onset of the bulldozing highlighting the emergence of a novel instability, the capillary wahsboarding. Finally, using ferromagnetic particles we demonstrated the possibility to trigger/force the bulldozing process. Because everything must have an end, we did not have time yet to investigate further the formation of plugs. Nevertheless, we can anticipate that applying a magnetic field, either vertical or horizontal, along the tube will result in the tunability of the Janssen effect and therefore a change of the plug characteristic sizes.
Future work on the magnetic fatigue of the granular column are intended to characterize fully the observed phenomenon. We also intend to analyse in details the discharge of the 2D magnetic silo to apprehend the dynamics of magnetic granular media. Finally, our use of index-matching liquid during the drainage of a frictional fluid highlighted the air invasion in the granular packing. This preliminary observation will lead in future work to the apprehension of the plug formation and mostly their typical length.

APPENDIX

A

PLUG PRESSURE

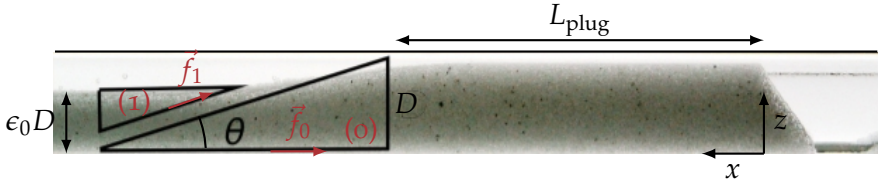

Figure A.1: Schematic of the plug during the bulldozing experiment.

We propose here to express the pressure needed to push a plug of grains bulldozing a sedimented layer, as shown in figure (A.1).
Since the plug is composed of a confined granular material, Janssen redirection of stresses occurs $\sigma_x = \kappa\sigma_r$. Moreover, the plug moving in the horizontal direction, we can assume that all friction forces at the capillary wall are mobilised in the horizontal direction $\tau = \mu\sigma_r$. Finally, we make the same assumption as Janssen and consider that the horizontal stress σ_x is homogeneous in the radial direction r. Note that this assumption is strong in this case due to gravity perpendicular to the x direction. All three assumptions lead to $\tau = \mu\kappa\sigma_z$.
Considering the apparent density of the plug with a random close packing fraction $\phi_c \approx 0.64$, the weight of the plug acts as a friction pad and the pressure exerted on the capillary wall σ_w is given by;

$$\sigma_w(x) = \mu\left(\kappa\sigma_{xx}(x) + \phi_c\Delta\rho g\frac{D}{4}\right). \tag{A.1}$$

A force equilibrium in the horizontal direction x gives:

$$\pi\frac{D^2}{4}\left(\sigma_x|_{x+\mathrm{d}x} - \sigma_x|_x\right) + \pi D\mathrm{d}x\sigma_w = 0 \tag{A.2}$$

that, when divided by the infinitesimal slice width $\mathrm{d}x$, leads to the differential equation;

$$\frac{\mathrm{d}\sigma_x(x)}{\mathrm{d}x} + \frac{4\mu\kappa}{D}\sigma_x(x) + \mu\phi_c\Delta\rho g = 0, \tag{A.3}$$

This equation, similar to the one obtained in the Janssen prediction, has the following solution:

$$\sigma_x(x) = A\exp(-4\mu\kappa x/D) - \phi_c\Delta\rho g D/(4\kappa), \tag{A.4}$$

with A a pre-factor determined later.
Ahead of the advancing plug, we can differentiate two granular zones, (0) where the advancing front, making an angle θ with the horizontal, bulldozes the particles in the deposit layer of height $\epsilon_0 D$, (1) where the particles in the

deposit layer are resting on the bulldozing area (o). The first zone bulldozing the sedimented layer can be approximated by a semi-cylinder of weight:

$$W_0 = \frac{1}{2}\left(\pi\frac{D^2}{4}\frac{D}{\tan\theta}\right)\phi_c\Delta\rho, \tag{A.5}$$

The bulldozed sedimented layer correspond to a partially filled half-cylinder of weight:

$$W_1 = \frac{1}{2}\left(\frac{1}{4}\arccos\left(1-2\epsilon_0\right) - \sqrt{\epsilon_0-\epsilon_0^2}\left(\frac{1}{2}-\epsilon_0\right)\right)\frac{D^3}{\tan\theta}\phi_c\Delta\rho \tag{A.6}$$

$$= \frac{1}{2}f(\epsilon_0)\frac{D^3}{\tan\theta}\phi_c\Delta\rho \tag{A.7}$$

The bulldozing zone (o) is sliding on the capillary, resulting in a frictional force $f_0 = \mu g W_0$, while the laying zone (1) is creating an additional friction stress on zone (o) supposed with the same friction coefficient μ, which projected on the horizontal direction is given by $f_1 = \mu g\cos\theta W_1$. Both forces lead to a stress limit at $x = L_{\text{plug}}$:

$$\sigma_{\text{front}} = \mu g\left(W_0 + \cos\theta W_1\right)\frac{4}{\pi D^2} \tag{A.8}$$

$$= \frac{2\mu g D\phi_c\Delta\rho}{\pi\tan\theta}\left(\frac{\pi}{4}+\cos\theta f(\epsilon_0)\right) \tag{A.9}$$

By equalizing both equations (A.4) for $x = L_{\text{plug}}$ and (A.9), we otain an expression for the pre-factor A:

$$A = \sigma_0(\phi,\mu,\kappa)\exp\left(4\mu\kappa L_{\text{plug}}/D\right), \tag{A.10}$$

with

$$\sigma_0(\epsilon_0,\mu,\kappa) = \phi_c\Delta\rho g D\left[\frac{1}{4\kappa}+\frac{2\mu}{\pi\tan\theta}\left(\frac{\pi}{4}+\cos\theta f(\epsilon_0)\right)\right] \tag{A.11}$$

The pressure exerted by the plug at $x = 0$ is then given by:

$$P\left(L_{\text{plug}}\right) \approx \sigma_0(\epsilon_0,\mu,\kappa)\exp\left(4\mu\kappa L_{\text{plug}}/D\right) - \phi_c\Delta\rho g D/(4\kappa). \tag{A.12}$$

Finally, by taking typical values for $\mu \approx 0.5$, $\kappa \approx 0.6$, $L_{\text{plug}} \approx 3D$, we can compare both terms in equation (A.12):

$$\frac{\sigma_0(\epsilon_0,\mu,\kappa)\exp\left(4\mu\kappa L_{\text{plug}}/D\right)}{\phi_c\Delta\rho g D/(4\kappa)} \approx \exp\left(4\mu\kappa L_{\text{plug}}/D\right) \approx 36 \gg 1. \tag{A.13}$$

To conclude, the pressure required to displace the granular plug writes:

$$\boxed{P\left(L_{\text{plug}}\right) \approx \sigma_0(\epsilon_0,\mu,\kappa)\exp\left(4\mu\kappa L_{\text{plug}}/D\right).} \tag{A.14}$$

B

CAPILLARY FILLING

We propose here to rationalize the filling of particles inside the capillary given in figure (4.1). To do so, we consider the geometry given in figure (B.1) and use the Shields parameter presented in section 1.3 that we recall here:

$$\Theta = \frac{\tau^f}{\Delta\rho g d} \,, \tag{B.1}$$

where the transport of particles occurs when $\Theta = 2\mu/9$, with μ the particles' friction coefficient.
In this geometry, we assume that the liquid flows in a restricted capillary of diameter $(1-\epsilon_0)D$. The velocity profile of the liquid is then given by the Hagen-Poiseuille flows [75]:

$$u = u_{\max}\left(1 - \left(\frac{2y}{(1-\epsilon_0)D}\right)^2\right) \,, \tag{B.2}$$

where in our case of a constant flow rate of liquid I_0 injected in the tube, $u_{\max} = 4I_0/(\pi D^2(1-\epsilon_0)^2)$. Finally, the shear stress used in the definition of the Shields parameter is given by:

$$\tau^f = \eta\frac{\mathrm{d}u}{\mathrm{d}y} = -4\eta u_{\max}\frac{y}{(1-\epsilon_0)^2 D^2} \,, \tag{B.3}$$

with η the fluid dynamic viscosity.
To determine the limit ϵ_0 reached for a given filling rate I_0, we suppose that the sedimented layer of particles is stable if a particle placed on its top at

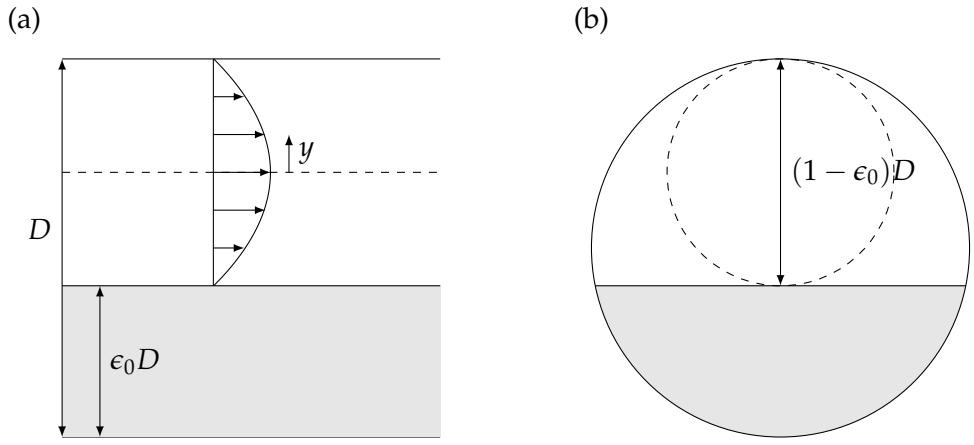

Figure B.1: Partially filled tube geometry. (a) Side view. (b) Front View.

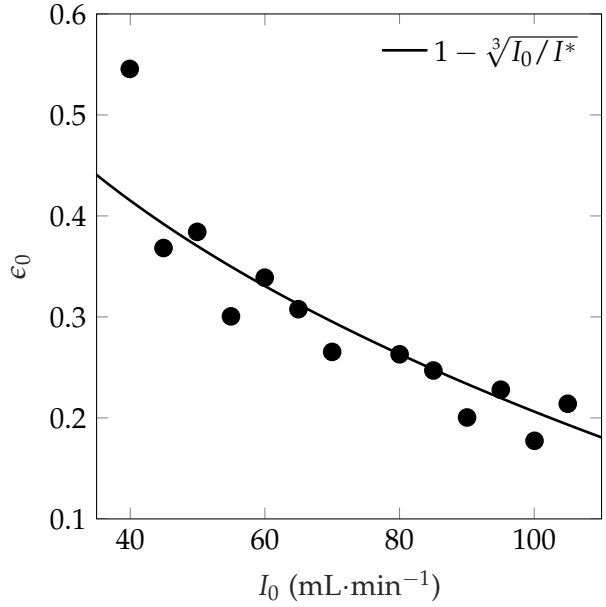

Figure B.2: Height of sedimented layer injected in the tube dependence on the injection rate I_0.

$y = -(1-\epsilon_0)D/2 + a$ is carried away by the fluid.
First, we express the shear stress exerted on this particle:

$$\tau^f = 4\eta u_{\max} \frac{1}{(1-\epsilon_0)^2 D^2} \left(\frac{(1-\epsilon_0)D}{2} - a \right) \approx \frac{2\eta u_{\max}}{(1-\epsilon_0)D}\,, \tag{B.4}$$

where we neglected the second term since $a/D \approx 0.05$ in our experiments.
The Shields criterion finally writes:

$$\frac{2\mu}{9}\Delta\rho g 2a = \eta \frac{8I_0}{\pi D^3 (1-\epsilon_0)^3}, \tag{B.5}$$

$$(1-\epsilon_0)^3 = \frac{18\eta I_0}{\pi D^3 \mu \Delta\rho g a}. \tag{B.6}$$

The filling fraction ϵ_0 reached for a given injection rate I_0 of the liquid is then given by $\epsilon_0 = 1 - \sqrt[3]{I_0/I^*}$ with:

$$I^* = \frac{\pi D^3 \mu \Delta\rho g a}{18\eta}. \tag{B.7}$$

With our experimental values, we find $I^* = 34\,\mathrm{ml}\cdot\mathrm{min}^{-1}$ to be compared with the experimental values, as shown in figure (B.2). Our prediction is slightly over the experimental results, which is not surprising regarding our assumptions, mainly about the geometry of the partially filled tube shown in figure (B.1.b). We propose to correct our prediction by fitting our experimental results by the law:

$$\epsilon_0 = 1 - \sqrt[3]{I_0/I^*}, \tag{B.8}$$

giving $I^* = 200\,\mathrm{ml}\cdot\mathrm{min}^{-1}$.

BIBLIOGRAPHY

[1] H. M. Jaeger, S. R. Nagel, and R. P. Behringer. "Granular solids, liquids, and gases." In: *Reviews of Modern Physics* 68.4 (Oct. 1996), pp. 1259–1273.

[2] P.-G. de Gennes. "Reflections on the mechanics of granular matter." In: *Physica A: Statistical Mechanics and its Applications* 261.3-4 (Dec. 1998), pp. 267–293.

[3] P.-G. de Gennes. "Granular matter: a tentative view." In: *Reviews of Modern Physics* 71.2 (Mar. 1999), S374–S382.

[4] FAO. *Crop Prospects and Food Situation #3, September 2020*. FAO, 2020.

[5] F. B. Wadsworth et al. "The force required to operate the plunger on a French press." In: *American Journal of Physics* 89.8 (Aug. 2021), pp. 769–775.

[6] L. Vanel and E. Clément. "Pressure screening and fluctuations at the bottom of a granular column." In: *The European Physical Journal B* 11.3 (Oct. 1999), pp. 525–533.

[7] G. Ovarlez, C. Fond, and E. Clément. "Overshoot effect in the Janssen granular column: A crucial test for granular mechanics." In: *Physical Review E* 67.6 (June 2003).

[8] B. Andreotti, Y. Forterre, and O. Pouliquen. *Granular Media*. Cambridge University Press, 2009. Chap. 2, pp. 22–23.

[9] J.-P. Bouchaud, M. E. Cates, and P. Claudin. "Stress Distribution in Granular Media and Nonlinear Wave Equation." In: *Journal de Physique I* 5.6 (June 1995), pp. 639–656.

[10] J. P. Wittmer, M. E. Cates, and P. Claudin. "Stress propagation and Arching in Static Sandpiles." In: *Journal de Physique I* 7.1 (Jan. 1997), pp. 39–80.

[11] I. Bratberg, K. J. Måløy, and A. Hansen. "Validity of the Janssen law in narrow granular columns." In: *The European Physical Journal E* 18.3 (Oct. 2005), pp. 245–252.

[12] S. Mahajan et al. "Reverse Janssen Effect in Narrow Granular Columns." In: *Physical Review Letters* 124.12 (Mar. 2020).

[13] J. P. Peralta et al. "Apparent mass during silo discharge: Nonlinear effects related to filling protocols." In: *Powder Technology* 311 (Apr. 2017), pp. 265–272.

[14] M. Benyamine et al. "Discharge flow of a bidisperse granular media from a silo." In: *Physical Review E* 90.3 (Sept. 2014).

[15] M. A. Aguirre et al. "Pressure Independence of Granular Flow through an Aperture." In: *Physical Review Letters* 104.23 (June 2010).

[16] C. Perge et al. “Evolution of pressure profiles during the discharge of a silo.” In: *Physical Review E* 85.2 (Feb. 2012).

[17] C. Mankoc et al. “The flow rate of granular materials through an orifice.” In: *Granular Matter* 9.6 (Sept. 2007), pp. 407–414.

[18] W. Beverloo, H. Leniger, and J. van de Velde. “The flow of granular solids through orifices.” In: *Chemical Engineering Science* 15.3-4 (Sept. 1961), pp. 260–269.

[19] A. Marin et al. “Clogging in constricted suspension flows.” In: *Physical Review E* 97.2 (Feb. 2018).

[20] I. Zuriguel et al. “Clogging transition of many-particle systems flowing through bottlenecks.” In: *Scientific Reports* 4.1 (Dec. 2014).

[21] X. Wu et al. “Why hour glasses tick.” In: *Physical Review Letters* 71.9 (Aug. 1993), pp. 1363–1366.

[22] A. Nicolas et al. “A counterintuitive way to speed up pedestrian and granular bottleneck flows prone to clogging: can ‘more’ escape faster?” In: *Journal of Statistical Mechanics: Theory and Experiment* 2018.8 (Aug. 2018), p. 083403.

[23] R. Kumar and B Bhattacharjee. “Porosity, pore size distribution and in situ strength of concrete.” In: *Cement and Concrete Research* 33.1 (Jan. 2003), pp. 155–164.

[24] A. M. Neville and J. J. Brooks. *Concrete technology*. 2nd edition. Prentice Hall, 2010.

[25] E. Rouèche. “Influence des paramètres de vibrations sur la rhéologie d’un milieu granulaire : Application au remplissage des fusibles.” PhD thesis. Ecole Nationale Supérieure des Mines de Saint-Etienne, 2005.

[26] J. B. Knight et al. “Density relaxation in a vibrated granular material.” In: *Physical Review E* 51.5 (May 1995), pp. 3957–3963.

[27] T. Divoux, H. Gayvallet, and J.-C. Géminard. “Creep Motion of a Granular Pile Induced by Thermal Cycling.” In: *Physical Review Letters* 101.14 (Oct. 2008).

[28] P. Richard et al. “Slow relaxation and compaction of granular systems.” In: *Nature Materials* 4.2 (Feb. 2005), pp. 121–128.

[29] P Philippe and D Bideau. “Compaction dynamics of a granular medium under vertical tapping.” In: *Europhysics Letters (EPL)* 60.5 (Dec. 2002), pp. 677–683.

[30] K. L. Johnson. *Contact Mechanics*. Cambridge University Press, May 1985, pp. 306–311.

[31] P. A. Cundall and O. D. L. Strack. “A discrete numerical model for granular assemblies.” In: *Géotechnique* 29.1 (Mar. 1979), pp. 47–65.

[32] T. Weinhart et al. “Fast, flexible particle simulations — An introduction to MercuryDPM.” In: *Computer Physics Communications* 249 (Apr. 2020), p. 107129.

[33] M. Pakpour et al. "How to construct the perfect sandcastle." In: *Scientific Reports* 2.1 (Aug. 2012).

[34] L. Bocquet, É. Charlaix, and F. Restagno. "Physics of humid granular media." In: *Comptes Rendus Physique* 3.2 (Jan. 2002), pp. 207–215.

[35] P.-G. de Gennes, F. Brochard-Wyart, and D. Quéré. *Capillarity and wetting phenomena: drops, bubbles, pearls, waves*. eng. New York, NY: Springer, 2010.

[36] P. C. F. Møller and D. Bonn. "The shear modulus of wet granular matter." In: *Europhysics Letters (EPL)* 80.3 (Oct. 2007), p. 38002.

[37] E. Mersch et al. "Effect of an electric field on an intermittent granular flow." In: *Physical Review E* 81.4 (Apr. 2010).

[38] B. F. Edwards and J. M. Edwards. "Dynamical interactions between two uniformly magnetized spheres." In: *European Journal of Physics* 38.1 (Nov. 2016), p. 015205.

[39] J. Vessaire et al. *Sedimentation of a suspension of paramagnetic particles in an external magnetic field*. Aug. 2020.

[40] G. Lumay and N. Vandewalle. "Controlled flow of smart powders." In: *Physical Review E* 78.6 (Dec. 2008).

[41] K. Bai et al. "Effective magnetic susceptibility of suspensions of ferromagnetic particles." In: *Journal of Applied Physics* 124.12 (Sept. 2018), p. 123901.

[42] G. Lumay and N. Vandewalle. "Flow of magnetized grains in a rotating drum." In: *Physical Review E* 82.4 (Oct. 2010).

[43] G. Lumay et al. "Packing fraction and compaction dynamics of magnetic powders." In: *AIP Conference Proceedings*. AIP, 2009.

[44] G. Lumay and N. Vandewalle. "Tunable random packings." In: *New Journal of Physics* 9.11 (Nov. 2007), pp. 406–406.

[45] N. Vandewalle et al. "Flow properties and heap shape of magnetic powders." In: *AIP Conference Proceedings*. AIP, 2009.

[46] G. Lumay et al. "Flow of magnetic repelling grains in a two-dimensional silo." In: *Papers in Physics* 7.0 (Sept. 2015).

[47] J. Bernard and L. Thorens. "Channel formation in draining suspensions." In: *Emergent Scientist* 2 (2018), p. 4.

[48] M. M. Mrokowska et al. "Laboratory studies on bedload transport under unsteady flow conditions." In: *Journal of Hydrology and Hydromechanics* 66.1 (Nov. 2017), pp. 23–31.

[49] B. Andreotti, Y. Forterre, and O. Pouliquen. *Granular Media*. Cambridge University Press, 2009. Chap. 8, pp. 313–319.

[50] A. Daerr et al. "Erosion patterns in a sediment layer." In: *Physical Review E* 67 (2003), 065201(R).

[51] B. Sandnes et al. "Labyrinth Patterns in Confined Granular-Fluid Systems." In: *Physical Review Letters* 99.3 (2007), p. 038001.

[52] G. Dumazer et al. "Frictional Fluid Dynamics and Plug Formation in Multiphase Millifluidic Flow." In: *Physical Review Letters* 117.2 (2016), p. 028002.

[53] B. Sandnes et al. "Patterns and flow in frictional fluid dynamics." In: *Nature Communications* 2.1 (2011).

[54] H. A. Knudsen et al. "Granular labyrinth structures in confined geometries." In: *Physical Review E* 77.2 (2008).

[55] H. A. Knudsen et al. "Labyrinth patterns in confined and tilted granular-fluid systems." In: *AIP Conference Proceedings* 1145 (2009), pp. 1043–1046.

[56] K. S. Olsen and J. M. Campbell. "Diffusion Entropy and the Path Dimension of Frictional Finger Patterns." In: *Frontiers in Physics* 8 (Mar. 2020).

[57] G. Dumazer et al. "Self-Structuring of Granular material under Capillary Bulldozing." In: *EPJ Web of Conferences* 140 (2017). Ed. by F. Radjai et al., p. 09016.

[58] G. Dumazer et al. "Capillary bulldozing of sedimented granular material confined in a millifluidic tube." In: *Physical Review Fluids* 5.3 (2020).

[59] Y. Bertho, F. Giorgiutti-Dauphiné, and J.-P. Hulin. "Dynamical Janssen Effect on Granular Packing with Moving Walls." In: *Physical Review Letters* 90.14 (Apr. 2003).

[60] N. A. Spaldin. *Magnetic Materials*. Cambridge University Press, 2009. Chap. 2, p. 18.

[61] J. W. Landry et al. "Confined granular packings: Structure, stress, and forces." In: *Physical Review E* 67.4 (Apr. 2003).

[62] K. M. Hill et al. "Mixing of granular materials: a test-bed dynamical system for pattern formation." In: *International Journal of Bifurcation and Chaos* 09.08 (Aug. 1999), pp. 1467–1484.

[63] N. Jain, J. M. Ottino, and R. M. Lueptow. "Regimes of segregation and mixing in combined size and density granular systems: an experimental study." In: *Granular Matter* 7.2-3 (Mar. 2005), pp. 69–81.

[64] H. Xiao et al. "Modelling density segregation in flowing bidisperse granular materials." In: *Proceedings of the Royal Society A* 472.2191 (July 2016), p. 20150856.

[65] D. Stauffer. *Introduction to percolation theory*. London Washington, DC: Taylor & Francis, 1992. Chap. 2.

[66] T. L. Pennec et al. "Ticking hour glasses: Experimental analysis of intermittent flow." In: *Physical Review E* 53.3 (Mar. 1996), pp. 2257–2264.

[67] G. W. Baxter et al. "Pattern formation in flowing sand." In: *Physical Review Letters* 62.24 (June 1989), pp. 2825–2828.

[68] E. Freyssingeas, M.-J. Dalbe, and J.-C. Géminard. "Flowers in flour: Avalanches in cohesive granular matter." In: *Physical Review E* 83.5 (May 2011).

[69] D. Borrero-Echeverry and B. C. A. Morrison. "Aqueous ammonium thiocyanate solutions as refractive index-matching fluids with low density and viscosity." In: *Experiments in Fluids* 57.7 (July 2016).

[70] G. Vazquez, E. Alvarez, and J. M. Navaza. "Surface Tension of Alcohol Water + Water from 20 to 50 .degree.C." In: *Journal of Chemical & Engineering Data* 40.3 (May 1995), pp. 611–614.

[71] D. C. Mays and B. A. Faybishenko. "Washboards in unpaved highways as a complex dynamic system." In: *Complexity* 5.6 (2000), pp. 51–60.

[72] B. Percier, S. Manneville, and N. Taberlet. "Modeling a washboard road: From experimental measurements to linear stability analysis." In: *Physical Review E* 87 (2013), p. 12203.

[73] N. Taberlet, S. W. Morris, and J. N. McElwaine. "Washboard Road: The Dynamics of Granular Ripples Formed by Rolling Wheels." In: *Physical Review Letters* 99.6 (Aug. 2007).

[74] B. Percier et al. "Lift and drag forces on an inclined plow moving over a granular surface." In: *Physical Review E* 84.5 (2011), p. 051302.

[75] A. Ostadfar. "Fluid Mechanics and Biofluids Principles." In: *Biofluid Mechanics*. Elsevier, 2016, pp. 1–60.

PAPERS

I - Thorens L., Måløy K. J., Bourgoin M., & Santucci S. (2021). *Magnetic Janssen effect*. Nature Communications, 12(1). https://doi.org/10.1038/s41467-021-22722-y

II - Thorens L., Måløy K. J., Bourgoin M., & Santucci S. (2021). *Taming the Janssen effect*. EPJ Web of Conferences, 249, 08004. https://doi.org/10.1051/epjconf/202124908004

III - Thorens L., Måløy K. J., Bourgoin M., & Santucci, S. (in preparation). *Magnetic Janssen Effect in hybrid granular media*

IV - Thorens L., Viallet M., Måløy K. J., Bourgoin M., & Santucci, S. (2021). *Discharge of a 2D magnetic silo*. EPJ Web of Conferences, 249, 03017. https://doi.org/10.1051/epjconf/202124903017

V - Thorens L., Måløy K. J., Flekkøy E. G., Sandnes B., Bourgoin M., & Santucci, S. (in preparation). *Capillary washboarding during the slow drainage of a frictional fluid*

nature COMMUNICATIONS

ARTICLE

https://doi.org/10.1038/s41467-021-22722-y OPEN

Magnetic Janssen effect

L. Thorens [1,2], K. J. Måløy [2], M. Bourgoin [1] & S. Santucci [1,3]✉

A pile of grains, even when at rest in a silo, can display fascinating properties. One of the most celebrated is the Janssen effect, named after the pioneering engineer who explained the pressure saturation at the bottom of a container filled with corn. This surprising behavior arises because of frictional interactions between the grains through a disordered network of contacts, and the vessel lateral walls, which partially support the weight of the column, decreasing its apparent mass. Here, we demonstrate control over frictional interactions using ferromagnetic grains and an external magnetic field. We show that the anisotropic pairwise interactions between magnetized grains result in a radial force along the walls, whose amplitude and direction is fully determined by the applied magnetic field. Such magnetic Janssen effect allows for the fine tuning of the granular column apparent mass. Our findings pave the way towards the design of functional jammed materials in confined geometries, via a further control of both their static and dynamic properties.

[1] Univ Lyon, ENS de Lyon, Univ Claude Bernard, CNRS, Laboratoire de Physique, Lyon, France. [2] PoreLab, The Njord Centre, Department of Physics, University of Oslo, Oslo, Norway. [3] Lavrentyev Institute of Hydrodynamics, Siberian Branch of the Russian Academy of Sciences, Novosibirsk, Russia. ✉email: stephane.santucci@ens-lyon.fr

Granular media are ubiquitous in everyday life, in both natural and man-made systems. Their handling is of prime importance for a wide range of major industrial sectors, from civil engineering, to mining, agriculture, food, chemical and pharmaceutical industries. Around 40 billion of tonnes of sand and gravels are extracted every year for the building industry, while 2.5 billion of tonnes of iron ores and more than 2 billion of tonnes of cereals are produced annually[1]. These colossal quantities which keep on increasing with dramatic environmental consequences explain why granular matter appears as the second most manipulated material after water[2]. Even the smallest improvement in our understanding of particulate materials may have profound economic and societal impacts. However, granular media still confront engineers and physicists with challenging fundamental questions, which over the last decades has triggered an upsurge of studies within a very active research community[2–6]. They can display unusual physical properties, common to a wide range of amorphous materials, such as foams, emulsions and gels. These Soft Jammed Materials exhibit a peculiar dual mechanical behavior arising from their complex disordered microstructure: they behave as solids at rest, while they unjam and flow like liquids above a critical yield stress[6–9].

Here, we focus on the simplest static configuration, commonly encountered in our daily lives: a container filled with a granular assembly up to a given height. For sufficiently tall column (higher than the vessel diameter), the pressure at its bottom saturates at a value much smaller than the hydrostatic pressure that one would measure for a Newtonian liquid column. In order to understand and avoid the failure of silos, which is still an industrial problem nowadays, Janssen proposed in a seminal work[10] a simple continuum phenomenology to explain this puzzling behavior. His model relies on three hypothesis, (i) within the grains packing, the vertical stresses σ_z are redistributed proportionally to the horizontal ones, $\sigma_r = k\sigma_z$, with a phenomenological constant k (ii) the frictional contact forces F_z between the particles and the walls are at their Coulomb threshold, $F_z = \mu F_r$ with μ the friction coefficient between the grains and the wall, and (iii) the grain assembly is considered as a continuous medium. These assumptions lead to the description of a mass screening: the apparent mass $m_J = m_\infty[1 - \exp(-m_0/m_\infty)]$ saturates exponentially at a value $m_\infty = (\lambda/h)m_0$, with the characteristic length scale $\lambda = 2R/(4\mu k)$, $2R$ being the silo diameter, and m_0 the total mass of grains. Despite some criticisms and refinements[5,9,11–14], Janssen's approach has become a "classic", and its predictions have been shown to accurately describe experimental data, as long as the packing preparation leads to a full mobilization of the frictional forces along the container wall.

We propose here to revisit this classic problem by extending it to the case of ferromagnetic particles. One can then easily control and tune the interactions between the grains of the packing (using an external magnetic field), in contrast for instance to the influence of the particles shape and roughness on the frictional properties[15,16], or to the cohesive forces induced by capillary bridges in a humid environment[17–21], or by the occurrence of triboelectric charges[22,23], which are all much more difficult to control. Similar systems have already been used to modify the packing fraction and repose angle of a granular pile[24–28], as well as its flowing behavior in a silo or in a rotating drum[27,29]. When applying an external magnetic field $\mathbf{B}$, ferromagnetic particles acquire a magnetization with a dipolar moment $\mathbf{d} = V\chi_m/\mu_0\mathbf{B}$, with V the volume of the grain, μ_0 the magnetic permeability of vacuum and χ_m the volume susceptibility of the grain. Therefore, each particle i of the packing will interact with any other particle j via the dipole-dipole interactions[30]:

$$\mathbf{f_{ij}} = \frac{3\mu_0}{4\pi r_{ij}^5}\left(d^2\left(1 - 5\cos^2\alpha\right)\mathbf{r_{ij}} + 2dr_{ij}\mathbf{d}\cos\alpha\right), \qquad (1)$$

with the interaction potential, $U_{ij} = \frac{\mu_0 d^2}{4\pi r_{ij}^3}(1 - 3\cos^2\alpha)$, where α is the angle between the applied magnetic field and the separation vector $\mathbf{r_{ij}}$ between grains i and j. Interestingly, as illustrated on Fig. 1a, the induced magnetic dipolar pair interaction displays an anisotropic multi-polar field, either repulsive or attractive depending on the relative position of the grains, and the applied magnetic field direction. The dimensionless number that compares the strength of the magnetic interactions with the weight of the grains $\Psi = \frac{\chi_m^2 {B_0}^2}{\mu_0 a\rho g}$, with χ_m the magnetic susceptibility (ceiling at 3 for spherical grains assembly[31]), quantifies the involved interactions[28,32].

Results

Two series of measurements were performed with a vertical and a horizontal magnetic field. Figure 2a, b show the apparent measured mass as a function of the actual total mass of poured grains m_0 for various amplitude B_0 of the applied field, quantified by the parameter Ψ, which in our experiments ranges from 1.5 to ~35. First, without any magnetic field applied, $\Psi = 0$, we retrieve the typical exponential saturation of the measured mass predicted by Janssen[10]. Fitting our experimental data in the absence of magnetic field by Janssen' expression of m_J, with the saturation mass m_∞ as a single free parameter, we obtain $m_\infty = 48$ g, characteristic of our

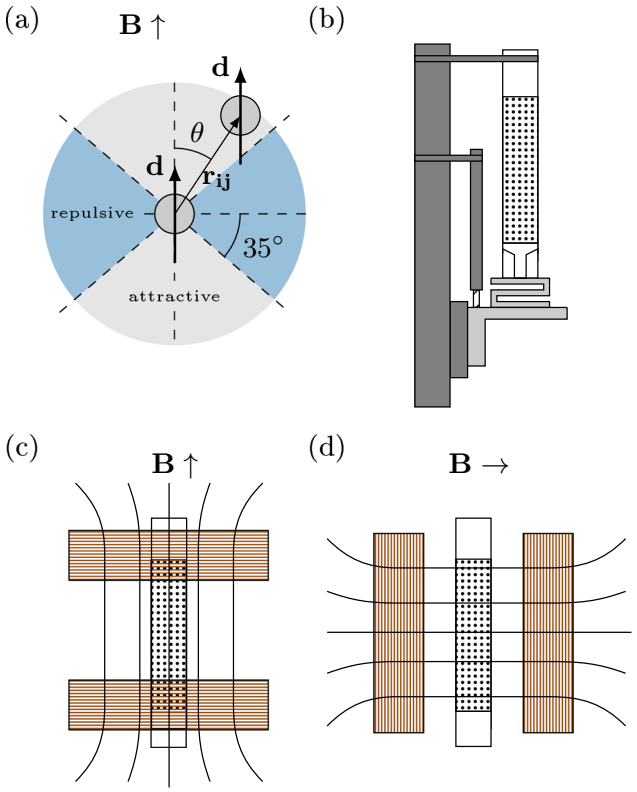

Fig. 1 Experimental setup. a Anisotropic magnetic dipolar interaction between two ferromagnetic particles subjected to the magnetic field **B**. **b** Ferromagnetic particles fill a cylindrical tube and rest on a piston fixed to a force sensor. This piston can be displaced vertically thanks to a motorized translation stage. **c**, **d** The column is placed between two magnetic coils mounted in a Helmoltz vertical or horizontal configuration to create a uniform magnetic field.

granular column. This fit is provided in Supplementary Information. We observe a deviation from Janssen's prediction as soon as a magnetic field is applied to the granular column. This is particularly evident for a vertical field and tall columns for which we observe a decrease of the packing apparent mass, as the amplitude of the magnetic field is increased. For small applied amplitudes the measured mass is still well described by Janssen's model, although with a decreasing saturating mass m_∞ and thus a larger phenomenological constant k, quantifying the radial redistribution of vertical stresses within the packing. For high amplitudes of the magnetic field, a striking more is less effect is observed. For tall columns, adding more grains lowers the measured mass!

The impact of a horizontal magnetic field on the apparent mass of the packing is less pronounced, although we can still observe a small but systematic increase of the measured mass for tall columns with Ψ. This could be interpreted, within the Janssen approach, as a reduction of the radial redistribution of stresses.

These results may appear counter-intuitive. Indeed, one may expect particles to reorganize, tending to align and form chains in the direction of the applied field. This would potentially increase the force on the lateral walls for horizontal fields, while increasing the vertical force and the apparent mass for a vertical applied field. However, using a transparent glass tube we detected no such rearrangement nor motion of the particles .

In order to analyze more deeply the deviations between our measurements and the classical Janssen prediction, we show in Fig. 2c the mass difference $m - m_J$ for a series of experiments performed at the maximum amplitude of the magnetic field $\Psi = 35$. Interestingly, while we clearly observe again the strong

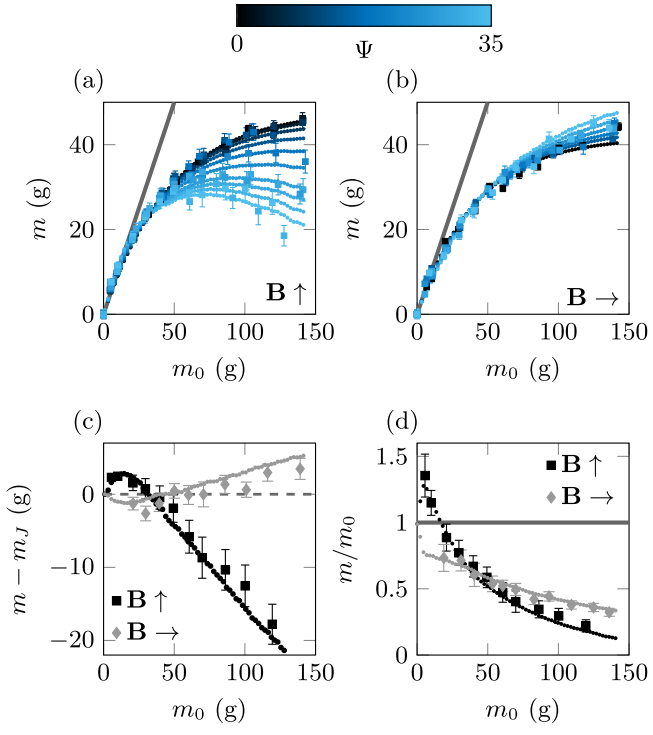

Fig. 2 Apparent mass measurements and predictions. a, **b** Mass measurement of the bead packing for different field intensity, characterized by Ψ, and direction. The gray line corresponds to the hydrostatic limit. For a field amplitude $\Psi = 35$, **c** gives the difference between the mass measurement and Janssen prediction m_J; while **d** displays the mass measurement renormalized by the true mass of the column m_0, the gray line corresponds to the hydrostatic limit, $m = m_0$. Our theoretical model (points reported on the various panels) reproduces quantitatively our experimental measurements (square symbols).

deviation to the classical exponential saturation for tall columns, with a lower (resp. larger) apparent mass for a vertical (resp. horizontal) magnetic field direction, we notice another striking behavior, where the effect reverses, for rather short granular columns, with a mass $m_0 \lesssim 30$ g, corresponding to a height typically smaller than the silo diameter. Indeed, when applying a vertical magnetic field to short columns, we observe an overshoot, where the measured mass appears slightly larger (peaking at 30–40% of m_0 for the highest values of magnetic field we explored) than the actual mass of the packing. This can be seen in Fig. 2d, where the apparent mass m is renormalized by the actual mass of the packing m_0, with the magnetic field fixed at its maximum amplitude. Such a puzzling magnetic reverse Janssen effect is reminiscent of recently reported results[33], where a delicate sequential filling protocol of a narrow container leads to the emergence of compressional frictional forces with conventional (non magnetic) beads. The present study goes beyond this, by indicating the possibility to control the reverse Janssen phenomenon, without requiring any specific filling protocol[34,35], via tunable particle-particle magnetic interactions. With horizontal magnetic fields, for short columns, we instead obtain an undershoot, with an apparent mass smaller than the actual mass of the packing. Our results and more specifically our model (described below) suggest that this overshoot presents a maximum, which occurs for a column height of only a few particle diameters. The high density of the ferromagnetic particles renders a thorough study difficult. In contrast, the reverse Janssen effect reported in[33] with less dense particles, is found maximum for columns heights exceeding ten particle diameters. These observations suggest interesting strategies to potentially finely tune this reverse effect, by investigating the combined role of the applied field, the tube to particle diameter and the particles density.

Model. To rationalize our measurements, we first need to consider all the pairwise dipole-dipole interactions within the ferromagnetic granular packing. For a given particle j, f_j^β, with $\beta = r, \theta, z$, gives respectively the radial, azimuthal and vertical components of the magnetic force resulting from its dipolar interaction with all the other particles. The components of the total net force associated with the magnetic effects on the whole packing, of height h, are given by $F^\beta(h) = \sum_i f_i^\beta$, where the sum is taken over all the particles of the packing. Due to the cylindrical symmetry of the set-up, $f_j^\theta = 0$, so that there is no net azimuthal force. For the vertical component, the mirror symmetry of the system with respect to the mid-plane ($z = h/2$) means that contributions of two symmetric particles j and j' compensate each other ($f_j^z = -f_{j'}^z$) and have a zero net effect on the global force. Thus, magnetic interactions do not add any global net vertical force on the packing. The only global effect of magnetic interactions on the packing is on the radial component. Such radial effects can be anticipated to be maximal near the walls of the container. Indeed, for a particle j placed along the symmetry axis of the container ($r_j = 0$), symmetry constraints impose that $f_j^r = 0$, as radial magnetic pair interactions of a particle on the axis with its symmetric neighbors average to zero. Conversely, if the particle j is off-axis, a radial net force f_j^r emerges due to the symmetry breaking related to the finite-size of the silo, as illustrated in Fig. 3a.

Those magnetic interactions can be computed numerically using Eq. (1) and the positions of particles within a packing generated by a Discrete Element Method simulation[36,37]. Figure 3b shows a typical spatial (r,z) map of the radial component of the magnetic force (averaged over the angular coordinate θ), for a 10 cm high column, under a vertical applied

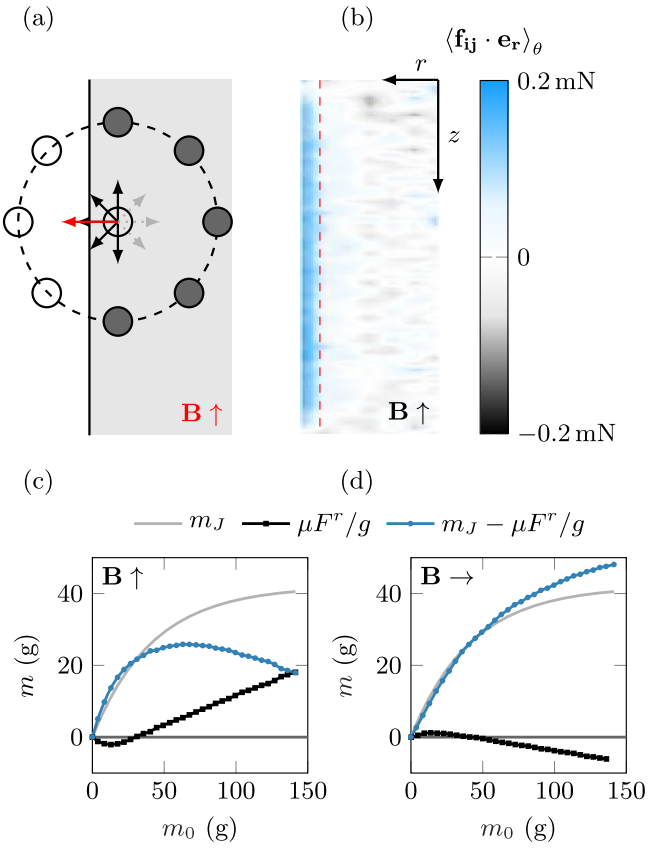

Fig. 3 Magnetic Janssen effect model. a The magnetic force on a particle within the packing, but off-the vertical axis, induced by neighboring ones (in dark gray), is non-zero and along the radial direction, due to the tube finite-size, and the non-compensation of the forces from the missing particles (in white). For a vertical magnetic field, the resulting radial force is repulsive (red arrow), as confirmed by the right panel. **b** Numerical computation of a spatial (*r*,*z*) map of the magnetic pair-interaction radial component (averaged over the coordinate θ) for a 10 cm column, submitted to a magnetic field of $\Psi = 35$. Model curves for each direction of the magnetic field (**c** vertical, **d** horizontal). The light gray line shows Janssen prediction; the black squares line is the result of the computed magnetic mass loss $\mu F^r/g$; the blue circles line (difference of both curves) gives the predicted apparent mass of the column.

field ($\Psi = 35$). In this case, we observe that the magnetic pair interactions result in a radial repulsive force concentrated at the walls. Furthermore, this radial force appears constant along the vertical position z, independent of the column height, except at the top and bottom due to the edge effect (see Supplementary Material for more details). As a result, for sufficiently tall columns $h > 2R$, we expect a linear dependence of the global radial force F^r with the packing mass m_0, as observed in Fig. 3c. For short columns $h < 2R$, corresponding to a packing mass m_0 smaller than 30 g, edges effects are dominant. Nevertheless, for this case of a vertical magnetic field, the magnetic interactions are found to be mostly attractive (see Fig. S6 in Supplementary Material), resulting in a negative global radial force F^r. Repulsive and attractive magnetic interactions compensate and cancel out for a column height around $h = 2R$.

Finally, we follow Janssen's approach in order to estimate the contribution of this radial force to the effective mass of the packing. We consider the granular packing as a cohesive continuous medium, and the particles wall contacts at the Coulomb limit, such that the radial net magnetic force $F^r(h)$ can be associated to a global vertical contribution to the pressure measured at the bottom of the silo, $F(h) = -\mu F^r(h)$. The minus sign accounts for the fact that a positive (outwards) radial contribution corresponds to a stronger force supported by the walls, hence reducing the apparent mass of the column. Such "magnetic Janssen effect" can therefore be either compressive or tensile depending on the sign of F^r, leading to a tunable –enhanced or hindered– apparent mass of the ferromagnetic packing, $m = m_J - \frac{\mu}{g}F^r(h)$.

Computing the global radial force $F^r(h)$ for various packing heights, the resulting predicted apparent mass is displayed in Fig. 3c, d (blue curve), for a vertical and horizontal magnetic field (of a fixed amplitude, $\Psi = 35$ and a friction coefficient $\mu = 0.40 \pm 0.05$) as a function of the actual granular mass. The contribution from the classical Janssen effect and the additional magnetic effect are also shown. Figure 2 demonstrates that our theoretical approach reproduces quantitatively all the experimental measurements, without any adjustable parameter.

Discussion

Importantly, our model predicts that for sufficiently tall columns (typically taller than the silo diameter), the magnetic contribution to the apparent mass evolves linearly with the actual added mass m_o. In particular, when a vertical field is applied, the apparent mass decreases linearly with m_o, pointing towards the existence of an invisibility threshold corresponding to a critical total mass $m_0^c(B_0)$ (dependent on the applied field amplitude) above which the apparent mass vanishes and the column becomes undetectable at the bottom of the silo. Alternatively, for a given total mass m_0, invisibility can be reached by adjusting the amplitude of the magnetic field above a critical amplitude ${B_0}^c(m_0)$.

Figure 4a shows how this invisibility threshold m_0^c, computed numerically, evolves with the amplitude of the magnetic field, given by the dimensionless number Ψ. We observe that this critical mass m_0^c decreases as a power-law with Ψ, $m_0^c \propto \Psi^{-1}$, with an exponential cut-off at large magnetic field (corresponding also to small granular columns).

We can furthermore predict such scaling behavior, following our derived expression of the apparent mass of the ferromagnetic granular column, with a given applied field,

$$m = m_J - \frac{\mu}{g}F^r(m_0^c, \Psi) = 0 \qquad (2)$$

The total radial magnetic force F^r is directly proportional to the magnetic field strength dimensionless number Ψ. Furthermore, as already mentioned, this magnetic force increases linearly with m_0, $F^r \propto (m_0 - m_0^{2R})$, where $m_0^{2R} \simeq 30$ g the actual mass of the granular column of height $h = 2R$, the silo diameter (see Fig. S6 in Supplementary Material). Considering tall columns ($h >> 2R$), the Janssen mass has reached its saturation value, $m_J \simeq m_\infty$, and the actual mass of the packing m_0 is thus larger than m_0^{2R}, such that, $F^r(m_0^c, \Psi) \propto (m_0^c - m_0^{2R})\Psi \simeq m_0^c\Psi$. We therefore obtain the following scaling for this critical mass, $m_0^c \propto m_\infty \frac{g}{\mu}\Psi^{-1}$, in excellent agreement with our numerical computation.

The predicted values of this critical mass m_0^c are beyond the experimentally reachable ones, set by the limits of our current set-up: the maximum intensity of the external magnetic field $B_{max} \simeq 170$ G, (leading to $\Psi \simeq 35$) is fixed by the maximum electrical power that the coils can handle, while granular columns taller than $h_{max} \simeq 10$ cm, (which corresponds to a mass around 150 g) experience inhomogeneous applied field. These experimental limitations are displayed on the Fig. 4a, b. Nevertheless, Fig. 4 a shows that the invisibility condition ($\Psi \simeq 35, m_0^c \simeq 250$ g) is not so far from the experimental limits of our apparatus. We have therefore performed a single apparent mass measurement for a very tall column ($h_{max} \simeq 15$ cm) corresponding to an actual

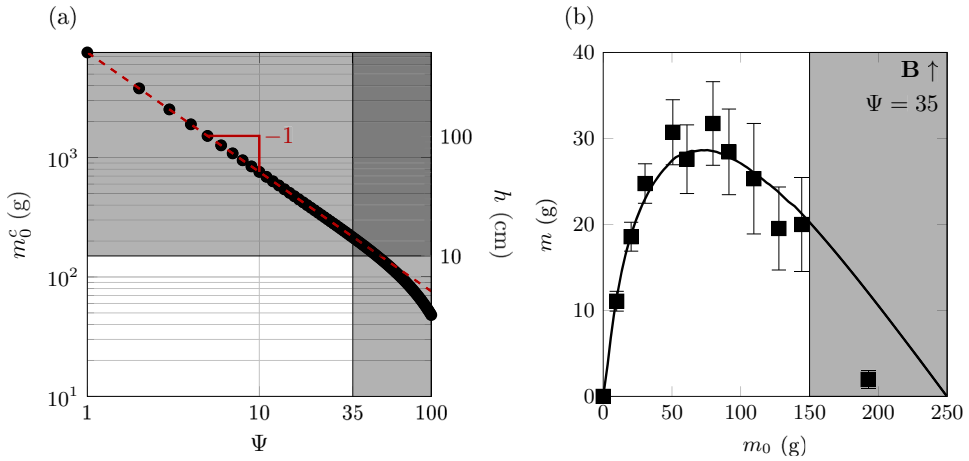

Fig. 4 Invisibility threshold and experimental limitations. a Numerical computation of the critical mass m_0^c, for which the apparent mass of the packing is zero, as a function of the magnetic field strength, given by the dimensionless number Ψ. This critical mass decreases as a power-law, $m_0^c \propto \Psi^{-1}$, as predicted theoretically. The gray zones represent the mass and magnetic field intensity that cannot be reached by our experimental apparatus. **b** Apparent mass measurement for the highest magnetic field intensity, applied vertically, and comparison to our model (black line).

mass around 200 g, with a vertical magnetic field of maximum amplitude ($\Psi \simeq 35$), presented in Fig. 4b. Strikingly, we observed that the granular column becomes invisible with an apparent mass close to zero in these conditions. This is in qualitative agreement with our model. Indeed, this critical mass appears slightly smaller than our theoretical prediction, $m_0^c = 250\,\mathrm{g}$, probably due to the fact that the applied magnetic field for such a tall granular column is not perfectly homogeneous all along the packing.

To conclude, the present study reveals a magnetic Janssen effect leading to versatile control of the apparent mass of a ferromagnetic granular column. Beyond such remarkable static properties, being able to finely tune the apparent mass of a granular column opens an appealing perspective towards novel dynamical properties, with for instance the control of the discharge of silos. Finally, we note that our study can be extended to the case of composite granular media (where only a fraction of the grains are ferromagnetic) with an even broader range of possible applications.

Methods

The setup shown in Fig. 1 consists of a copper tube of 19.57 mm internal diameter filled with steel beads of radius $a = 0.75$ mm and density $\rho = 8000\,\mathrm{kg\,m^{-3}}$. The beads lay on a Polytetrafluoroethylene (PTFE) piston of diameter 18.30 mm carefully aligned with the tube to ensure no contact with its walls. The piston is attached to a force sensor which can measure the apparent mass of the packing with a precision of ±0.10 g. We followed the protocol described in[11,38] to fully mobilize the frictional forces along the tube: the piston is mounted on a vertical translation stage displacing the beads assembly downwards over a distance $\Delta h = 7$ mm at a velocity $v = 0.2\,\mathrm{mm\,s^{-1}}$, see Supplementary Materials for more details. The packing apparent mass is then obtained by measuring its mean value during the displacement, while the standard deviation around this value reflects the typical measurement dispersion. We placed the whole setup between two magnetic coils in a Helmholtz configuration, creating a uniform magnetic field, either vertical or horizontal depending on the respective orientation of the coils. The magnetic field is turned on and applied to the granular column, right after the packing preparation, just before its mass measurement. With this setup, we can reach a maximum external magnetic field of $B_{\mathrm{max}} \approx 170$ G, leading to the dimensionless number $\Psi \approx 35$. The inner diameter of our magnetic coils (20 cm) sets the maximum height of the granular column, for which the applied field can be considered uniform, to $h_{\mathrm{max}} = 10\,\mathrm{cm}$, which corresponds to a mass around 150 g. For a uniform magnetic field, the individual induced dipolar moments $\mathbf{d}$ can be considered identical for all beads and aligned with the direction of the field.

Data availability

The data that support the findings of this study are available from the corresponding author upon reasonable request.

Code availability

The code used for discrete particle simulations is the open-source package MercuryDPM[36].

Received: 1 December 2020; Accepted: 22 March 2021;
Published online: 30 April 2021

References

1. FAO. *Crop prospects and food situation #3, September 2020* (FAO, 2020).
2. de Gennes, P. Reflections on the mechanics of granular matter. *Phys. A Stat. Mech. Appl.* **261**, 267–293 (1998).
3. Duran, J. *Sands, powders, and grains : an introduction to the physics of granular materials* (Springer, 2000).
4. Jaeger, H. M. & Nagel, S. R. Physics of the granular state. *Science* **255**, 1523–1531 (1992).
5. de Gennes, P. G. Granular matter: a tentative view. *Rev. Modern Phys.* **71**, S374–S382 (1999).
6. Andreotti, B., Forterre, Y. & Pouliquen, O. *Granular Media: Between Fluid and Solid* (Cambridge University Press, 2013).
7. Bi, D., Zhang, J., Chakraborty, B. & Behringer, R. P. Jamming by shear. *Nature* **480**, 355–358 (2011).
8. Liu, A. J. & Nagel, S. R. Jamming is not just cool any more. *Nature* 396, 21–22 (1998).
9. Cates, M. E., Wittmer, J. P., Bouchaud, J.-P. & Claudin, P. Jamming, force chains, and fragile matter. *Phys. Rev. Lett.* **81**, 1841–1844 (1998).
10. Janssen, H. A. Investigations of pressure of grain in silo. *Vereins Eutscher Ingenieure Zeitschrift* **39**, 1045–1049 (1895).
11. Vanel, L. & Clément, E. Pressure screening and fluctuations at the bottom of a granular column. *Eur. Phys. J. B* **11**, 525–533 (1999).
12. Vanel, L. et al. Stresses in silos: comparison between theoretical models and new experiments. *Phys. Rev. Lett.* **84**, 1439–1442 (2000).
13. Bratberg, I., Måløy, K. J. & Hansen, A. Validity of the Janssen law in narrow granular columns. *Eur. Phys. J. E* **18**, 245–252 (2005).
14. Bouchaud, J.-P., Cates, M. E. & Claudin, P. Stress distribution in granular media and nonlinear wave equation. *J. de Phys. I* **5**, 639–656 (1995).
15. Anthony, J. L. & Marone, C. Influence of particle characteristics on granular friction. *J. Geophys. Res.* **110**, B08409 (2005).
16. Baxter, G. W., Behringer, R. P., Fagert, T. & Johnson, G. A. Pattern formation in flowing sand. *Phys. Rev. Lett.* **62**, 2825–2828 (1989).
17. Hornbaker, D. J., Albert, R., Albert, I., Barabási, A.-L. & Schiffer, P. What keeps sandcastles standing? *Nature* **387**, 765–765 (1997).
18. Bocquet, L., Charlaix, E., Ciliberto, S. & Crassous, J. Moisture-induced ageing in granular media and the kinetics of capillary condensation. *Nature* **396**, 735–737 (1998).
19. Nowak, S., Samadani, A. & Kudrolli, A. Maximum angle of stability of a wet granular pile. *Nat. Phys.* **1**, 50–52 (2005).
20. Scheel, M. et al. Morphological clues to wet granular pile stability. *Nat. Mater.* **7**, 189–193 (2008).
21. Tapia, F., Santucci, S. & Géminard, J.-C. Fracture reveals clustering in cohesive granular matter. *EPL Europhys. Lett.* **115**, 64001 (2016).

22. Waitukaitis, S. R., Lee, V., Pierson, J. M., Forman, S. L. & Jaeger, H. M. Size-dependent same-material tribocharging in insulating grains. *Phys. Rev. Lett.***112**, 218001 (2014).
23. Schella, A., Herminghaus, S. & Schröter, M. Influence of humidity on tribo-electric charging and segregation in shaken granular media. *Soft Matter* **13**, 394–401 (2017).
24. Forsyth, A. J., Hutton, S. R., Rhodes, M. J. & Osborne, C. F. Effect of applied interparticle force on the static and dynamic angles of repose of spherical granular material. *Phys. Rev. E* **63**, 031302 (2001).
25. Taylor, K., King, P. J. & Swift, M. R. Influence of magnetic cohesion on the stability of granular slopes. *Phys. Rev. E* **78**, 031304 (2008).
26. Lumay, G. & Vandewalle, N. Tunable random packings. *N. J. Phys.* **9**, 406–406 (2007).
27. Lumay, G. & Vandewalle, N. Controlled flow of smart powders. *Phys. Rev. E* **78**, 061302 (2008).
28. Lumay, G., Vandewalle, N., Nakagawa, M. & Luding, S. Packing fraction and compaction dynamics of magnetic powders. In *AIP Conference Proceedings* (AIP, 2009).
29. Vandewalle, N., Lumay, G., Nakagawa, M. & Luding, S. Flow properties and heap shape of magnetic powders. In *AIP Conference Proceedings* (AIP, 2009).
30. Edwards, B. F. & Edwards, J. M. Dynamical interactions between two uniformly magnetized spheres. *Eur. J. Phys.* **38**, 015205 (2016).
31. Bai, K. et al. Effective magnetic susceptibility of suspensions of ferromagnetic particles. *J. Appl. Phys.* **124**, 123901 (2018).
32. Vessaire, J., Plihon, N., Volk, R. & Bourgoin, M. Sedimentation of a suspension of paramagnetic particles in an external magnetic field. *Phys. Rev. E* **102**, 023101 (2020).
33. Mahajan, S. et al. Reverse janssen effect in narrow granular columns. *Phys. Rev. Lett.***124**, 128002 (2020).
34. Shaxby, J. H., Evans, J. C. & Jones, V. On the properties of powders. the variation of pressure with depth in columns of powders. *Trans. Faraday Soc.* **19**, 60 (1923).
35. Peralta, J. P., Aguirre, M. A., Géminard, J.-C. & Pugnaloni, L. A. Apparent mass during silo discharge: nonlinear effects related to filling protocols. *Powder Technol.* **311**, 265–272 (2017).
36. Weinhart, T. et al. Fast, flexible particle simulations — an introduction to MercuryDPM. *Comput. Phys. Commun.* **249**, 107129 (2020).
37. Landry, J. W., Grest, G. S., Silbert, L. E. & Plimpton, S. J. Confined granular packings: structure, stress, and forces. *Phys. Rev. E* **67**, 041303 (2003).
38. Bertho, Y., Giorgiutti-Dauphiné, F. & Hulin, J.-P. Dynamical janssen effect on granular packing with moving walls. *Phys. Rev. Lett.* **90**, 144301 (2003).

Acknowledgements

We thank L. Vanel, J-C. Géminard, and N. Taberlet for enlightening discussions. We thank the Research Council of Norway through its Centre of Excellence funding scheme, project number 262644, the support of ENS de Lyon, and of the CNRS, through the French-Norwegian IRP, (D-FFRACT). S.S. acknowledges also the support of the Russian Government with grant no. 14.W03.31.0002.

Author contributions

All authors significantly contributed to this work as a team effort. S.S. and M.B. designed the study. L.T. performed the experiments and the theoretical analysis, supervised by S.S., M.B. and K.J.M.. S.S. and L.T. wrote the first draft of the manuscript. All authors read critically and participate to the writing of the manuscript.

Competing interests

The authors declare no competing interests.

Additional information

Supplementary information The online version contains supplementary material available at https://doi.org/10.1038/s41467-021-22722-y.

Correspondence and requests for materials should be addressed to S.S.

Peer review information *Nature Communications* thanks Massimo Pica Ciamarra and the other, anonymous, reviewer(s) for their contribution to the peer review of this work. Peer reviewer reports are available.

Reprints and permission information is available at http://www.nature.com/reprints

Publisher's note Springer Nature remains neutral with regard to jurisdictional claims in published maps and institutional affiliations.

Taming the Janssen effect

Louison Thorens[1,2,*], *Knut Jørgen* Måløy[2], *Mickaël* Bourgoin[1], and *Stéphane* Santucci[1,3]

[1]Univ Lyon, ENS de Lyon, Univ Claude Bernard, CNRS, Laboratoire de Physique, F-69342 Lyon, France
[2]PoreLab, The Njord Centre, Department of Physics, University of Oslo, P. O. Box 1048 Blindern, N-0316 Oslo, Norway
[3]Lavrentyev Institute of Hydrodynamics, Siberian Branch of the Russian Academy of Sciences, Novosibirsk, Russia

Abstract. We investigate both experimentally and theoretically the apparent mass of a ferromagnetic granular assembly filling a cylindrical container and submitted to a magnetic field **B**, aligned vertically along the silo. We show that the mass of the ferromagnetic granular column depends strongly on the applied magnetic field. Notably, our measurements deviate strongly from the exponential saturation of the measured mass as a function of the true mass of the grain packing, as predicted by Janssen [H.A. Janssen, Vereins Eutscher Ingenieure Zeitschrift, 1045 (1895)]. In particular, the measured mass of tall columns decreases systematically as the amplitude of the magnetic field increases. We rationalize our experimental findings by considering the induced magnetic dipole-dipole interactions within the whole packing. We show the emergence of a global magnetic radial force along the walls of the silos, fully determined by the external magnetic field. The resulting tunable frictional interactions allows a full control of the effective mass of the ferromagnetic granular column.

1 Introduction

More than hundred years ago, a German engineer H.A Janssen studying the failure of silos, proposed a phenomenological model to describe the saturation of the pressure measured at the bottom of a container filled with grains [1]. Indeed, the pressure exerted at the bottom of a silo does not follow the hydrostatic formula $\sigma = \rho g h$ where ρ is the average density of the medium and h the column height, but saturates. Janssen's approach of this problem is simple but transcript nicely the experimental measurements. It can be resumed as follow: (i) the grain assembly is considered as a continuous medium with a homogeneous vertical stress σ_z along a tube section, (ii) within the grains packing, the vertical stress is redistributed in the horizontal direction following the proportional law: $\sigma_r = K\sigma_z$, with a phenomenological constant K, (iii) the frictional contact forces F_z between the grains and the cylinder wall are at the Coulomb limit $F_z = \mu F_r$, with μ the friction coefficient. Using these three hypothesis on a column slice, Janssen could demonstrate that the apparent mass measured at the base of the silo saturates exponentially, $m_J = m_\infty[1 - \exp(-m_0/m_\infty)]$ characterized by the saturation mass $m_\infty = (\rho\pi R^3)/(2K\mu)$, with R the tube radius. During the last decades this simple approach has been criticized and refined [2–7], but it remains a classical result nowadays, the so-called, Janssen effect. In fact, when dealing with this static configuration of grains at rest in a tube, the main issue resides in the measure of the stresses since a granular system at rest is extremely responsive to perturbation and its preparation [8]. To measure the apparent mass at the bottom of the system, [9] proposed an experimental protocol to ensure that the friction forces are fully mobilized in the vertical direction. Nevertheless the Janssen effect is ultimately hardly controllable. Here, we propose to use ferromagnetic grains which, when submitted to an external magnetic field, acquire a magnetic moment leading to tunable pair interactions inside the granular medium. The possibility to modify and control in-situ with an external parameter the particles interactions within the packing constitutes a great advantage, in stark contrast with other means, such as the use of different particles (with different shapes and roughness) [10, 11], modifying the environment humidity (leading to capillary bridges) or triboelectric charge effects [12–14], which are all barely tunable.

2 Experiments

A sketch of our experimental setup is shown in figure 1a. This setup is composed of a copper tube of 19.6 mm radius filled with monodisperse 0.75 mm radius steel grains laying on a 19.0 mm radius piston fixed to a force gauge. The sensor is also mounted on a motorized vertical translation stage moving downward. The whole setup is placed between two coils mounted in a Helmholtz configuration, generating a uniform magnetic field **B** in the vertical direction as shown in figure 1b.

To quantify the effect of the magnetic interaction, we can consider the dimensionless number Ψ, (sometimes referred as a magnetic Bond number [15, 16]), which compares magnetic pair interaction and gravity, $\Psi = (\chi_m B)^2/(\mu_0 a\rho g)$ where χ_m is the magnetic susceptibility of the beads equal to 3 in the case of a random close packing [17], μ_0 is the magnetic permeability of vacuum, a the

*e-mail: louison.thorens@ens-lyon.fr

A video is available at https://doi.org/10.48448/2292-nz67

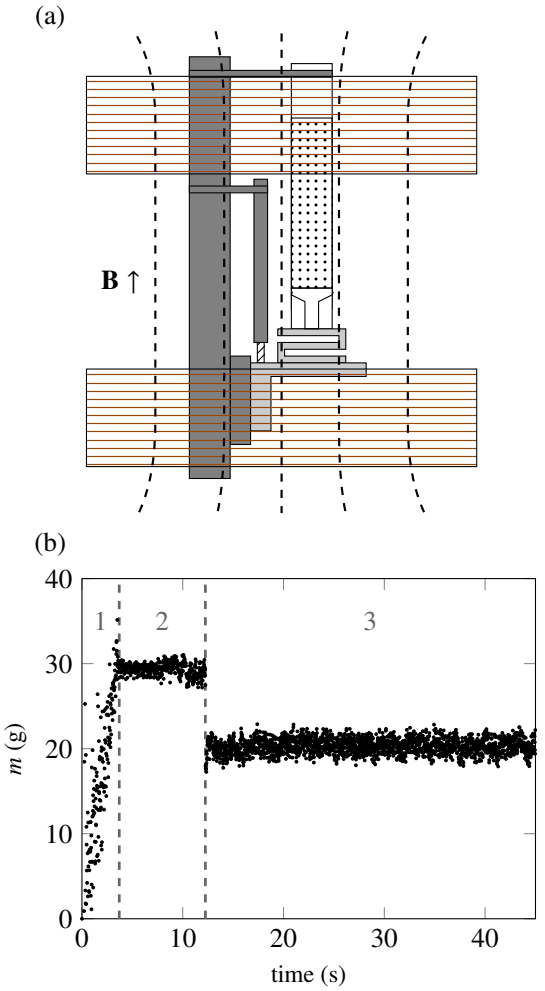

Figure 1. (a) Sketch of the experimental set-up with the generation of a homogeneous vertical magnetic field, using coils in a Helmholtz configuration. (b) Typical mass measurement, 1. beads are poured inside a tube using a hopper until we reach the desired mass m0, 2. the packing is at rest and the hopper is removed, 3. downward movement of the vertical translation stage, the mass measurement corresponds to the mean plateau value.

bead radius, ρ the bead density. In our case, due to the limitation of the power supply used, the maximum reachable value is $\Psi = 35$ corresponding to a magnetic field $B = 170\,\mathrm{G}$.

Figure 1b gives a typical mass measurement using our system. Our protocol is the following: the grains are poured inside the tube using a funnel until reaching the desired packing mass m_0. Then the funnel is removed and the magnetic field turned on. The vertical translation stage moves downward at a constant velocity $v = 0.2\,\mathrm{mm\,s^{-1}}$ over a distance of $\Delta h \simeq 7\,\mathrm{cm}$, following the protocol proposed by [9], releasing the spring compression loaded in the mass sensor, leading to a lower apparent mass. The mass reaches a plateau during the descent where the mean value corresponds to our mass measurement m and the standard deviation gives the typical dispersion of our measurement. Finally, when the stage stops, the mass sensor is compressed again and the apparent mass is slightly higher than the mean plateau value.

We used this experimental protocol to measure the apparent mass of the grain column for different packing mass m_0 and field amplitude Ψ. The results are shown in figure 2a. First, without magnetic field, $\Psi = 0$, the measured mass of the granular column is in very good agreement with Janssen's prediction, following an exponential saturation with a characteristic mass $m_\infty = 42\,\mathrm{g}$. Nevertheless, as soon as the ferromagnetic granular column is submitted to an external magnetic field, we observe a strong deviation from Janssen's prediction. Specifically, when increasing the amplitude of the magnetic field, we clearly see that for a high enough packing mass $m_0 > 40\,\mathrm{g}$, the higher the magnetic field, the lower the apparent mass. The even more striking effect is clearly seen for the highest amplitude of the magnetic field used, corresponding to $\Psi = 35$, for which from a certain packing mass $m_0 \approx 70\,\mathrm{g}$, the apparent mass of the packing decreases with the actual mass of the packing m_0: the more added grains, the lower the apparent mass! Pushing the limits of our experimental setup, using a very tall column corresponding to a mass $m0 = 190\,\mathrm{g}$ where the magnetic field is not as homogeneous, we could measure that the apparent mass became null for the highest amplitude of the magnetic field applied. Indeed, in such conditions, the grain assembly was stuck inside the tube, its wall supporting completely the weight of the granular column. To emphasize such deviations to the prediction of Janssen, we show on figure 2b the difference between the apparent mass m and the Janssen classical prediction m_J shown in figure 2b. For low packing mass $m_0 < 40\,\mathrm{g}$, the apparent mass is slightly higher than the Janssen prediction, while for higher packing mass the measure is always lower than the classical prediction and seems to follow a linear slope ($m_0 > 40\,\mathrm{g}$) which decreases systematically with the magnetic field amplitude.

3 Model

Ferromagnetic grains under a uniform vertical magnetic field acquire a vertical magnetic moment $\mathbf{d}$ directly proportional to the magnetic field via the magnetic susceptibility, $\mathbf{d} = V\chi_m\mathbf{B}/\mu_0$. Each particle i of the packing will interact with a particle j with the following magnetic dipole-dipole interactions [18]:

$$\mathbf{f_{ij}} = \frac{3\mu_0}{4\pi r_{ij}^5}\left(d^2\left(1-5\cos^2\alpha\right)\mathbf{r_{ij}} + 2dr_{ij}\mathbf{d}\cos\alpha\right), \qquad (1)$$

where α is the angle between the magnetic field and the beads distance vector $\mathbf{r}_{ij}$. Figure 3a gives a representation of the magnetic interaction either repulsive or attractive depending on the relative position of the particles i and j ($\mathbf{r_{ij}}$), and the applied magnetic field $\mathbf{B}$, characterized by the angle α. Therefore, a particle i of the packing will be subjected to multiple interactions from its neighbours following each time the expression above. The resulting magnetic force will be the sum of all magnetic dipole-dipole interactions $f_i = \sum_j f_{ij}$.

We can first discuss those local magnetic forces f_i, within the granular packing. Because of the cylindrical symmetry

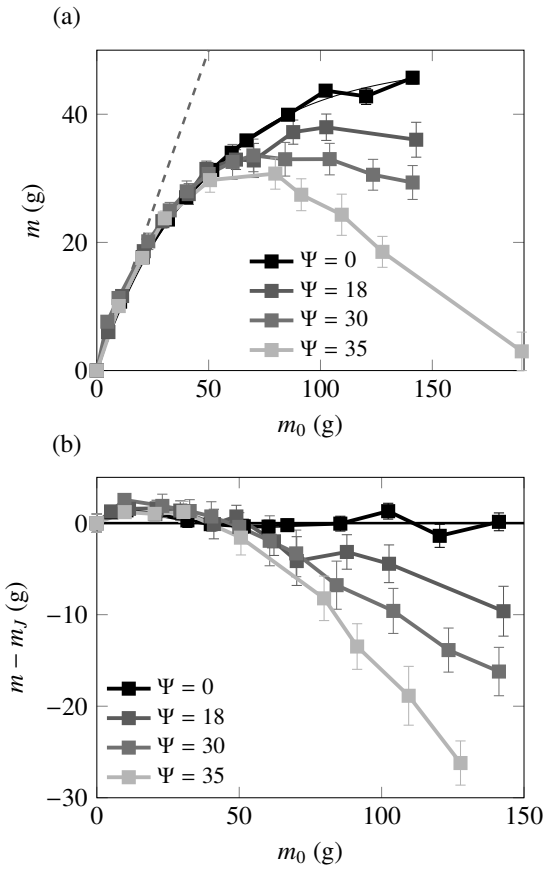

Figure 2. (a) Apparent mass measured using our experimental setup for different magnetic field amplitude, the black continuous line corresponds to the Janssen model m_J and the grey dashed line represents the hydrostatic limit. (b) Mass difference between the apparent mass of the system and the Janssen expression m_J for different magnetic field amplitude.

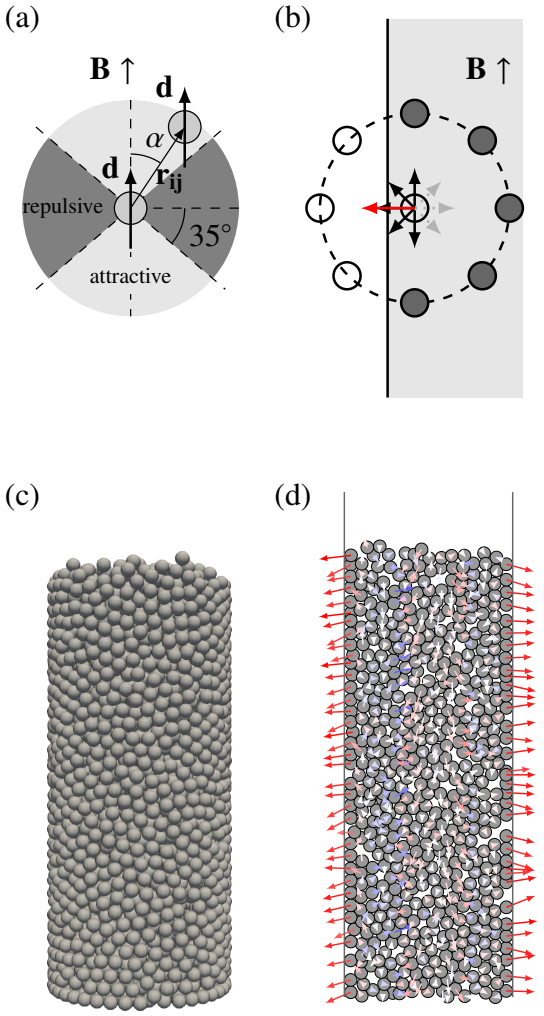

Figure 3. (a) Ferromagnetic dipolar interaction for a vertical magnetic field, either repulsive or attractive depending on the relative position of the particles and the applied magnetic field, quantified by the angle α. (b) Forces acting on an off-axis particle. (c) Random close packing generation using DPM simulations. (d) Forces representations inside a tube layer, averaged along θ, for a vertical magnetic field where red (resp. blue) vectors represents positive (resp. negative) radial components.

of the column, and the mirror symmetry with respect to the mid-plane at $z = h/2$, the magnetic interactions do not add any global azimuthal nor vertical forces on the packing. Thus, the only net force that will not average to zero within the column, is the radial component f^r. The figure 3b describes schematically this effect, which arises because of the finite-size of the silo, and the non-compensation of some interactions due to missing particles (displayed in white). It is important to remark also that we can expect this effect to be maximal along the walls of the container.
To verify these considerations, we generated 3D random close packing using Discrete Element Method simulations [19]. We followed the numerical protocol the filling protocol proposed by [20] where the particles are randomly placed on a disk at constant height above the sedimented packing. This simulation method allowed us to generate packings of filling fraction $\phi \approx 0.6$, as shown in figure 3c. Using the positions of the beads thus generated, we computed all the magnetic pair interactions using eq. (1). Thus, we could obtain the magnetic force exerted on each particle inside the packing. We could obtain the magnetic force exerted for a packing vertical slice in figure 3d, with vectors in red (resp. blue) for a positive (resp. negative) radial component f^r. We clearly see that the forces are mainly situated along the tube wall and pushing against it while they rapidly decrease to zero in the packing core. Moreover, we can notice that those radial repulsive forces emerging at the walls of the silos appear constant.

To express the impact of the magnetic forces on the apparent mass at the tube base, we consider the ferromagnetic grain assembly as a whole. Therefore, we no longer consider the local individual forces, but the global net force exerted on the wall $F^r = \sum_i f_i^r$. We noticed that the local forces, in the case of a vertical magnetic field, are mainly pushing against the wall ; thus, we expect a positive global radial force. Moreover, if we consider Janssen's hypothesis that the friction forces are fully mobilized in the vertical direction, this global magnetic radial force can provide a global vertical contribution to the pressure measured at the bottom of the silo : $F = -\mu F^r$. The final

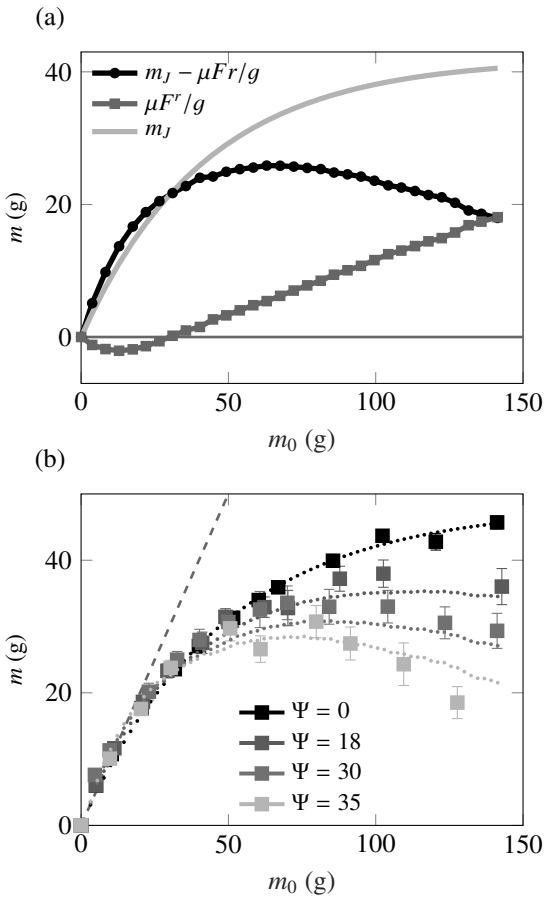

Figure 4. (a) Model curves for a vertical magnetic field. The light grey line shows the classical Janssen prediction; the grey squares line is the result of the computed magnetic mass loss $\mu F^r/g$; the black circles line (difference of both curves) gives the predicted apparent mass of the column. (b) Comparison of the model to the experimental data points.

apparent mass is then given by the Janssen approach from which we subtract the magnetic friction contribution:

$$m = m_J - \mu F^r/g, \tag{2}$$

where the friction coefficient μ is equal to 0.4 in our experiments. The global picture of the numerical resolution is given in figure 4 where we show the Janssen contribution m_J, the global radial force F^r computed using the local forces f_i for different packing height h, and the final result of eq. 2. The radial force is slightly negative for low mass $m_0 < 30\,\mathrm{g}$ and follow a linear tendency for higher mass. The final shape was compared with the experimental results for different field intensity and was found in good accordance as shown in figure 4b.

To conclude, we have described a "magnetic Janssen effect" [21], which allows to control the apparent mass of a ferromagnetic granular column. Such ability to finely tune frictional interactions thanks to an external controlling parameter opens appealing perspectives beyond such a static behaviour, with novel dynamical properties involved for instance in the discharge of silos [15, 22].

References

[1] H.A. Janssen, Vereins Eutscher Ingenieure Zeitschrift **39**, 1045 (1895)
[2] L. Vanel, E. Clément, Eur. Phys. J. B **11**, 525 (1999)
[3] L. Vanel, P. Claudin, J.P. Bouchaud, M.E. Cates, E. Clément, J.P. Wittme, Phys. Rev. Lett. **84**, 1439 (2000)
[4] P.G. de Gennes, Rev. Mod. Phys. **71**, S374 (1999)
[5] M.E. Cates, J.P. Wittmer, J.P. Bouchaud, P. Claudin, Phys. Rev. Lett. **81**, 1841 (1998)
[6] I. Bratberg, K.J. Måløy, A. Hansen, Eur. Phys. J. E **18**, 245 (2005)
[7] J.P. Bouchaud, M.E. Cates, P. Claudin, J. Phys-Paris I **5**, 639 (1995)
[8] B. Andreotti, Y. Forterre, O. Pouliquen, *Granular media: between fluid and solid* (Cambridge University Press, Cambridge, 2013), 86
[9] G. Ovarlez, C. Fond, E. Clément, Phys. Rev. E **67**, 060302(R) (2003)
[10] J.L. Anthony, C. Marone, J. Geophys. Res. **110**, B08409 (2005)
[11] G.W. Baxter, R.P. Behringer, T. Fagert, G.A. Johnson, Phys. Rev. Lett. **62**, 2825 (1989)
[12] D.J. Hornbaker, R. Albert, I. Albert, A.L. Barabási, P. Schiffer, Nature **387**, 765 (1997)
[13] M. Scheel, R. Seemann, M. Brinkmann, M.D. Michiel, A. Sheppard, B. Breidenbach, S. Herminghaus, Nature Materials **7**, 189 (2008)
[14] F. Tapia, S. Santucci, J.C. Géminard, EPL-Europhys. Lett. **115**, 64001 (2016)
[15] G. Lumay, N. Vandewalle, Phys. Rev. E **78**, 061302 (2008)
[16] J. Vessaire, N. Plihon, R. Volk, M. Bourgoin, Phys. Rev. E **102**, 023101 (2020)
[17] K. Bai, J. Casara, A. Nair-Kanneganti, A. Wahl, F. Carle, E. Brown, JPN J. Appl. Phys. **124**, 123901 (2018)
[18] B.F. Edwards, J.M. Edwards, Eur. Phys. J **38**, 015205 (2016)
[19] T. Weinhart, L. Orefice, M. Post, M.P. van Schrojenstein Lantman, I.F. Denissen, D.R. Tunuguntla, J. Tsang, H. Cheng, M.Y. Shaheen, H. Shi et al., Comput. Phys. Commun. **249**, 107129 (2020)
[20] J.W. Landry, G.S. Grest, L.E. Silbert, S.J. Plimpton, Phys. Rev. E **67**, 041309 (2003)
[21] L. Thorens, K.J. Måløy, M. Bourgoin, S. Santucci, Nat. Commun. in press (2021)
[22] L. Thorens, K.J. Måløy, M. Bourgoin, S. Santucci, EPJ Web Conf. this volume (2021)

Magnetic Janssen Effect in hybrid granular media

L. Thorens[1,2], K. J. Måløy[2], M. Bourgoin[1], S. Santucci[1,3]
[1] *Univ Lyon, ENS de Lyon, Univ Claude Bernard, CNRS, Laboratoire de Physique, F-69342 Lyon, France*
[2] *PoreLab, The Njord Centre, Department of Physics, University of Oslo, P. O. Box 1048 Blindern, N-0316 Oslo, Norway and*
[3] *Lavrentyev Institute of Hydrodynamics, Siberian Branch of the Russian Academy of Sciences, Novosibirsk, Russia*
(Dated: August 10, 2021)

Granular media are widely involved in a large variety of industrial and natural systems, displaying exceptional behaviours. The Janssen effect, describing the pressure screening at the bottom of a granular column, is one of the most famous ones. The classical description reports that a part of the grains weight is supported by the walls of the tube via a complex network of mechanical frictional contacts. Recently, we reported that the use of ferromagnetic grains can lead to the presence of a magnetic Janssen effect, where the contact forces can be remotely driven. Here, we propose to investigate the magnetic Janssen effect in a hybrid granular assembly made of both ferromagnetic and non-ferromagnetic grains. Moreover, we show that both the amount of ferromagnetic particles and their distribution inside the packing have a clear impact on the apparent mass of the granular column.

Granular media, commonly seen in a variety of engineering and environmental systems, remain at the heart of an active field of research. The singularity of their physics leads to a large variety of unique behaviours, where grains can behave both as solid or liquid depending on the applied conditions. A fundamental problem of granular mechanics certainly is their storage in a confined geometry, also known as the Janssen effect [1], and first described by the German engineer who gave it his name. A column of grains filling a tube does not appear as heavy as it really is. In fact, for a granular column taller than its diameter, the bottom pressure saturates, meaning that part of the mechanical stress is applied on the tube walls. To quantify this effect, Janssen relied on three strong assumptions: (i) the granular assembly is considered homogeneous; (ii) inside the packing, the vertical stresses are partially redirected horizontally along the walls following the proportionality law $\sigma_r = K\sigma_z$, where K is the phenomenological Janssen constant; (iii) the friction forces between the grains and the wall are fully mobilized $F_z = \mu F_r$, with μ the friction coefficient. These three assumptions lead to the following expression for the apparent mass at the bottom of a granular column:

$$m_J = m_\infty^0 \left[1 - \exp(-m_0/m_\infty^0)\right], \tag{1}$$

where m_0 is the actual packing mass and m_∞^0 is the saturation mass depending on the considered geometry. Even though Janssen's model has been refined since, it remains a robust description of grains storage in a confined geometry.

Recently, we proposed to test Janssen prediction on a granular column filled with ferromagnetic particles, surrounded by an homogenous magnetic field $\mathbf{B}_0$ [2]. The easily tunable interactions between ferromagnetic grains leads to an external control of the force inside the packing and therefore a control of its apparent mass. We showed that the effective mass of a column of ferromagnetic grains could indeed be magnetically controlled, increasing or decreasing the classical Janssen effect, with a remarkable "*more is the less*" behaviour where, for a sufficiently large vertical applied field, the apparent mass of the column would decrease as grains are added, up to the point where it strictly vanishes. A simple model, accounting for the magnetic interactions and their symmetry breaking due to the confinement of the grains was derived, showing excellent agreement with experiments.

In this letter, we extend the observation and the modelling of this *magnetic Janssen effect* to the more general case of hybrid granular media, composed of a mixture of both ferromagnetic and non-ferromagnetic grains. We show that both the amount of ferromagnetic particles and their distribution inside the packing lead to a control of the apparent mass of the granular column.

While their potential for applications is far more relevant than the case of entirely ferromagnetic granular systems (ferromagnetic grains represent indeed only a small portion of the large variety of existing granular media), hybrid granular media remain scarcely studied. One exception is the study of the compaction (by tapping) of a mixed steel-and-glass grains packing [3, 4], showing a continuous increase of the compaction time as the volume fraction of magnetic grains and/or the amplitude of the magnetic field increases, hence paving the way towards the discovery of new magnetically tunable granular physics with potential impact on the broad range of applications in the context of cohesive powders industry.

Magnetic grains are characterized by the magnetic susceptibility of their material χ, significantly greater than one, linking the external magnetic field $\mathbf{B}_0$ and the dipolar moment of a grain of volume V: $\mathbf{d} = V\chi\mathbf{B}_0/\mu_0$, with μ_0 the magnetic permeability of vacuum. In the case of a granular packing of ferromagnetic spheres, the magnetic susceptibility saturates at a value of $\chi_m = 3$ [5] (even if the susceptibility of the bulk material can be significantly larger), due to demagnetization fields. Since each bead inside the packing acquires a dipolar moment $\mathbf{d}$, each pair of grains i and j will

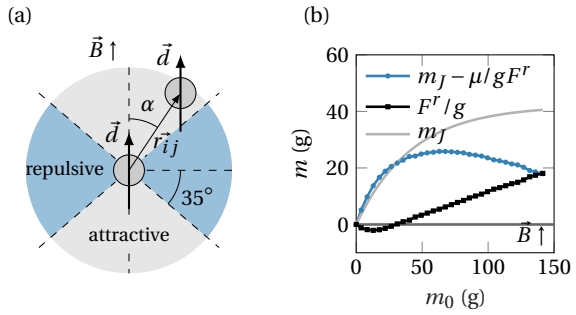

Figure 1. Magnetic Janssen effet. (a) Magnetic pair interaction between two ferromagnetic beads characterized by the magnetic moment **d**. The interaction can be either repulsive of attractive depending on the angle between the two beads α. (b) Apparent mass of the magnetic Janssen prediction for a vertical magnetic field.

interact following the dipole-dipole interaction force:

$$\mathbf{f_{ij}} = \frac{3\mu_0}{4\pi r_{ij}^5}\left(d^2\left(1-5\cos^2\alpha\right)\mathbf{r_{ij}} + 2d r_{ij}\mathbf{d}\cos\alpha\right), \qquad (2)$$

where α is the angle between the applied magnetic field and the separation vector between the two grains $\mathbf{r_{ij}}$ as shown in figure 1a and $d = |\mathbf{d}|$. We assume here that the dipolar momenta of the two grains i and j are equal ($\mathbf{d}_i = \mathbf{d}_j = \mathbf{d}$), what holds for a homogeneous magnetic field. I can be seen from eq. 2 that the interaction can be either repulsive or attractive depending on the value of α : it is attractive when particles tend to be aligned, while it is repulsive when grains are side by side (see Fig. 1a).

Within this context we have previously shown that both the dipolar property of the magnetic interaction force and the particular confined geometry of a tube lead to the existence of a tunable –enhanced or hindered– "magnetic Janssen effect" of a ferromagnetic packing with the following expression for the new apparent mass:

$$m = m_J - \frac{\mu}{g}F^r(m_0, B_0), \qquad (3)$$

where F^r is the global radial force resulting from the magnetic pair interactions applied on the tube walls. F^r can be estimated using expression (2) on a simulated 3D random close packing, for any given value of the actual packing m_0 (or height h) and of the magnetic field amplitude B_0. The corresponding magnetic Janssen prediction (in excellent agreement with experiments [2]) for a vertical applied magnetic field and for a packing entirely composed of ferromagnetic particles is recalled in figure 1b. It can be seen that for a small columns, the magnetic contribution leads to an apparent mass exceeding the classical Janssen mass (reminiscent of an inverse Janssen effect [6]) while for large columns the magnetic contribution significantly reduces the apparent mass which eventually becomes a decreasing function of the actual mass. Here, we explore how this scenario of the magnetic Janssen effect is affected when

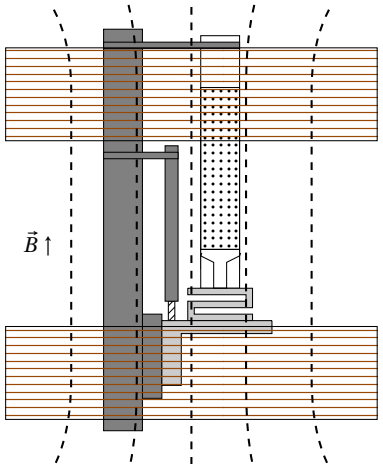

Figure 2. Experiment set-up where a tube filled with ferromagnetic beads lays on a mass sensor fixed on vertical translation stage with a magnetic field generated using Helmholtz coils either in vertical configuration.

only a fraction of the grains is ferromagnetic. This generalises the previous study by accounting for the dependency of the magnetic Janssen effect on the mass fraction ϕ_m of ferromagnetic grains.

To characterise the Janssen effect experimentally, we measure the apparent mass of a column of grains. The figure 2a gives a representation of the experimental setup, composed of a copper tube of diameter 19.6 mm, mounted on a piston of diameter 19.0 mm filled with $a = 0.75$ mm radius grains. The piston is slightly smaller than the tube to ensure that the mass we measure is only the packing one, but large enough so that no bead can fall out. The piston is fixed on a mass sensor (Testwell KD40S-100N) attached to a vertical translation stage as proposed by [7] to fully mobilise vertically the frictional forces along the tube wall to verify Janssen assumption (iii). The whole system is then placed between two coils in a vertical Helmholtz configuration, generating a uniform vertical magnetic field within a length scale of 10 cm setting a maximum limit for the packing height $h \approx 10$ cm. To ensure no history of the magnetic grains between each measurement (remanence), we demagnetised the grains before pouring inside the tube following the hysteresis protocol given in [8]: the beads are placed in an 100% amplitude-modulated 20 Hz sinusoidal signal which amplitude is then decreased to zero. The beads are first poured inside the tube using a funnel until we reach a desired mass m_0, the funnel is then removed and the magnetic field turned on before moving the piston downward at a constant velocity $v = 0.2\,\mathrm{mm\,s^{-1}}$ over a distance of $\Delta h \simeq 7$ mm. The apparent mass of the packing is taken as the mean mass over the descent and the measurement error as the standard deviation.

In this study, the experiments were performed using a mixture of ferromagnetic and non-ferromagnetic grains

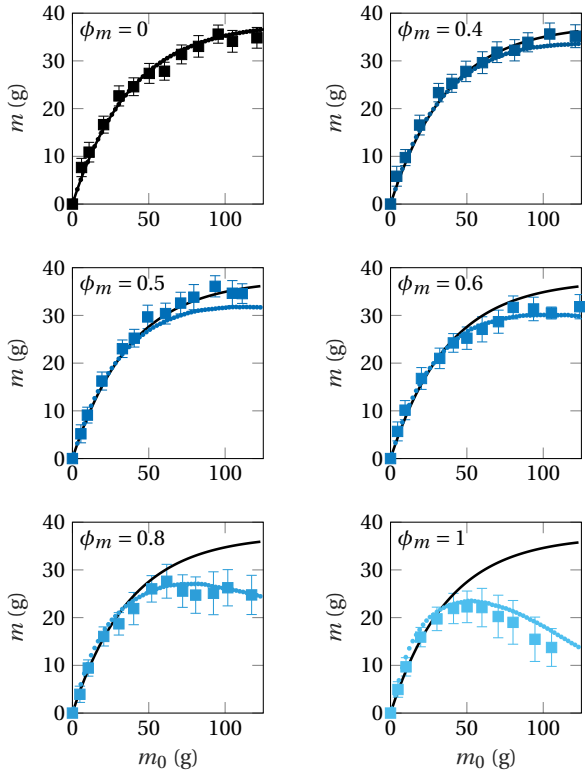

Figure 3. Mass measurement of the beads for a vertical magnetic field B = 170 G and varying the magnetic fraction of the packing ϕ_m. The colour squares are the experimental data, the black line represents the classical Janssen prediction while the colour dots represent the computed model. The experiments follow the Janssen prediction until $\phi_m \approx 0.5$ where they switch to the magnetic Janssen model.

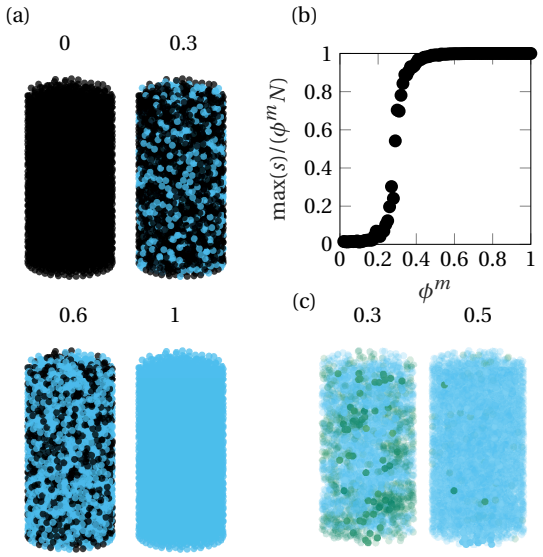

Figure 4. Magnetic Janssen effect of a randomly mixed ferromagnetic distribution. (a) Representation of the mixed packing used for the numerical resolution, where black (respectively blue) beads represent are non-ferromagnetic (respectively ferromagnetic). (b) Maximum ferromagnetic cluster size normalised by the total number of ferromagnetic particles. (c) Clusters visualisation where the biggest cluster is shown in blue while smaller clusters are shown in green, non-ferromagnetic particles are not displayed.

at the desired ferromagnetic concentration $\phi_m = N^m/N$, where N^m and N are respectively the number of ferromagnetic particles and total number of particles inside the packing. In order to avoid unwanted segregation due to any eventual density difference between the two classes of grains, what would jeopardise the realisation of a truly random mixed packing [9, 10], we use a mixture of steel beads, with identical size (1.50 mm diameter) and density, and only varying with respect to their magnetic properties. The ferromagnetic beads are made of 100C6 steel while the non magnetic are made of 316-L steel. The density difference between these materials is about 2%.

In parallel to experiments, we adapted the model solution of the magnetic Janssen effect [2] using the packing generation and the pair interactions resolution keeping the magnetic field constant to B_0 = 170 G but only varying the amount N^m of ferromagnetic particles. To do so, we selected for each value of ϕ_m a random list of N^m grains inside the packing and computed the pair dipole-dipole magnetic interactions only on this limited random collection of positions inside the packing as shown in figure 4a. To avoid any bias on the final result that could be induced by the random process, we averaged the computation of the total radial force F^r on series of 10 independent random realisations for each value of ϕ_m.

The results and comparison between the model and the experiments are shown in figure 3. As one can expect, the lower the amount of ferromagnetic particles inside the packing, the lower the magnetic Janssen effect, until retrieving the classical Janssen mass measurement for $\phi_m = 0$.

The modeled magnetic Janssen effect adapted to the mixture case with a randomized positioning of the ferromagnetic particles is in rather good accordance with the experimental results, although some deviation can be noted for the smallest values of ϕ_m for which the experiments are almost undistinguishable from the classical (non-magnetic) Janssen effect, suggesting the existence of a threshold in ϕ_m^c below which magnetic effects do not play any significant role. The experiments show indeed that the magnetic Janssen effect starts playing a role only for ferromagnetic concentrations higher than $\phi_m^c \approx 0.5$.

To explore this transition, we look at the distribution of clusters of ferromagnetic grains inside the packing. For each magnetic particle, we identify its magnetic neighbours in contact (distance between the two particles lower or equal to $2a$, due to possible overlap of the particles). Similar to a percolation description [11], we identify each cluster with its size s, and compute the associated number of clusters of this size n_s. Using this description, the packing can be

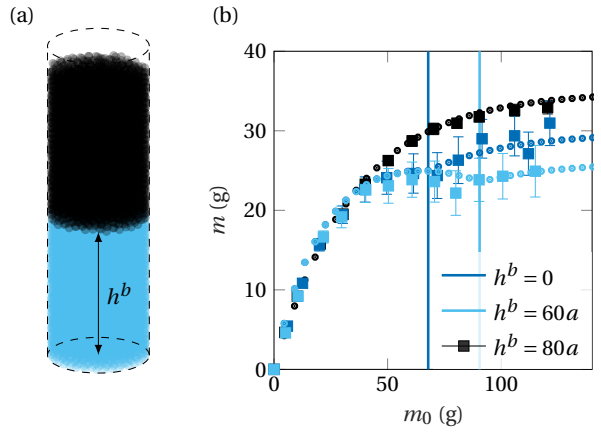

Figure 5. Magnetic Janssen for a buffer ferromagnetic packing. (a) Buffer of ferromagnetic beads at the bottom of the granular column, characterised by its height h^b. (b) Apparent mass of the granular packing varying the buffer height. The experimental data points are in good accordance with the magnetic Janssen prediction where the apparent mass follows a shifted version of the classical Janssen prediction for packing mass higher than the buffer mass. The vertical lines correspond to the buffer mass where the transition from magnetic to classical Janssen occurs.

considered as cohesive if it is made of a unique cluster of connected ferromagnetic grains, meaning that the biggest cluster of size max(s) is equal to the total number of ferromagnetic particles in the packing $\phi_m N$. Figure 4b shows the size max(s) of the biggest ferromagnetic cluster present in the packing, normalized by the total number of ferromagnetic particles, and one can see that there exists a clear transition around $\phi_m = 0.4 - 0.5$ where the packing consists of one connected cluster containing all the ferromagnetic particles, confirming the existence of a concentration threshold. Finally, figure 4c shows the different clusters for two different ferromagnetic concentrations at $\phi_m = 0.3$ and 0.5 where, even though for $\phi_m = 0.3$ the biggest cluster (in blue) has a size of about the tube size, the ferromagnetic grains distribution is still composed of smaller trapped clusters that do not contribute to the magnetic Janssen effect and the ferromagnetic packing cannot be considered as homogeneous.

The random positioning of non-ferromagnetic particles can be seen as the presence of non-ferromagnetic defects inside the packing. Nevertheless, the positioning of both types of particles can be chosen wisely in order to vary the apparent mass behaviour as a combination of both magnetic and classical Janssen effect. To do so, we used the ferromagnetic particles as a "buffer" of the classical Janssen effect, where a set of ferromagnetic particles of height h^b are placed at the bottom of the granular column. Both the representation of the buffer and the experimental results are shown in figure 5. The rationalisation of the results obtained is straightforward. For a packing height lower than the buffer height h^b, the apparent mass follows the magnetic Janssen prediction while for a packing height higher than the buffer height the apparent mass is a combination of both the classical Janssen effect and the magnetic contribution of height $h = h^b$:

$$m = m_J - \frac{\mu}{g} F^r(h^b), \tag{4}$$

The magnetic contribution being a constant depending only on the buffer height, the apparent mass for high packing mass m_0 is finally following a shifted classical Janssen expression m_J. Our experimental results are following nicely the magnetic Janssen prediction, characterised in this case by a point at $m = m^b$ (with $m^b = \pi R^2 \rho \phi_c h^b$ the buffer mass) where the derivative of the apparent mass is not continuous. Moreover, since the apparent mass for high enough packing mass follows a shifted classical Janssen prediction given by the equation (4), the saturation mass of a granular packing with a ferromagnetic buffer is also dependent of the buffer height and magnetic field strength characterised by Ψ. The magnetic global radial force F^r being linear for high enough packing height, we can expect that the new saturation mass of the packing m^*_∞ will depend linearly on the buffer height. Indeed, if we take the limit at high masses of equation (4), we end up with:

$$m_\infty = m^0_\infty - \frac{\mu}{g} F^r(h^b), \tag{5}$$

where m^0_∞ if the saturation mass obtained in the classical Janssen prediction of equation (1).

In this work, we have shown the possibility of controlling the magnetic Janssen effect of a hybrid granular packing composed of both ferromagnetic and non-ferromagnetic grains. The magnetic Janssen effect seems to occur only for an homogeneous packing when all the ferromagnetic grains are connected. Future dynamic simulations of magnetic granular media will help us understanding the origin of this transition. It is also possible to place wisely the ferromagnetic particles, as a buffer for instance, to modify the value of the Janssen's saturation mass. Future work is intended to investigate other spatial distribution of ferromagnetic particles in the packing. A radial distribution, with all ferrromagnetic particles at the center of the tube, would help understanding if ferromagnetic particles contact with the wall is necessary to measure a magnetic Janssen effect. The results presented in this study pave the way toward a more practical use of the magnetic Janssen effect and the design of new tunable hybrid granular media.

ACKNOWLEDGEMENTS

We thank N. Taberlet for enlightening discussions. We thank the Research Council of Norway through its Centre of Excellence funding scheme, project number 262644, the support of ENS de Lyon, and of the CNRS, through the French-Norwegian IRP, (D-FFRACT). S.S. acknowledges

also the support of the Russian Government with grant no. 14.W03.31.0002.

[1] H. A. Janssen, Vereins Eutscher Ingenieure Zeitschrift , 1045 (1895).
[2] L. Thorens, K. J. Måløy, M. Bourgoin, and S. Santucci, Nature Communications **12** (2021), 10.1038/s41467-021-22722-y.
[3] G. Lumay, N. Vandewalle, M. Nakagawa, and S. Luding, in *AIP Conference Proceedings* (AIP, 2009).
[4] G. Lumay, S. Dorbolo, and N. Vandewalle, Physical Review E **80**, 041302 (2009), arXiv:0907.0646.
[5] K. Bai, J. Casara, A. Nair-Kanneganti, A. Wahl, F. Carle, and E. Brown, Journal of Applied Physics **124**, 123901 (2018).
[6] S. Mahajan, M. Tennenbaum, S. N. Pathak, D. Baxter, X. Fan, P. Padilla, C. Anderson, A. Fernandez-Nieves, and M. P. Ciamarra, Physical Review Letters **124** (2020).
[7] G. Ovarlez, C. Fond, and E. Clément, Physical Review E **67** (2003), 10.1103/physreve.67.060302.
[8] N. A. Spaldin, *Magnetic Materials* (Cambridge University Press, 2009) Chap. 2, p. 18.
[9] N. Jain, J. M. Ottino, and R. M. Lueptow, Granular Matter **7**, 69 (2005).
[10] H. Xiao, P. B. Umbanhowar, J. M. Ottino, and R. M. Lueptow, Proceedings of the Royal Society A: Mathematical, Physical and Engineering Sciences **472**, 20150856 (2016).
[11] D. Stauffer, *Introduction to percolation theory* (Taylor & Francis, London Washington, DC, 1992) Chap. 2.

Discharge of a 2D magnetic silo

Louison Thorens[1,2,*], *Maud* Viallet[1], *Knut Jørgen* Måløy[2], *Mickaël* Bourgoin[1], and *Stéphane* Santucci[1,3]

[1]Univ Lyon, ENS de Lyon, Univ Claude Bernard, CNRS, Laboratoire de Physique, F-69342 Lyon, France
[2]PoreLab, The Njord Centre, Department of Physics, University of Oslo, P. O. Box 1048 Blindern, N-0316 Oslo, Norway
[3]Lavrentyev Institute of Hydrodynamics, Siberian Branch of the Russian Academy of Sciences, Novosibirsk, Russia

Abstract. We investigate experimentally the discharge of a 2D-silo, a Hele-Shaw cell, filled with a mono layer of ferromagnetic grains submitted to an external magnetic field **B** perpendicular to the cell plane. In this case the magnetic pair interactions are repulsive. We show that the granular flow rate decreases systematically with the amplitude of the external magnetic field applied. Interestingly, while the output flow rate remains constant during an experiment, we reveal very large spatio-temporal fluctuations of the packing density within the cell, particularly evident for magnetic field of high amplitudes.

1 Introduction

Granular materials have been, over the last decades, celebrated for their particular static and dynamic behaviour [1–3]. One of the most daily encountered granular system is certainly the hourglass where grains flow from a top vessel to a lower one driven only by gravity. The first model to describe the flow of particles flowing through a small aperture was given by Beverloo in 1961 [4]. The particles flow rate is supposed constant and the only size of interest is the opening aperture w which leads to a drainage velocity $v \sim \sqrt{gw}$. Since the opening surface is proportional to the opening width w in a 2D geometry, the output mass flow rate q is then proportional to $\rho\sqrt{g}w^{3/2}$ with ρ the grains density. Beverloo's law gives a better fit to the experimental observation with the following expression: $q = C\rho\sqrt{g}(w - w_m)^{3/2}$ where C is a constant and w_m an opening width correction of about 1 to 2 grain diameters. The grain flow rate is observed to be constant and useful compared to a clepsydra, but the justification of this interesting property is still under debate. The Janssen effect is commonly proposed to justify that the flow rate given by the Beverloo law is independent of the height of the granular column. However, several experimental measurements either in velocity driven [5] or gravity driven conditions [6, 7] have shown that such argument is improper. A clear understanding of the physical origin of the Beverloo law still remains to be unveiled.

Recently, thanks to the use of ferromagnetic particles, we could demonstrate the emergence of a tunable "Magnetic Janssen effect" [8, 9] and, as a result, the possibility to control the apparent mass of a ferromagnetic granular column. Therefore, as a follow-up of those studies, we propose here to go beyond the simple static configuration and investigate now the discharge of a silo filled with ferromagnetic particles. When submitted to an external magnetic field, each particle acquire a magnetic moment **d** leading to tunable magnetic pair interactions inside the grain assembly depending on the magnetic field direction and amplitude. The flow of such magnetic powder has been investigated previously in the case of a 3D funnel [10], with the report of an intermittent flow at the output of the funnel and a strong dependence of the flow rate on the magnetic field amplitude. Nevertheless, the 3D geometry introduces a complex network of ferromagnetic interactions. Here, we propose to focus on a 2D geometry for which the ferromagnetic interactions are reduced to pure repulsion. Previous work using permanent magnets in a 2D silo have been reported [11], however in this case the magnetic interactions cannot be tuned.

2 Flow rate control

A sketch of our experimental setup is given in figure 1a. The setup consists of a Hele-Shaw cell with a gap $e = 0.6\,\text{mm}$ filled with $2a = 500\,\mu\text{m}$ diameter steel beads. The gap consists of two chambers separated by a $w = 10a$ wide opening formed by a 45° funnel. This system is quasi 2D and the beads are arranged in a unique layer packing flowing from the top chamber to the bottom one by gravity. The system is placed in a magnetic coil wider than the cell generating a magnetic field **B** perpendicular to the cell plane. To quantify the strength of the magnetic interactions we consider the magnetic Bond number [10, 12] which compares the magnetic interactions and gravity $\Psi = (\chi_m B)^2/(\mu_0 a\rho g)$ where χ_m is the magnetic susceptibility equals to 3 in our case [13], μ_0 is the magnetic permeability of vacuum. In our experimental set-up, we could reach a maximum value of $\Psi = 62$, corresponding to a magnetic field of 130 G.

Since the magnetic field is homogeneous in the cell plane, each particle i has a magnetic dipolar moment $\mathbf{d} = \chi_m \mathbf{B}/\mu_0$

*e-mail: louison.thorens@ens-lyon.fr

A video is available at https://doi.org/10.48448/ejwj-jr49

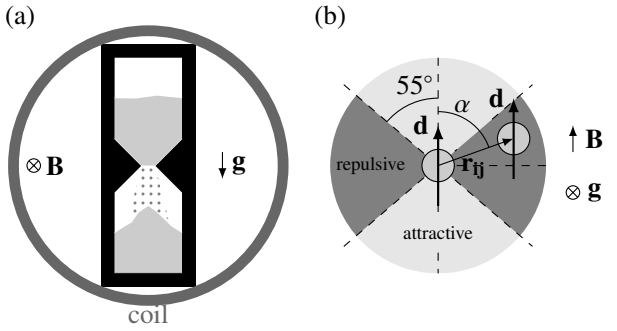

Figure 1. (a) Experimental setup made of a quasi 2D silo in a Hele-Shaw cell with a 45° funnel in its centre. The cell is filled with 500 µm diameter steel beads. The cell is placed in a magnetic coil generating a magnetic field perpendicular to the cell. (b) Top view of the left panel representing the dipolar interaction between two uniformly charged ferromagnetic beads characterized by the dipolar moment **d**.

and interacts with its neighbour j according to the magnetic potential energy:

$$U_{ij} = \frac{\mu_0 d^2}{4\pi r_{ij}^3}(1 - 3cos^2\alpha), \tag{1}$$

where r_{ij} is the beads distance and α is the angle between $\mathbf{r}_{ij}$ and the magnetic field **B**. The magnetic pair interaction is summarized in figure 1b. In general, the interaction can be either repulsive or attractive depending on the angle α, but in our case the quasi 2D geometry leads to a minimum angle $\alpha = \pi/2 - (\arcsin e/2a - 1) \approx 78°$ which means that the interactions are always repulsive.
The experimental protocol is the following: first the beads are at rest in the bottom chamber and we turn the magnetic field on. Then, the cell is rotated using a stepper motor to the next vertical position where the ferromagnetic particles are now in the upper chamber. A high-speed camera (Phantom V10) then records the discharge of the cell at a rate of 440 frames per seconds. Finally, the cell is rotated again and we perform a demagnetisation of the beads using the hysteresis protocol proposed in [18].

We estimated the flow rate using the evolution of the number of beads in the bottom chamber. This number was computed using the apparent area of the bead sedimented cluster occupying the lower chamber after a binarization of the image. Since the contrast between the black grains and the white background is high, the image analysis is rather straightforward and the detection robust. The temporal evolution of the cumulative number N(t) of those sedimented particles during the discharge of the silo is given in figure 2a for different amplitude of the applied magnetic field. We can see that the flow rate given by the slope of those curves $N(t)$ averaged over 5 different experimental realisations, displayed in figure 2b, decreases systematically when we increase the magnetic interaction intensity Ψ. This result was previously reported by [10] in the case of a 3D funnel where the magnetic dipole-dipole interactions within the granular packing could be either attractive or repulsive. In our case where we force the interactions to be purely repulsive, we retrieve this behaviour where the flow rate of the beads flowing through a narrow opening is controlled by the amplitude of the external magnetic field. Nevertheless, we did not find in this case, and for our reachable Ψ, a critical magnetic field threshold above which the bead do not flow anymore.

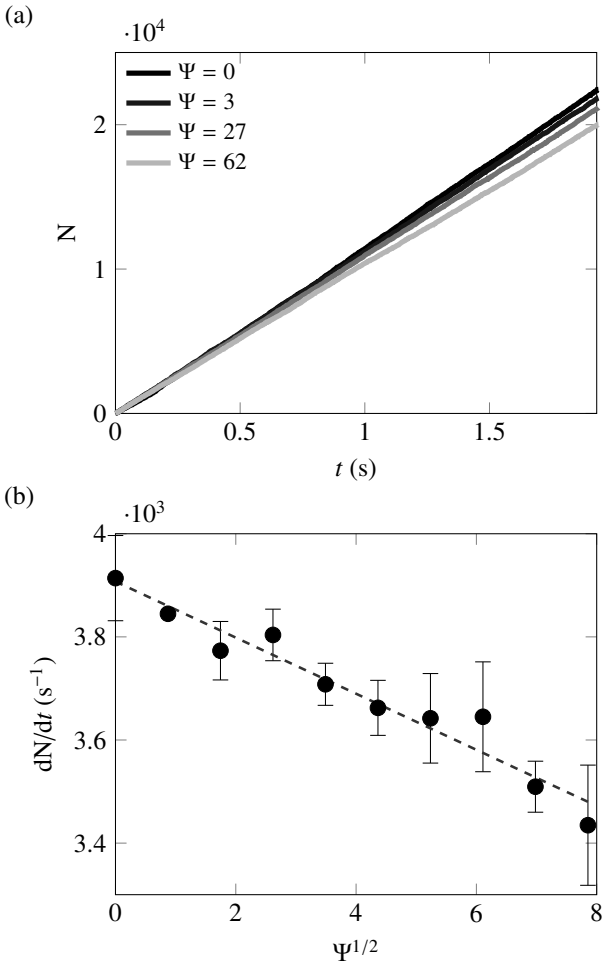

Figure 2. (a) Cumulative number of beads in the lower part of the cell during time for different magnetic field. (b) Flow rate of the beads in the silo given by the slope of the cumulative number of beads. The flow rate decreases when increasing the magnetic field intensity. The dashed line corresponds to a linear fit of the experimental data. Error bars correspond to the standard deviation over three realizations.

The measured flow rate seems to decrease linearly with the amplitude of the magnetic field $B \equiv \Psi^{1/2}$, as shown in figure 2b. This result appears different from the experimental measurement reported in [10], where the flow rate was found proportional to Ψ. This discrepancy could be explained by the different geometry studied (2D versus 3D), involving different magnetic interactions within the granular packing.

3 Internal heterogeneous dynamics

Interestingly, the internal dynamics of the flowing grains within the upper chamber of the silo displays a more

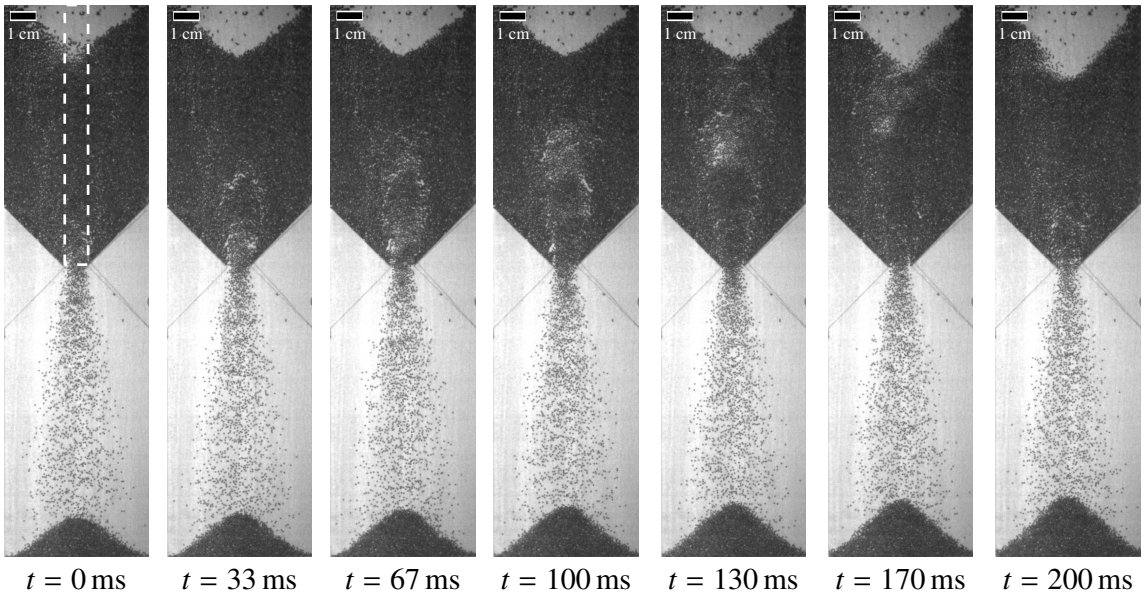

Figure 3. Image sequence of a silo discharge in the case of the maximum magnetic field intensity ($\Psi = 62$). The images were taken at regular time steps and we can see a defect wave, where the beads are free falling inside the structure, going upward. The full sequence of 200 ms corresponds to a propagation cycle where the defect emerges at the funnel neck and go up to the free surface of the structure. The white dashed window shown in the first panel represents the window used for the spatio-temporal maps displayed in figure 4.

complex behaviour. Indeed, we could notice some strong spatio-temporal fluctuations of the density of the packing, which appeared more evidently when increasing the amplitude of the applied magnetic field. In figure 3, we show some typical examples of the flowing patterns on a series of images recorded during one experiment performed with the highest magnetic field $\Psi = 62$ on a 200 ms time range. Examining the top chamber of the cell, we can notice the nucleation of a kind of air bubble, just at the bottom of the funnel, corresponding to a zone where particles are missing. Then, we observe that this bubble is moving upward within the packing, against the granular flow, until it reaches the top free surface in about 170 ms. Furthermore, strikingly, the particles at the free surface of the packing do not move until this bubble could reach the surface; at that point, they fall abruptly, while a new bubble emerges in the opening area. Such heterogeneous granular flow is reminiscent of the early work of [14] reporting experiments of a ticking hourglass. In this case, the lower room is sealed and the flow rate is stopped by the air pressure until Darcy air flow through the grains unclogs the system. A ticking behaviour was also reported by [10] at the output of the funnel using magnetic interactions. Nevertheless, in our case the output flow rate remains constant, as shown in figure 2a, while the heterogeneous dynamics appears only in the top chamber. Our results remind us more of the work presented in [15, 16], respectively for rough and cohesive grains. The observations that were made are close to ours where lower density waves move in the packing creating discrete avalanches of the grains free surface. The proposed explanation is that a part of the grains is clogging the rest of the packing, creating a low density beneath, until the cohesion is not strong enough to support the whole packing. The main advantage of our experiment is the easily tunable aspect of ferromagnetic interactions.

To quantify such complex dynamics, we computed spatio-temporal maps of the flowing particles. In practice, for each experiment, we considered a window of $10a$ width and as high as the top part of the cell centred in the horizontal direction as shown in figure 3 on the first panel. At each time step, we average over the grey scale level of this region, along the horizontal direction (over 37 pixels) to obtain one single vector, giving the mean intensity detected along the vertical position in the chamber (a white zone corresponding to air, while the particles appear in black). The final picture gives a spatio-temporal evolution of the flowing grain packing in the top chamber as used in [17]. The results for three experiments are given in figure 4. Without any magnetic field, $\Psi = 0$, the grains flow out of the top part rather smoothly and the free surface of the packing goes down at a constant flow rate. For an intermediate magnetic field amplitude, $\Psi = 27$, the flow rate remains constant with a linear evolution of the free surface of the packing. However we can distinguish the apparition of irregularities (whitish lines and a slightly rough top-interface) corresponding to the nucleation and motion of the bubbles, previously discussed. Moreover, the duration of the discharge is longer, corresponding to a lower flow rate as we reported in figure 2. Finally, for high magnetic field, $\Psi = 62$, the discharge dynamics within the upper chamber of the cell appears to be very jerky. As we reported on the snapshots of figure 3, and as it clearly emerges in the spatio-temporal figure, the free surface of the packing displays a step-like evolution. Such "stop and go" jerky dynamics is characterized by successive sudden

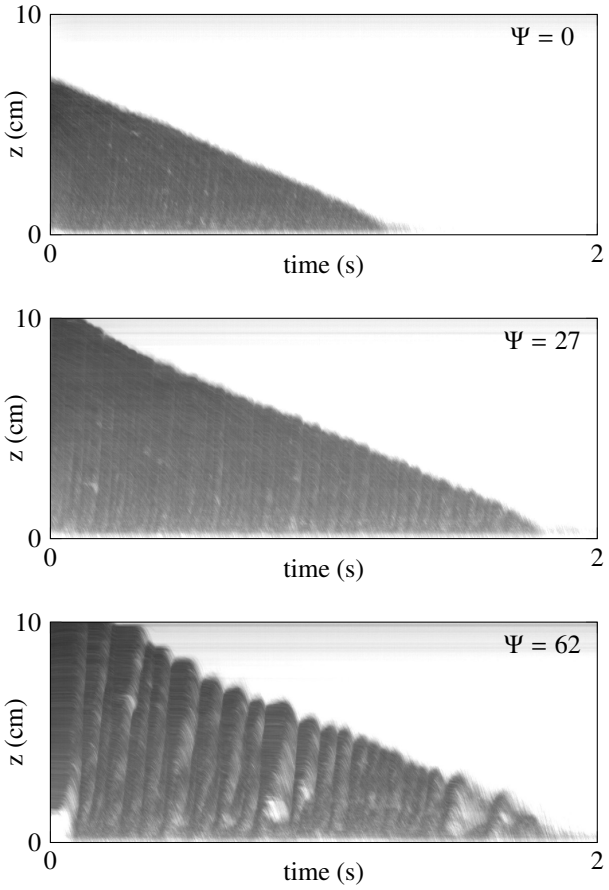

Figure 4. Spatio temporal maps of the flowing particles in the upper part of the silo structure for different magnetic field intensity Ψ. At each time step the vertical data corresponds to an average of the grey scale values over a 10a width rectangle centred on the funnel displayed in the first image of figure 3. For low and medium magnetic field no wave can be seen but we retrieve that the flow rate, given by the free surface slope, decreases. For higher magnetic field, wave propagation given by the step structure in the image appears.

drops of the free surface, followed by waiting times during which the free surface more or less does not evolve. The characteristic pattern formed by the apparition of parallel white lines in the spatio-temporal map, corresponds indeed to the upward motion of a bubble - density defect within the packing.

The waiting time between two successive drops of the free surface corresponds to the time for the bubble-defect, nucleated at the funnel, to propagate through the packing and reach the free surface. Since the white lines in the spatio-temporal maps appear parallel, the velocity of those density-defects is constant and thus the waiting time decreases during an experiment. We can also notice that the white lines are steeper for a lower Ψ. Interestingly, one can also notice that the bubble density-defect velocity depends on the magnetic field amplitude. Moreover, the sudden drops observed at the free surface of about 2 mm of amplitude corresponds to an abrupt avalanche triggered when a bubble reaches the top free surface.

To conclude, we have shown that the discharge dynamics of a ferromagnetic grain assembly depends strongly on the external magnetic field applied. Interestingly, we could somehow realize a tunable hourglass, since the constant flow rate decreases systematically when increasing the amplitude of the applied external magnetic field. Moreover, for high magnetic field amplitudes, the flowing dynamics of the granular packing appears very heterogeneous, with the nucleation of a bubble at the funnel opening and rising through the particles assembly.

References

[1] H.M. Jaeger, S.R. Nagel, Science **255**, 1523 (1992)
[2] H.M. Jaeger, S.R. Nagel, R.P. Behringer, Rev. Mod. Phys **68**, 1259 (1996)
[3] P.G. de Gennes, Rev. Mod. Phys. **71**, S374 (1999)
[4] W. Beverloo, H. Leniger, J. van de Velde, Chem. Eng. Sci. **15**, 260 (1961)
[5] M.A. Aguirre, J.G. Grande, A. Calvo, L.A. Pugnaloni, J.C. Géminard, Phys. Rev. Lett. **104**, 238002 (2010)
[6] C. Perge, M.A. Aguirre, P.A. Gago, L.A. Pugnaloni, D.L. Tourneau, J.C. Géminard, Phys. Rev. E **85**, 021303 (2012)
[7] S. Rubio-Largo, A. Janda, D. Maza, I. Zuriguel, R. Hidalgo, Phys. Rev. Lett. **114**, 238002 (2015)
[8] L. Thorens, K.J. Måløy, M. Bourgoin, S. Santucci, Nat. Commun. in press (2021)
[9] L. Thorens, K.J. Måløy, M. Bourgoin, S. Santucci, EPJ Web Conf. this volume (2021)
[10] G. Lumay, N. Vandewalle, Phys. Rev. E **78**, 061302 (2008)
[11] G. Lumay, J. Schockmel, D. Henández-Enríquez, S. Dorbolo, N. Vandewalle, F. Pacheco-Vázquez, Papers in Physics **7**, 070013 (2015)
[12] J. Vessaire, N. Plihon, R. Volk, M. Bourgoin, Phys. Rev. E **102**, 023101 (2020)
[13] K. Bai, J. Casara, A. Nair-Kanneganti, A. Wahl, F. Carle, E. Brown, J. Appl. Phys. **124**, 123901 (2018)
[14] T.L. Pennec, K.J. Måløy, A. Hansen, M. Ammi, D. Bideau, X. lun Wu, Phys. Rev. E **53**, 2257 (1996)
[15] G.W. Baxter, R.P. Behringer, T. Fagert, G.A. Johnson, Phys. Rev. Lett. **62**, 2825 (1989)
[16] E. Freyssingeas, M.-J. Dalbe, J.-C. Géminard, Phys. Rev. E **83**, 051307 (2011)
[17] E. Mersch, G. Lumay, F. Boschini, N. Vandewalle, Phys. Rev. E **81**, 041309 (2010)
[18] N.A. Spaldin, *Magnetic Materials* (Cambridge University Press, 2009), 18

Capillary washboarding during the slow drainage of a frictional fluid

L. Thorens[1,2], K. J. Måløy[2], E. G. Flekkøy[2], B. Sandnes[3], M. Bourgoin[1], S. Santucci[1,4]
[1] *Univ Lyon, ENS de Lyon, Univ Claude Bernard, CNRS, Laboratoire de Physique, F-69342 Lyon, France*
[2] *PoreLab, The Njord Centre, Department of Physics, University of Oslo, P. O. Box 1048 Blindern, N-0316 Oslo, Norway*
[3] *Energy Safety Research Institute, Swansea University Bay Campus, Swansea, SA1 8EN, UK and*
[4] *Lavrentyev Institute of Hydrodynamics, Siberian Branch of the Russian Academy of Sciences, Novosibirsk, Russia*
(Dated: August 10, 2021)

The slow drainage of a frictional fluid within a confined medium highlights the complex interaction between capillary action and granular stress. For instance, the displacement of grains by a water/air meniscus in a horizontal capillary tube results in the formation of plugs along the geometry. Nevertheless, so far, the triggering of such instability has never been explored. Modifying systematically the wettability and surface tension of the draining liquid within an hydrophobic capillary as well as the height of the sedimented granular bed, we could identify the necessary conditions for the emergence of this bulldozing instability. Furthermore, we also reveal a new unstable regime of the drainage, leading to the periodic formation of dunes, analogous to the road washboarding instability. 2D numerical simulations of a meniscus pushing a bulldozed front of particles explain our experimental observations.

Two-phase flow displacements of settling granular mixtures with inter-particle friction in confined geometries, also known as frictional fluids, are common in Nature and engineering systems. Indeed, numerous industrial processes, such as oil recovery and soil decontamination imply the transport of liquids, sand, and gas [1]. The transport of sediments remodelling bed rivers or the circulation of physiological fluids with the transport of blood cells in the vascular systems [2, 3] constitute also examples of prime importance occurring in natural and biological situations.

In order to apprehend the complexity of such flows, due to specifically the interaction between capillary processes and granular stresses governed by the frictional contacts with the confining walls, experiments in Hele-Shaw cells and capillary tubes, have been designed using glass beads and water [4–7]. Such model experiments allowing for a direct visualisation of the multiphasic displacement dynamics could reveal a wide range of complex flows, with instabilities, from stick-slip bubbles to destabilized viscous fingers, depending on the amount of particles present in the confining medium and the liquid flow rate [6, 8].

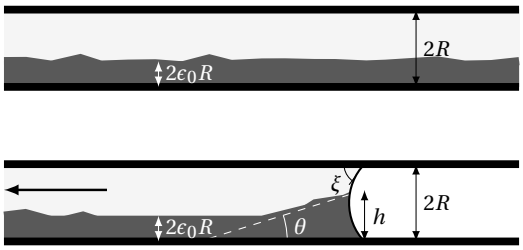

Figure 1. Bulldozing instability. A granular bed of height $2\epsilon_0 R$ rests at the bottom of a capillary tube of height $2R$. While draining out the liquid out the tube, a meniscus at the liquid/air border appears. The meniscus may bulldoze partly the particles on its way forming a bulldozing front of height h.

In this study we focus on the bulldozing instability described in [9, 10] and presented in figure 1. The system is composed of a granular bed of height $2\epsilon_0 R$ resting in an hydrophobic capillary tube of radius $R = 1\,\text{mm}$. The liquid is withdrawn from the left side of the tube at a constant flow rate $I_0 = 0.1\,\text{ml}$. The flow rate is slow enough to ensure no viscosity effect during the drainage, according to the criterion given in [6]. The other side of the tube is opened to air. While draining the liquid, a meniscus at the liquid/air boundary appears, bulldozing the particles on its way. The particles may be bulldozed up to the top of the geometry. Reaching this limit, due to the Janssen effect, the friction force exerted by the particles packing on the wall grows exponentially with the amount of bulldozed particles. When the pressure required to push the bulldozing front exceeds the capillary pressure threshold that allows air to enter the granular medium, air enters the granular medium and a plug of grains is left behind. This process repeats itself along the tube resulting in a plug trail along the geometry as shown in figure (2.a). The plug formation process has been previously described in details by [9]. However, the triggering of this instability has never been studied.

In this study, we focus on the onset of the bulldozing mechanism. We investigate the influence of the system parameters (liquid properties, height of settling bed) on the bulldozing dynamics. We also highlight the existence of a "capillary washboarding" instability when particles are only partially bulldozed by the meniscus.

The granular medium is composed of polydisperse glass beads of diameter $d = 100\,\mu\text{m} - 200\,\mu\text{m}$. In previous studies, the surrounding liquid was water of surface tension $\gamma = 72\,\text{mN}\cdot\text{m}^{-1}$. In this study, to modify the liquid properties, we use a solution of water and isopropanol (or 2-propanol). Isopropanol has a lower surface tension than water $\gamma_{\text{2-propanol}} = 22\,\text{mN}\cdot\text{m}^{-1}$. The surface tension γ and the wetting angle ξ of the solution depend on the weight amount of alcohol (2-propanol $\%_w$). The surface tension measurement using a drop-shape analyser (Kruss DSA24E) are given in figure (3.a), found in excellent accordance with [11]. The tube was made hydrophobic using a silanization

solution (~5% dimethyldichlorosilane in heptane). Increasing the amount of alcohol in the solution changes drastically the wetting contact angle. Experimental measurements of the contact wetting angle on a silanized glass plate are given in figure (3.b).
To compare the bulldozing power of each liquid, we consider a friction pad ahead of the meniscus of height $h = 2R$. The force needed to push it is given by:

$$f_{\text{friction}} = 2\mu g \frac{\pi R^3}{\tan\theta}\Delta\rho\,, \tag{1}$$

where θ is the avalanche angle defined in figure (1). The force exerted by the meniscus can be approximated by:

$$f_{\text{meniscus}} = 4\gamma R \sin\xi\,. \tag{2}$$

If the force exerted by the meniscus is greater than the friction force, the particles are pushed. To characterise the meniscus ability to displace the granular packing we then define the dimensionless number:

$$\mathscr{C} = \frac{2\gamma\tan\theta\sin\xi}{\mu g\Delta\rho\pi R^2}, \tag{3}$$

For pure water, we find $\mathscr{C} = 2.7$, that can explain why, when using water in previous studies, the bulldozing mechanism was always occurring. For pure alcohol, we find $\mathscr{C} = 0.028$. With our water/isopropanol solution, the dimensionless number $\mathscr{C}$ ranges on two decades, and we can expect different drainage dynamics.

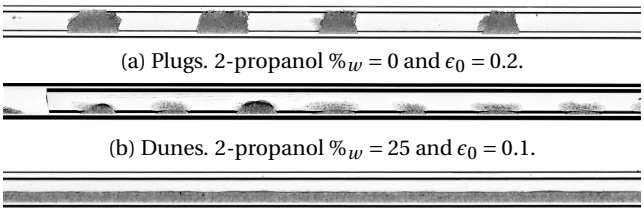

(a) Plugs. 2-propanol $\%_w = 0$ and $\epsilon_0 = 0.2$.

(b) Dunes. 2-propanol $\%_w = 25$ and $\epsilon_0 = 0.1$.

(c) Stable layer. 2-propanol $\%_w = 100$ and $\epsilon_0 = 0.5$.

Figure 2. Different types of pattern formed along the tube depending on the liquid properties and initial height of particles. If the particles are clogging the tube, plugs are formed governed by the Janssen effect. When the meniscus is bulldozing partly the particles, a series of periodic dunes is formed on the way. For pure alcohol, the meniscus is not bulldozing any particles and the particles bed remains unperturbed.

Depending on the liquid properties and the initial height of particles, different patterns appear in the tube. Figure (2 gives the three different possible systems. For a low concentration of isopropanol, or high initial height of particles in the tube $2\epsilon_0 R$, the system reaches the clogging situation and plugs are formed along the tube. This situation corresponds to the plug pattern formation described in [9]. For a high concentration of isopropanol in the solution, the meniscus slides over the sedimented bead layer and no particles is bulldozed. We refer to this situation as "resting particles". Finally, for a medium concentration of isopropanol and a low initial height of particles, we reach the "capillary washboarding" situation. In this case, the meniscus bulldozes partially the particles in the tube. Before reaching the clogging situation, the meniscus passes over the bulldozed particles forming a dune. The final pattern is made up of a recurring series of dunes.

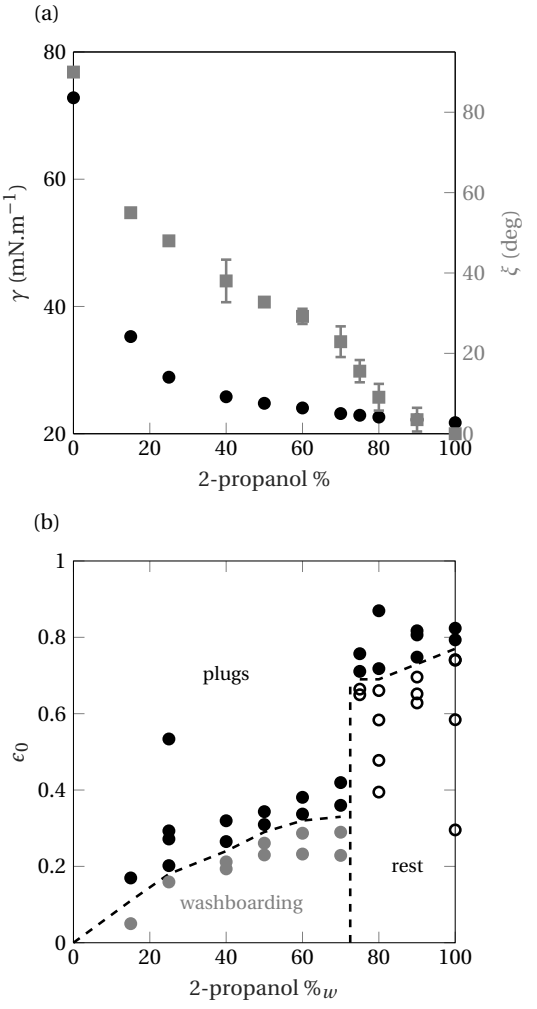

Figure 3. (a) Experimental measurement of the isopropanol/water solution properties: surface tension (in black) and wetting contact angle (in grey). (b) Phase diagram of the drainage experiment. Depending on the alcohol concentration of the solution, or initial height of particles different dynamics are observed. As presented in figure (2), the three different dynamics are plugs (black), dunes (grey) or resting particles (white). The dashed lines correspond is the interpolated boundary between the three phases.

In figure (3.b), we summarise the experimental reached state depending on the two system parameters: isopropanol concentration and initial height of particles $2\epsilon_0 R$. For 2-propanol$\%_w$ $w70$, the capillary washboarding mechanism governs the dynamics of the system. By increasing ϵ_0, we may reach the clogging situation and trigger the plug for-

mation mechanism. However, for high isopropanol concentration the capillary washboarding mechanism is never obtained and a direct transition to the plug formation appears at larger ϵ_0.

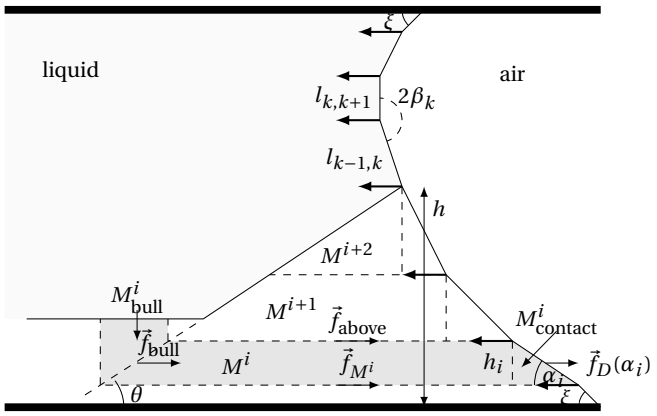

Figure 4. Global sketch of the simulated system. First, the meniscus is modelled by a series of points k characterised by the pair distances $l_{k,k+1}$ and local angle of curvature $2\beta_k$. Second, the bulldozed front, of height h and avalanche angle θ, is cut in different layers. Each layer of mass M^i is in contact with a bulldozing part M^i_{bull} and a titled part M^i_{contact}.

We used numerical simulation of the meniscus bulldozing the particles inside a 2D confined geometry to explain our experimental results. the global sketch of the simulated system is given in figure (4. The system is composed of two distinct parts that we describe independently. First, we focus on the simulation of the meniscus without the presence of particles in the geometry. Second, the introduction of particles in the system adds granular stress on the meniscus with a feedback effect resulting in its deformation.
The simulation of the meniscus is inspired by the work of [5]. In this work, the meniscus simulations were designed to model the formation of labyrinthine patterns during the slow drainage of a frictional fluid inside a Hele-Shaw cell. In our case, we use this 2D simulations in the out-of-plane (vertical) direction. The meniscus is modelled by a series of points k separated by a series of length $l_{k,k+1}$. at each point, the local angle between two successive meniscus segments $2\beta_k$ is computed. From these two local parameters, one can compute the local curvature of the meniscus κ_k given by:

$$\kappa_k = \frac{\pi - 2\beta_k}{l_{k-1,k} + l_{k,k+1}} \,. \tag{4}$$

Using the value of the local curvature, one can compute the capillary pressure acting on the meniscus given by Laplace equation:

$$\delta P_k = \gamma \kappa_k \,, \tag{5}$$

where γ is the effective liquid surface tension in contact with air. The wetting contact angle ξ is fixed during the whole simulation by forcing the meniscus local angles at the top and bottom of the tube:

$$\beta_1 = \beta_N = \frac{\pi - \xi}{2} \tag{6}$$

where N is the number of points modelling the meniscus.
We need to compute the granular stress acting on each meniscus point. At each time step, the amount of bulldozed particles ahead of the meniscus is characterised by its height h. The bulldozed grains are forming a constant avalanche angle θ with the horizontal. For each meniscus segment in contact with grains, we can differentiate four different granular forces contributions:

- the bulldozed layer of mass M^i_{bull}, applying a force $f_{\text{bull}} = \mu \cos^2\theta g M^i_{\text{bull}}$,
- the layer itself of mass M^i, applying a force $f_{M^i} = \mu g M^i$,
- the layers above of mass $\sum_{k>i} M^k$, applying a force $f_{\text{above}} = \mu g \sum_{k>i} M^k$,
- the tilted layer in contact with the meniscus of mass M^i_{contact}, applying a force $f_{\text{contact}} = \mu_D(\alpha_i) g M^i_{\text{contact}}$.

The latter part of the layer is pushed horizontally by a titled segment of the meniscus. This situation is similar to the washboard road instability [12–14] where a periodic riddles pattern appears at the top of a sand road by the repeated passage of vehicles.

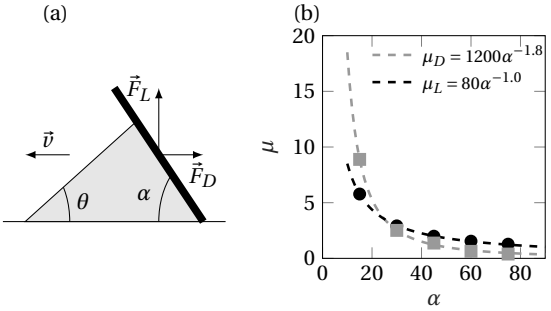

Figure 5. (a) Geometry of the pad pushed by a plane advancing at a constant velocity v with an angle of attack α. (b) Data from [14]. Friction coefficients of the drag F_D and lift F_L forces.

As suggested by [14, 15], the local friction coefficient μ_D depends on the local angle of attack α_i. At the moment, the direct dependence of the friction coefficient on the angle of attack is not fully understood. We propose to fit the experimental data from [14] by a power law $\mu_D = a_D \alpha^{b_D}$ detailed in figure (5). Using all frictions forces acting on each granular layer i, we define the local granular stress acting on the meniscus segment by:

$$\sigma_i \delta S_i = f_{\text{bull}} + f_{M^i} + f_{\text{above}} + f_{\text{contact}} \,, \tag{7}$$

where δS_i is the local surface of the meniscus plane. At each time step, the local capillary action and the local granular stress are computed at each meniscus point. The pressure difference across the fluid air interface $\delta P_i(z)$ at position z decrease with the height according to :

$$\delta P_i(z) = \delta P_i(z = 2R) - \rho_l g(2R - z)\,. \tag{8}$$

At each time step, a meniscus point may advance if $\delta P_i(z)$ overcomes the sum of the capillary pressure $\gamma\kappa_i$ and granular stress term σ^i:

$$\delta P_i(z) > \gamma\kappa_i + \sigma^i\,, \tag{9}$$

or

$$\delta P_i(z = 2R) > \rho_l g(2R - z) + \gamma\kappa_i + \sigma^i\,. \tag{10}$$

Ultimately, the meniscus point advancing at each time step is the one minimising $\rho_l g(2R - z) + \gamma\kappa_i + \sigma^i$. This point advances horizontally over a distance δx_i which is set to keep the withdrawing rate constant in order to the match the experimental protocol. Finally, to ensure mass conservation, at each time step the bulldozed height h is updated accordingly while keeping the avalanche angle θ constant.

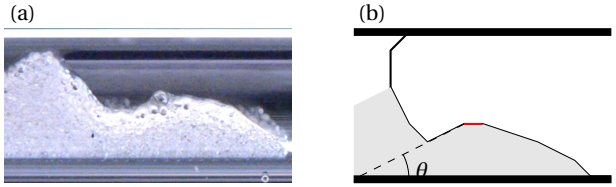

Figure 6. Descent phase of the meniscus during experiment (a) and simulation (b). When the local angle of attack is lower than a threshold $\alpha_{\min} = 4°$ (in red), the meniscus plunges in the sedimented layer of beads.

During the simulation, the meniscus will deform itself in response to the increase of the granular stress with the bulldozed height h. As the meniscus bends horizontally during deformation, the local angles of attack diminish, increasing even more the local granular stress. The deformation of the meniscus may result at some point in a horizontal meniscus plane. From experimental observation shown in figure (6), we remark that at this point the meniscus plunges in the sedimented bed forming an angle θ with the horizontal. This angle is observed to be similar to the avalanche angle. The origin of this behaviour still needs to be addressed. In the simulation, we force this descent phenomenon when the local angle of attack is lower than the threshold $\alpha_{\min} = 4°$.

In our simulations, we can tune both liquid properties ξ, γ and the initial height of particles $2\epsilon_0 R$. First, we set the liquid properties of the liquid in accordance with the isopropanol/water solution while varying the initial height of particles. The results of our simulation are given as a

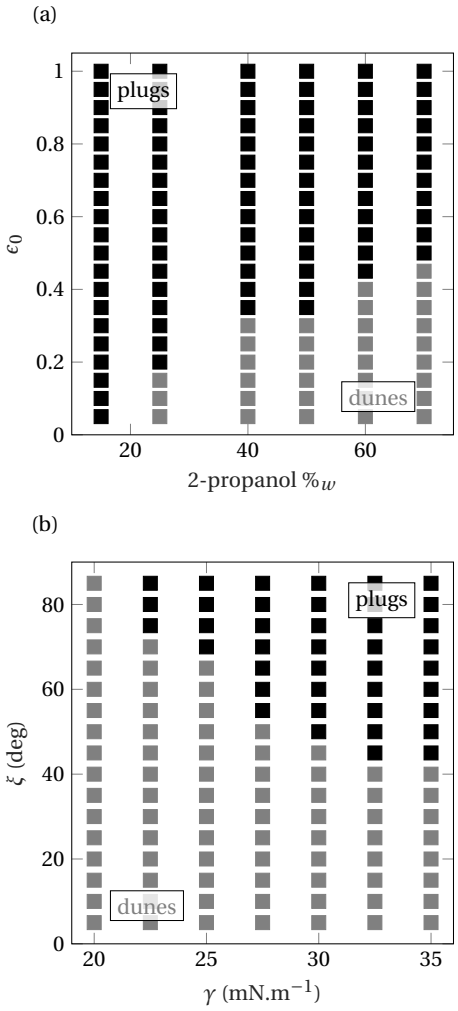

Figure 7. (a) Simulation phase diagram of the different bulldozing mechanisms depending on the solution concentration in alcohol and initial height of particles. The simulations results (squares) are compared to the experimental results (circles), following the same tendency on the different parameters. (b) Simulation phase diagram varying the liquid properties γ, ξ while keeping the initial amount pf particles constant $\epsilon_0 = 0.3$.

phase diagram presented in figure (7.a). When compared with the experimental results, our results are found in good accordance. We retrieve the same dependence with ϵ_0: increasing the initial height of particles in the system leads to a transition from dunes to plugs formation. During the simulation, the meniscus deforms itself responding to the increase of the granular stress until becoming almost horizontal at some point. Then, a dune is left behind while the meniscus plunges in the sedimented bed and the process repeats itself. Thanks to mass conservation, an increase of the initial height of particles leads to a quicker increase of the bulldozed height h. The clogging situation $h = 2R$ is reached before a complete deformation of the meniscus.
Unlike the experiments, we can vary both liquid parameters

ξ, γ independently. The simulation results while keeping the initial height of particles fixed by $\epsilon_0 = 0.3$ are given in figure (7.b). When decreasing the surface tension γ or the wetting angle ξ, the system transit from plugs formation to the capillary washboarding dynamics. We note that both liquid parameters have an impact on the meniscus dynamics.

During the slow drainage of liquid in the presence of sedimented grains out of a confined geometry, bulldozing mechanism may occur. The meniscus at the liquid/air boundary can bulldoze the particles ahead forming a so-called bulldozing front. On its way, due to granular stress acting on the meniscus, the latter deforms itself. If the bulldozing front reaches the top of the tube, a plug formation process starts as described in [9]. However, when increasing the amount of bulldozed particles, the meniscus can be deformed to an horizontal position. At this point, a dune is formed, this is the capillary washboarding mechanism. The process repeats itself to form a series of dunes along the tube. Future experimental work is intended to characterise the formation of dunes (period, amplitude). The transition for high concentration of alcohol from a resting beads layer to plugs formations still needs to be addressed. Finally, as described in [9], the plugs formation if governed by the Janssen effect. Recent work [16] proposed to control this Janssen effect by applying an external magnetic field on ferromagnetic grains. Using this idea, future work is intended to force the bulldozing instability as well as changing the resulting pattern.

ACKNOWLEDGEMENTS

We thank N. Taberlet for the constructive discussion concerning the washboard instability. We thank the Research Council of Norway through its Centre of Excellence funding scheme, project number 262644, the support of ENS de Lyon, and of the CNRS, through the French-Norwegian IRP, (D-FFRACT). S.S. acknowledges also the support of the Russian Government with grant no. 14.W03.31.0002.

[1] J. Tronvoll and E. Fjær, International Journal of Rock Mechanics and Mining Sciences & Geomechanics Abstracts **31**, 393 (1994).
[2] D. Gidaspow and J. Huang, Annals of Biomedical Engineering **37**, 1534 (2009).
[3] J. B. FREUND and M. M. ORESCANIN, Journal of Fluid Mechanics **671**, 466 (2011).
[4] B. Sandnes, H. A. Knudsen, K. J. Måløy, and E. G. Flekkøy, Physical Review Letters **99**, 038001 (2007).
[5] H. A. Knudsen, B. Sandnes, E. G. Flekkøy, and K. J. Måløy, Physical Review E - Statistical, Nonlinear, and Soft Matter Physics **77** (2008), 10.1103/PhysRevE.77.021301.
[6] B. Sandnes, E. G. Flekkøy, H. A. Knudsen, K. J. Måløy, and H. See, Nature Communications **2** (2011), 10.1038/ncomms1289.
[7] G. Dumazer, B. Sandnes, K. J. Måløy, and E. G. Flekkøy, Physical Review Fluids **5** (2020), 10.1103/PhysRevFluids.5.034309.
[8] B. Marks, B. Sandnes, G. Dumazer, J. A. Eriksen, and K. J. Måløy, Frontiers in Physics **3**, 1 (2015), arXiv:arXiv:1505.04054v1.
[9] G. Dumazer, B. Sandnes, M. Ayaz, K. J. Måløy, and E. G. Flekkøy, Physical Review Letters **117**, 028002 (2016).
[10] G. Dumazer, B. Sandnes, M. Ayaz, K. J. Måløy, and E. Flekkøy, EPJ Web of Conferences **140**, 09016 (2017).
[11] G. Vazquez, E. Alvarez, and J. M. Navaza, Journal of Chemical & Engineering Data **40**, 611 (1995).
[12] D. C. Mays and B. A. Faybishenko, Complexity **5**, 51 (2000).
[13] N. Taberlet, S. W. Morris, and J. N. McElwaine, Physical Review Letters **99** (2007), 10.1103/physrevlett.99.068003.
[14] B. Percier, S. Manneville, J. N. McElwaine, S. W. Morris, and N. Taberlet, Physical Review E - Statistical, Nonlinear, and Soft Matter Physics **84**, 051302 (2011), arXiv:1107.5494.
[15] B. Percier, S. Manneville, and N. Taberlet, PHYSICAL REVIEW E **87**, 12203 (2013).
[16] L. Thorens, K. J. Måløy, M. Bourgoin, and S. Santucci, Nature Communications **12** (2021), 10.1038/s41467-021-22722-y.